SEVERE PLASTIC DEFORMATION

OF DIFFICULT-TO-WORK ALLOYS

A Thesis

by

GUNEY GUVEN YAPICI

Submitted to the Office of Graduate Studies of
Texas A&M University
in partial fulfillment of the requirements for the degree of

MASTER OF SCIENCE

May 2004

Major Subject: Mechanical Engineering

SEVERE PLASTIC DEFORMATION

OF DIFFICULT-TO-WORK ALLOYS

A Thesis

by

GUNEY GUVEN YAPICI

Submitted to Texas A&M University
in partial fulfillment of the requirements
for the degree of

MASTER OF SCIENCE

Approved as to style and content by:

_____   _____
Ibrahim Karaman   Karl Theodore Hartwig
(Chair of Committee)   (Member)

_____   _____
Amy Epps Martin   Dennis L. O'Neal
(Member)   (Head of Department)

May 2004

Major subject: Mechanical Engineering

ABSTRACT

Severe Plastic Deformation of Difficult-To-Work Alloys. (May 2004)

Guney Guven Yapici, B.S., Bogazici University, Turkey

Chair of Advisory Committee: Dr. Ibrahim Karaman

The present work aims to reveal the microstructural evolution and post-processing mechanical behavior of difficult-to-work alloys upon severe plastic deformation. Severe plastic deformation is applied using equal channel angular extrusion (ECAE) where billets are pressed through a 90° corner die achieving simple shear deformation. Three different materials are studied in this research, namely Ti-6Al-4V, Ti-6Al-4V reinforced with 10% TiC and AISI 316L stainless steel. Microstructure and mechanical properties of successfully extruded billets were reported using light microscopy, scanning electron microscopy (SEM), transmission electron microscopy (TEM), tension and compression experiments and microhardness measurements. The effects of extrusion conditions (temperature and processing route) on the microstructure and mechanical properties are investigated. The underlying mechanisms responsible for observed mechanical behaviors are explored.

It is seen that ECAE shear deformation leads to refinement in α plates and elimination of prior β boundaries in Ti-6Al-4V. Decreasing extrusion temperature and increasing number of passes decreases α plate size and grain size. Refined α grain size leads to a significant increase in tensile and compressive flow stresses at room

temperature. Texture produced by ECAE has a pronounced effect on mechanical properties. Specifically it leads to tension/compression asymmetry in flow strengths and strain hardening coefficients may be described by the activation of differing slip systems under tension and compression loading. ECAE of Ti-6Al-4V+10%TiC samples also improved mechanical properties due to α plate size refinement. Nevertheless, further extrusion passes should be carried out for tailoring reinforcement size and distribution providing optimum strength and ductility.

ECAE deformation of AISI 316L stainless steel at high homologous temperatures (0.55 to 0.60 T_m) results in deformation twinning as an effective deformation mechanism which is attributed to the effect of the high stress levels on the partial dislocation separation. Deformation twinning gives rise to high stress levels during post-processing room temperature tension and compression experiments by providing additional barriers to dislocation motion and decreasing the mean free path of dislocations. The highest tensile flow stress observed in the sample processed at 700 $^{\circ}$C following one pass route A was on the order of 1200 MPa which is very high for 316L stainless steel.

The ultimate goal of this study is to produce stabilized end microstructures with improved mechanical properties and demonstrate the applicability of ECAE on difficult-to-work alloys.

Dedicated To My Parents, Cahit and Selma Yapici

For their endless love.

ACKNOWLEDGEMENTS

Last, but most importantly is the continuous courage and support received from my family. Murat, who did not leave me alone even in Texas, has been my strongest supporter and lovely brother. In addition, the visits of my mother and my aunt have been great times with their endless support throughout my studies. At this point, I would like to thank my father for encouraging me to study in the US and letting me discover the possibilities in this country.

TABLE OF CONTENTS

LIST OF FIGURES

LIST OF TABLES

CHAPTER I

INTRODUCTION

1.1 Background

Bulk nanostructured materials have been attracting attention due to their improved physical and mechanical properties [1-3]. Several techniques have been proposed for the fabrication of these materials including gas condensation, ball milling with subsequent consolidation and various severe plastic deformation (SPD) techniques [2-4]. SPD techniques are of advantage due to major difficulties inherent to other nanostructured material processing techniques. To name a few, there is residual porosity in compacted samples, impurities from ball milling and inability to process large scale billets. SPD methods are important due to the requirement of very high plastic strains at relatively low temperatures to attain nanostructures. Although conventional forming techniques carried out at low temperatures such as rolling or drawing may result in the formation of nanostructures; the substructures formed are usually of cellular type having boundaries with low angles of misorientation. In contrast, SPD techniques may form grains with sizes on the order of 100-200 nm and with high angle grain boundaries [2]. From the various SPD techniques; the idea of utilizing simple shear is developed by Segal in former Soviet Union [5]. The process is called equal channel angular extrusion (ECAE) and consists of deforming a billet of material through two intersecting channels of equal cross-sectional area at an angle of 2φ to each other, without a decrease in billet

This thesis follows the style and format of *Materials Science and Engineering A*.

cross-sectional area. Heavily deformed microstructures are formed in the processed billets [6].

Up to now, easy to work materials such as copper and aluminum were the primary materials used in the development of ECAE [7-10]. Mechanical properties of difficult-to-work alloys have been a major research topic for many researchers. However, these studies were generally limited to conventional processes or lack the detailed study needed for exploring the effect of processing parameters on the mechanical behavior of severely deformed materials [11-14]. This is because severe plastic deformation especially ECAE of difficult-to-work alloys forms a challenge due to the very high flow stress and limited ductility of these materials.

Successful ECAE processing of some hard materials have been reported at high temperatures [15-17]. In general, the success of an ECAE process depends on several factors, including the extrusion conditions, material constitutive behavior, friction conditions and tooling design [18]. These factors may be classified as macro-level and micro-level conditions. Macro-uniformity must be attained by special static boundary conditions which depend on the friction between the sample and press equipment, tooling design, the contact area and the special back pressure. Without the presence of the special boundary conditions, non-uniform plastic flows leading to fracture may occur. Similarly, low temperature extrusions of hard materials may form instabilities in the microstructure such as shear bands [15]. Micro-level conditions should provide the suitable strain, strain rate level and temperature to reach the desired level of grain

refinement. The difficult-to-work alloys that were studied in this research are; Ti-6Al-4V, Ti-6Al-4V reinforced with 10% TiC and AISI 316L stainless steel.

Titanium alloys are used extensively in aerospace and biomedical applications due to their low density, high corrosion resistance, high strength, toughness, good elevated temperature properties and formability. Among these alloys Ti-6Al-4V (Ti64) remains the primary choice for damage-tolerant components [19]. Several investigators have shown that an optimal combination of fracture toughness and high cycle fatigue (HCF) can be achieved in Ti64 through the introduction of a bimodal microstructure [20, 21]. The latter is characterized by the presence of approximately 15 vol.% equiaxed primary alpha with the remainder present as transformed beta lamellae. Further effort has shown that the HCF performance of the bi-modal microstructure can be enhanced by decreasing the slip line length, the latter depending upon the equiaxed alpha size and alpha plate spacing [20-22]. Additionally the fracture toughness can be enhanced by controlling the lamellae spacing.

The other material, Ti-6Al-4V+10%TiC (Ti64/TiC) metal matrix composite constitutes randomly dispersed TiC particles in Ti64 matrix. This alloy is also utilized extensively in the aerospace industry. ECAE has shown to be effective in breaking down and aligning the SiC second phase particles within the aluminum alloy matrix [23]. Studies on Cu-Nb and Cu-Ag two phase alloys showed that ECAE leads to the transformation of structural elements into aligned, thin filaments [24].

AISI 316L is a low stacking fault austenitic stainless steel. Austenitic stainless steels are useful in a broad range of industrial applications mainly due to their excellent

corrosion resistance [25]. High work hardening is another typical feature of stainless steel. It is obtained not only through glide and interaction of dislocations but also with the presence of stacking faults, deformation twins and their interaction with slip [26, 27]. The typical deformation mechanisms taking place in austenitic steels start with dislocation slip at the early stages, continues on with the formation of extensive stacking faults where planar slip is dominant. At higher strains, cross-slip takes over resulting in band structures containing cells until the stage where twinning becomes the dominant mechanism of deformation before strain instability [28]. It is also reported that mechanical twinning can be assisted by the addition of solute atoms that can raise the shear stress for slip while reducing the stacking fault energy (SFE) [26, 29]. Reduction in SFE leads to wider partial dislocation separation, resulting in a structure with planar dislocation arrays, thus enhancing the propensity of twinning. Decrease in deformation temperature may also lead to the formation of planar dislocations, which reduce the ability of a material to cross-slip causing the early onset of twinning.

Another mechanism that needs to be considered at high temperatures in austenitic stainless steels is dynamic strain aging (DSA). DSA has been reported to cause serrated flow under certain combinations of temperature and strain rate [29-36]. In addition, flow stress and strain hardening typically peak at a certain temperature in the DSA region, which itself is a function of strain rate [35]. For 316L austenitic stainless steel, this temperature range is reported to be 500 – 600 °C for a strain rate of $10^{-3} - 10^{-4}$ s^{-1} [35-37]. DSA occurs due to easy diffusion of carbon and nitrogen or Cr atoms depending on the DSA regime and their pinning effect for dislocations. Serrated flow is due to

repeated yielding by unlocking of dislocations from solute atmospheres and the formation of new solute atmosphere. DSA may be effective in the activation of twinning in the sense that it increases the stress level by restriction of dislocation motion. It is of great interest to observe the activation of different mechanisms induced by high strain and strain rate applied during severe plastic deformation.

In the following sections, the principles of ECAE including the parameters that affect the resulting mechanical behavior, possible deformation mechanisms in the research materials and previous studies in relation to the current work are discussed.

1.2 Principles of Equal Channel Angular Extrusion

ECAE is carried out by introducing a lubricated billet into a die containing two channels with equal cross-section. For sufficiently long billets, plastic flow is essentially steady and in one plane. The channels intersect at an angle denoted by 2ϕ near the center of the die. The process is described in Fig. 1.2.1. Under these conditions the billet moves inside the channels as a rigid body, and deformation is achieved by simple shear in a thin layer at the crossing plane of the channels [2, 5]. In this way the complete billet, except the small end regions and the minor surface area is deformed in the same uniform manner. The die angle determines the incremental strain intensity applied as the billet passes through the shear plane [5, 38]. The effective Von Misses strain per pass is given by [38, 39] :

$$\varepsilon = \frac{2}{\sqrt{3}} \cot \phi$$

The punch pressure needed to press the billet can be determined by:

$$p = \frac{2}{\sqrt{3}} \cdot \sigma_y \cdot \cot \phi$$

where σ_y is the yield stress of the material.

The equivalent reduction ratio (RR) and the equivalent area reduction (AR) values of ECAE for N passes with respect to conventional extrusion can be found as:

$$RR = \exp(N \cdot \varepsilon) \quad \text{and} \quad AR = (1 - RR^{-1}) \cdot 100\%$$

In the current study the intersection angle is 90° and the billet is pressed through the die using a servohydraulic press. With a die angle of 90°, a true plastic strain of 1.15 and equivalent area reduction of 69% can be reached [38].
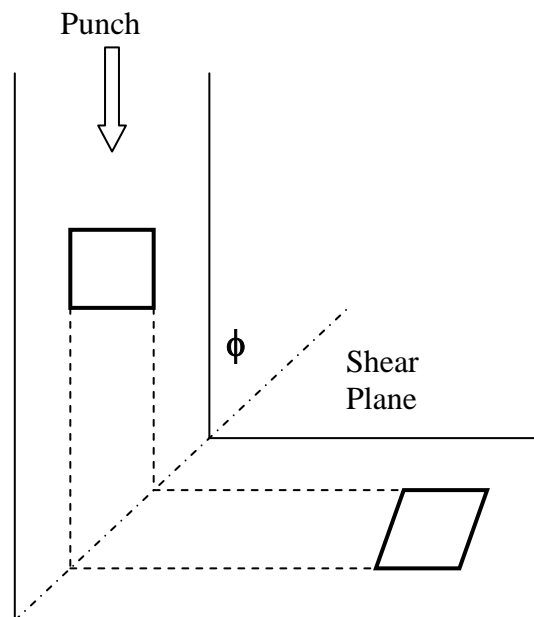
Fig. 1.2.1. Schematic demonstrating the ECAE process. The representative material element goes through simple shear deformation.

The most important advantage of ECAE is the development of near uniform, intensive and simple shear in bulk billets. It is reported that simple shear is a near ideal

deformation method for creation of special structures, strong texture and unique properties [5, 6, 8]. However, conventional processes are not sufficient to transform simple shear into an ordinary and effective operation for high quality large products [2, 40]. Also, it is apparent that with ECAE, a large and uniform strain intensity per pass can be reached in material under low pressure and load without a reduction of the initial billet cross-section. It is reported that ideal extrusion giving the same final products require N time higher pressure compared to ECAE [38]. The advantages of equal channel angular extrusion are more evident with multiple extrusions of the billet. The process can easily be repeated a number of times in the same tool and very large effective deformations can be produced without a decrease in billet cross-sectional area. For an ECAE process of N passes, the total strain imposed is [39]:

$$\varepsilon_t = N \cdot \varepsilon$$

Here ε is the effective Von Misses strain per pass as given earlier. Multiple passes can be applied by changing the billet orientation at each step. This results in the modification of the shear planes and shear directions and is important for the creation of special structures and textures.

From the many possibilities, the common routes are described below and shown schematically in Fig. 1.2.2.

Route A: For this sequence of extrusions, the billet orientation is the same at each pass. As a result, the distortion of material elements is continuously increased with each successive pass. Because all elements are distorted in the same direction, strongly developed laminar grain structures and fiber textures are produced via this route.

Route B: The billet is deformed alternatively in two orthogonal directions $(+/-90^0)$ by rotating about the extrusion axis, meaning counter clockwise (CCW) 90^0 after every odd numbered pass and clockwise (CW) 90^0 after every even numbered pass.

Route C: The billet is rotated 180 ° around its axis after each pass. Material elements are deformed at odd-numbered passes and restored to their original forms at each even numbered pass. As a result, heavily deformed but uniform and equiaxed grain structures are created throughout the billet after even number of passes [40, 41].

Route C`: In this sequence, the billet is rotated 90^0 CCW after each pass.

Route A, All passes   Route C', all passes   Route B, N=3,5,9…   Route C, All passes
No Rotation   Route B, N=2,4,6…

N: Number of Passes
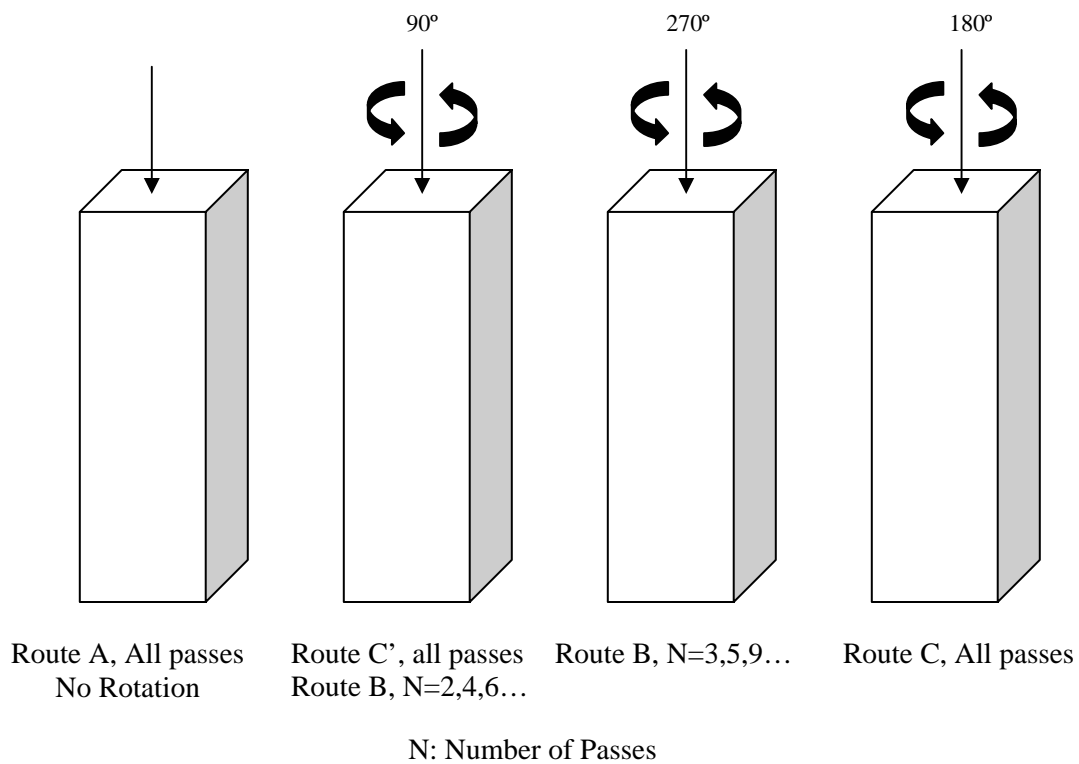
Fig. 1.2.2. Description of ECAE routes.

In general subgrains with low angle grain boundaries (GB) form inside the original grains after the first ECAE pass. These boundaries are not clearly defined indicating an instable state. With the increase in number of passes, these low angle GBs evolve into well defined high angle GBs and the level of grain refinement increases. Also with the same number of passes, the effectiveness of grain refinement increases and the aspect ratio decreases from routes A to B to C and to C' [41-43]. The aspect ratio represents the grain morphology; grains with low aspect ratio are more equiaxed. Due to the anisotropic characteristics of the microstructure developed in ECAE, samples from different planes of the processed billet should be observed to gain a complete understanding of microstructural evolution. This is described in Fig. 1.2.3. The flow plane, transverse plane and the longitudinal plane is indicated by F, T and L respectively throughout this study.

Punch

Longitudinal

Transverse

Flow

Extrusion Direction
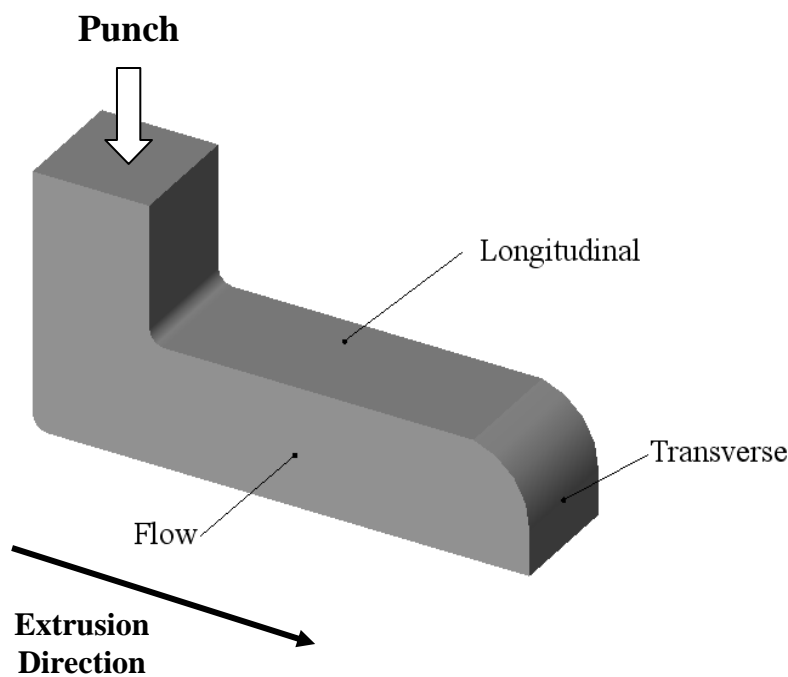
Fig. 1.2.3. Definition of the deformation planes on an extruded billet.

1.3 Deformation Mechanisms

Slip and twinning are the two common mechanisms of plastic deformation in most crystals. Understanding these mechanisms is very crucial in interpreting the resulting mechanical behavior.

1.3.1 Slip Mechanism

Slip or glide involves shearing of crystals on crystallographic planes (slip planes) and in crystallographic directions (slip directions) without a change in the volume of the crystal. Slip direction represented by the unit vector d and the slip plane represented by the unit vector n forms the slip systems for a given crystal. The slip direction should lie within the slip plane, for the material to remain continuous [44]. The initiation of slip depends on the magnitude of stress on a particular slip system. Slip begins when the shear stress reaches a critical value τ_r, the so called critical resolved shear stress. This yield criterion for crystallographic slip is called Schmid`s Law and is represented below [45].

$$\tau_r = \sigma \cdot \cos \lambda \cdot \cos \varphi \qquad (1)$$

λ is defined as the angle between the slip direction and the tensile axis. φ is defined as the angle between the slip plane normal and the tensile axis as seen in Fig. 1.3.1.1.b. In equation (1) $\cos \lambda \cdot \cos \varphi$ is called the Schmid factor. This law implies that the magnitude of the stress acting normally to the slip plane has no influence on the process of slip and slip starts on the slip system with the highest Schmid factor.
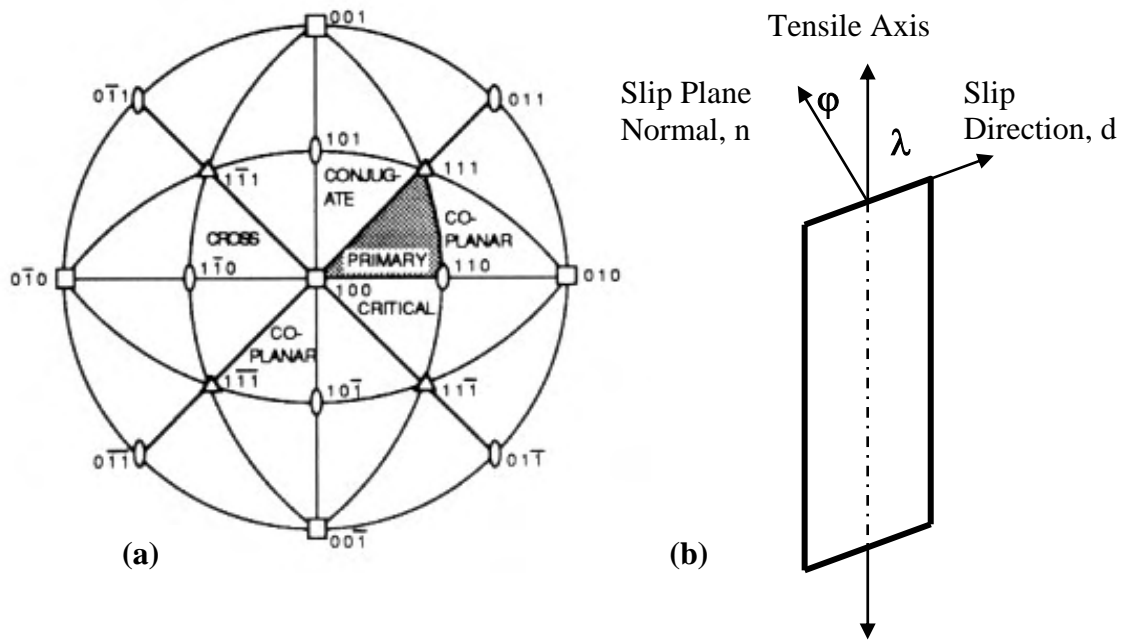
Fig. 1.3.1.1. Demonstration of (a) slip systems for fcc crystals [83] (b) slip elements of a crystal under uniaxial tension.

For fcc crystals slip occurs on the <110>{111} system. This system is made up of 12 individual systems. In bcc crystals slip takes place in the <111> direction and on the {110}, {112}, {123} or on an arbitrary plane of maximum resolved shear stress containing the slip direction. In a hcp crystal, slip can occur on the close packed basal plane (0001), or the $\{1\bar{1}01\}$ and $\{1\bar{1}00\}$ plane families with the common slip direction of $<11\bar{2}0>$. Under special loading conditions or at high temperatures, slip may occur on the $<11\bar{2}3>\{1\bar{1}0\bar{1}\}$ system. It is known that during deformation, the lattice reorients itself to accommodate the deformation leading to texture evolution. As an example, an fcc crystal subjected to uniaxial tension and compression tests will be considered here [45-47]. The tensile axis is represented in the basic stereographic triangle with the [100],

[110] and [111] corners. Except the boundaries, for all orientations in this triangle the

$[101] (11\bar{1})$ system has the highest Schmid factor and therefore called the primary slip

system. If the tensile axis lies on a boundary of the basic triangle, then two systems are

equally favored. The second system which is most favored in the adjoining triangle is

called the conjugate system.

There are three more systems, namely cross slip system, the critical slip system

and the coplanar system [45, 46]. The cross-slip system, $[101] (1\bar{1}\bar{1})$ may activate

when a screw dislocation moving on the primary system encounters an obstacle and

moves onto the cross slip plane. Additionally, coplanar slip systems operate by sharing

the primary slip system with different slip directions. When a crystal is subjected to

tension, the orientation of the tensile axis changes relative to the lattice and rotates

toward the primary slip direction. However, due to constraints, the tensile axis remains

straight and the lattice rotates. Therefore, primary slip on [101] (111) causes the tensile

axis to rotate toward the [101] slip direction. Once it reaches the [100]-[111] boundary,

the primary and conjugate systems are equally favored. So, simultaneous effect of [100]

and [110] slips causes rotation toward [211] along the boundary line. [211] lies on the

great circle through the two slip directions. This behavior is typical of fcc crystals

however exceptions occur for different stacking fault energy materials. Low stacking

fault energy materials may exhibit overshoot in the conjugate triangle before the stable

[211] end orientation. On the other hand, conjugate slip may start before reaching the

[100]-[111] boundary for high stacking fault energy materials. These anomalies occur

due to the differences in hardening of the primary and conjugate systems by slip. Rotation of the crystal in tension and compression is illustrated in Fig. 1.3.1.2.

(a)   **(b)**
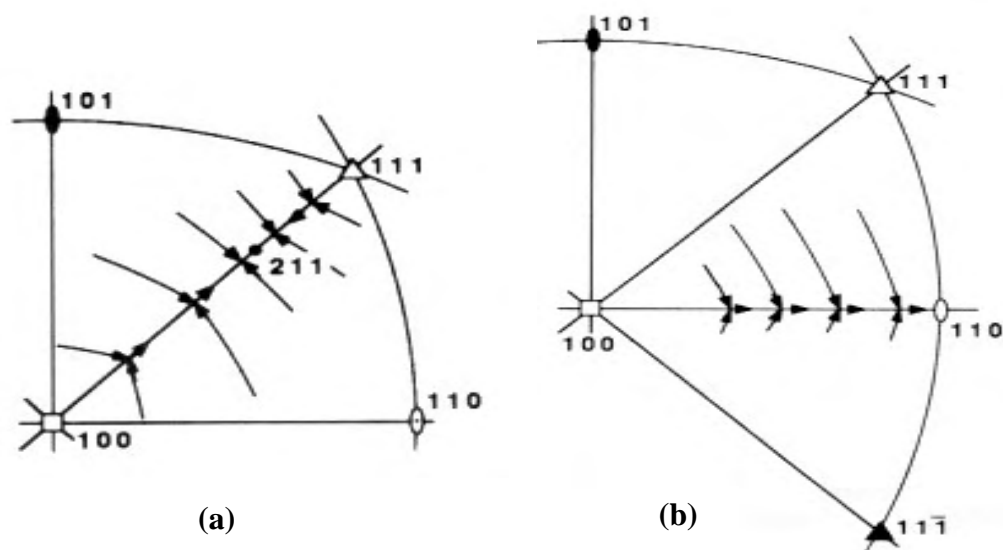
Fig. 1.3.1.2. Loading of single crystals. (a) rotation of the axis toward [211] during tension, (b) rotation of the axis toward [110] during compression [45].

In compression, the axis rotates toward the primary slip plane normal. The compression axis in the basic triangle, rotates toward [111] until it reaches the [100]-[110] boundary. At this point, the primary and critical slip systems are equally favored. The simultaneous activity of these two systems causes a gradual rotation toward [110] stable end orientation. Slip may occur on more than one system. This happens when multiple systems are stressed equally and attain the critical value for slip. For orientations along the boundary lines of the basic triangle two slip systems operate, whereas for corners of the triangle multiple systems are activated. That is, uniaxial stress along [001] activates eight systems, along [111] activates six systems and along [011] activates four systems [44, 46]. Slip in polycrystalline materials differ from single

crystals in a way that extra constraints are imposed on individual crystals. To satisfy the compatibilty, displacements across grain boundaries must be matched. Therefore, grain boundaries restrict the plastic flow and higher yield stress and hardening values are observed in polycrystals. The additional constraints can be met by the operation of five independent slip systems. Failure to supply this condition may result in fracture [45-47].

1.3.2 Twinning Mechanism

Twinning is also a common mechanism of plastic deformation mainly at low temperatures and high deformation rates [45-49]. It is most significant in crystals of low symmetry where five independent slip systems required to satisfy deformation may not be available. A twin is a deformed crystal region in which the lattice orientation is the mirror image of the rest of the crystal. Generally the non-twinned region is called the matrix. As slip, twinning also involves shear deformation on crystallographic planes; however there are some major differences. Twinning shear displacement is a fraction of the interatomic distance while slip displacement is always a whole multiple of the length of the burgers vector. Unlike slip, twinning shear is directional. As an example twinning in fcc crystals occur on the (111) plane in the $[11\bar{2}]$ direction but not in the $[\bar{1}\bar{1}2]$ direction. However, slip in opposite directions but on the same specific plane are equivalent. Moreover, twinning reorients the lattice abruptly in contrast to gradual rotation in slip [45, 48].
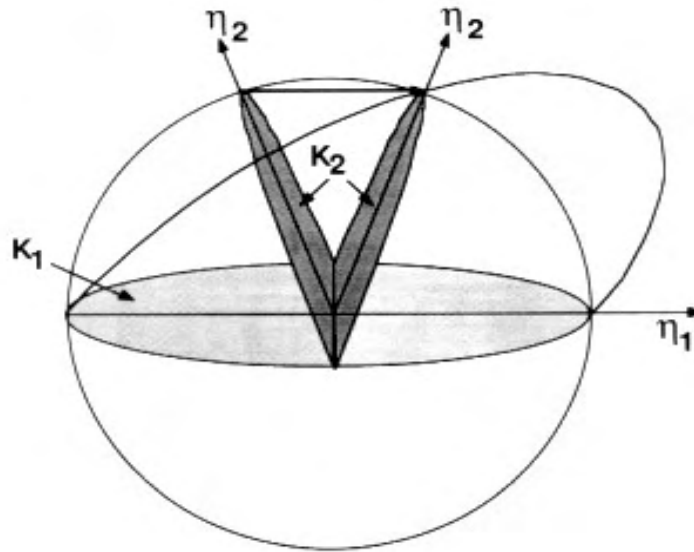
Fig. 1.3.2.1. Formal notation of twinning, showing a homogeneously sheared hemisphere [45].

Fig. 1.3.2.1 describes the hemispherical crystal undergoing twinning shear and its distorted appearance in ellipsoidal shape. Two material planes remain undistorted, that is the twinning plane or the mirror plane denoted by K_1 and the second undistorted plane K_2. Twinning takes place on K_1 and in shear direction η_1. The second direction η_2 lies in K_2 being perpendicular to the intersection of K_1 and K_2. η_2 is the only direction in K_2 that makes the same angle before and after twinning with any direction in K_1. K_1, K_2, η_1 and η_2 are the twinning elements. The plane containing η_1, η_2 and the normals to K_1, K_2 is the shear plane [50]. The twinning planes and directions for different crystal structures are tabulated in Table 1.3.2.1.

Table 1.3.2.1

Twinning elements in different crystal structures [46].

Twinning Elements for various Crystal Structures				
Structure	K_1	K_2	$\eta 1$	$\eta 2$
fcc	$\{111\}$	$\{11\bar{1}\}$	$<11\bar{2}>$	$<112>$
bcc	$\{112\}$	$\{11\bar{2}\}$	$<11\bar{1}>$	$<111>$
hcp	$\{10\bar{1}2\}$	$\{\bar{1}012\}$	$<10\bar{1}1>$	$<\bar{1}011>$

The shapes of deformation twins are generally lenticular and sharply pointed. The shape is related to the overall energy change during the formation of a twin. Two main factors influence this energy change. One of them is the introduction of a new surface and the resulting surface energy. The other is the strain energy created at the twin-matrix interface due to the plastic shear in the twinned area. The misfit between the matrix and the twin should be accommodated by elastic distortion of the matrix. This naturally requires energy, and is minimized when the twin is narrow and long. It is expected to have high aspect ratio twins when they are formed with a high shear strain. It is found that while fcc and bcc twins are thin, the twins in hcp metals are thicker [48-50].

1.3.3 Factors Affecting Twinning

Twinning behavior is influenced by many variables. These include temperature; strain rate; grain size, crystal orientation, texture and alloy composition. It should be noted that all these variables affect the way the material deforms. In this respect, stacking fault energy is an important factor in tendency towards twinning deformation.

In contrast to high SFE materials, where cross-slip is readily observed and random dislocation networks are formed, linear dislocation arrays and stacking faults are observed in low SFE materials [49, 51].

It has been reported that the orientation of the stress axis is important on the resulting formation of a twin. The twin variant selected is always of the variant for which the resolved shear stress is the highest. Therefore, single crystals or textured polycrystalline materials show difference in their twinned volume fractions for tension and compression. Twinning generally shows increased activity at lower temperatures due to less increase in the stress required for twinning compared to the increase in the stress required for slip. Decrease in deformation temperature may also lead to the formation of planar dislocations, which reduce the ability of a material to cross-slip causing the early onset of twinning. Fcc metals with low SFE and at low temperatures form localized fine twins with a homogeneous deformation structure while at higher temperatures thicker twins with localized flow may be demonstrated [49, 50].

Twinning stress is very sensitive to strain rate and under shock loading or severe deformation conditions deformation by twinning is frequently observed. Fcc materials with high SFE do not twin under normal conditions, however twinning has been observed in shock loaded Al-Mg alloys at low temperatures. This was attributed to the solid solution strengthening together with the greater increase in flow stress at low temperatures under dynamic loading than twinning stress [52]. Like slip, twinning is also hindered at grain boundaries from further growth. The twinning stress varies according to the grain size and a relation similar to the Hall-Petch relation as seen in equation 2,

can be written in which the twinning stress may increase linearly with d^{-1} [53]. In equation (2) σ_y^t is the twinning stress.

$$\sigma_y^t = \sigma_0^t + k^t \cdot d^{-\frac{1}{m}} \qquad (2)$$

Additionally the size of a twin is restricted by the grain size, and shorter twins are observed in refined structures. The chemical composition is also an important parameter, in a sense that it affects the SFE and the mobility of the screw dislocations. Lower SFE values are obtained with the addition of substitutional solute atoms in SFE, leading to increased twinning activity [45, 49-51]. Twinning as an alternative mode of deformation is responsible for strengthening and high work hardening. Twinning as an obstacle to slip and growing twins, act in the same way as grain boundaries and cause strengthening.

1.3.4 Twin-Slip and Twin-Twin Interactions

When a twin penetrates a slip band with a high density of dislocations, individual dislocations interact with the twin interface. Inversely, penetration of slip dislocations into a twin forming an obstacle to slip path is also common. A growing twin interacting with a glide line changes the orientation of the slip within the twin due to the twinning shear. It is also possible that the slip dislocations dissociate into other dislocations in the obstacle twin. If the incident dislocations from up a pile up pressing against the twin interface, the twins may branch or even fragment. Twin-twin interactions occur when annealing twins or existing deformation twins meet a growing deformation twin. The amount of shear by incident twin transferred beyond the existing twin depends on the

interactions taking place. The incident twin (I) can cross the obstacle twin (O) by forming a secondary twin (S) in the crossed region [49]. Two conditions are necessary for this to happen as explained by Cahn [50]. The K_1 planes of I and S must intersect that of O in the same direction and the direction η_1 the magnitude and sense of shear in I and S must be the same. Both twin-slip and twin-twin interactions may be responsible for microcracks formed in the vicinity of the intersections due to high stresses present.

1.4 Deformation Texture in Metals

Crystallographic texture is formed during deformation, solidification, phase transformation, recrystallization and grain growth. Deformation textures are formed after thermomechanical treatments and gain importance due to their effect on the mechanical properties. Textured materials usually exhibit anisotropic properties. Deformation texture is dependent on crystal structure, chemical composition, the nature, rate and amount of the deformation and temperature [45, 54]. In the following sections, common rolling and torsion textures of fcc and hcp metals and the effect of ECAE on texture evolution are discussed.

1.4.1 Rolling Textures

These textures are specified by crystallographic direction [uvw] parallel to the direction of rolling and by crystallographic plane (hkl) parallel to the rolling plane. They can also be referred as sheet textures. A higher rolling reduction generally produces a sharper texture, namely a decrease in scatter of orientations [55]. However, the locations of the peaks in the pole figures may shift considerably. This should be taken into account especially when analyzing textures in terms of fibers. Sometimes, it may be complex to

interpret the rolling texture. For fcc metals, two distinctive types of texture can be identified. Copper texture concentrated around (123)[421] and (146)[211] is seen in pure metals with generally high stacking fault energy. Brass texture represented (110)[112] is observed in alloys with lower stacking fault energy. Stephens [56] studied the effect of composition on texture by demonstrating the texture of 96% rolled copper with different Zn contents. It is reported that above 15% Zn concentration, there is a transition from pure metal to alloy type texture. It is known that addition of solutes to pure metal decreases the stacking fault energy. In addition, elevated deformation temperatures leads to copper texture, while brass texture is apparent at lower temperatures [57].

The textures of rolled hcp materials can be categorized into three groups according to their c/a ratios. For c/a ratio greater than 1.633 such as zinc and cadmium, textures with basal poles tilted 15° to 25° away from the normal direction toward the rolling direction are exhibited. For c/a ratio equals to 1.633 such as magnesium or cobalt, [0001] fiber textures tend to form. For c/a ratios lower than 1.633 such as zirconium and titanium, textures with basal poles tilted 20° to 40° away from the normal direction toward the transverse direction and [1010] poles are aligned with the rolling direction [55, 58].

1.4.2 Torsion Textures

This type of texture demonstrates the lattice orientation under simple shear and therefore gives insight about texture formation after ECAE. For fcc materials three different ideal orientations for shear texture have been proposed [55, 59]: The 'A' partial fiber can be indexed as {111}<uvw>, the 'B' partial fiber as {hkl}<110> and the 'C'

orientation as {001}<110>. The 'C' position is a special variation of the 'B' fiber texture. Recent work revealed the existence of another fiber. In the [111] pole figure it appears similar to the 'A' fiber but is rotated 90° about the pole figure center. One particular component, which is sometimes predominant in this 'D' fiber, is {112}<110>. Variation of torsion texture with material has been investigated. It has been shown that high stacking fault energy materials such as nickel and copper exhibit a strong 'B' fiber and a weak but non-zero intensity 'A' fiber texture [55]. For silver, similar B fiber texture exists and the A fiber is absent and replaced by the 'D' fiber. The strength of the 'D' fiber is dominated in Ni60Co. For copper deformed at 400 ^{o}C, it is seen the dominant fiber 'A' is replaced by 'D' [60].

Torsion textures for hcp metals are dependent on the ratio of the reduction in wall thickness (R_w) to reduction in diameter (R_i). For $R_w/R_i = 1$, the texture is similar to a fiber texture whereas, for $R_w/R_i > 1$, the texture is similar to a rolling texture [54, 55].

1.5 Effects of ECAE on Texture

ECAE deformation produces texture similar to simple shear texture. In general, the textures found in ECAE material are relatively weak compared to those seen on rolling to equivalent strains [61–65]. This is normal since the torsion textures are also found to be weak, due to the lower deformation symmetry and material rotation during simple shear deformation [63, 64]. However, the possibility of changing the billet orientation by rotating it between each extrusion cycle gives rise to complex strain paths that can further complicate the textural evolution.

Studies on texture development of ECAE processed materials mainly concerned easy to work metals such as aluminum, copper and magnesium in pure and alloy form, pure iron and silver [61-71]. Work on the textures generated during ECAE processing of Cu and Al have noted the presence of the {100}<110> and {112}<110> components on the partial B fiber. However, although the texture is always symmetric in the mirror plane of the die, that is the flow plane; the positions of maximum intensity have been reported to be rotated away from the transverse direction by 10–20°. This has been explained by assuming that the <110> B fiber aligns with the shear plane rather than the axis of the extruded billet [61, 65-67]. Work on copper by Huang et al. [61] showed that the resulting texture can be conveniently represented by the ideal torsion orientations of {111}<110>, {111}<112>, {112}<110> and {001}<110>. They reported that the pole intensity contours do not have mirror symmetry about the flow direction in the pole figures, as opposed to what is expected. However, the pole figures are symmetrical about the flow plane, reflecting the symmetry of the deformation process given by ECAE. Similar results were also reported by Agnew et al. [67]. Aluminum and its alloys were also studied frequently [63, 68]. The studies by Gholinia et al. [68] on Al-0.13% Mg alloy processed at room temperature up to 4, 8 and 12 passes following route A demonstrated that in all the (111) pole figures three peaks associated with the <110> B fiber along the symmetry plane of the die occur. The main texture components were reported as {001}<110> and {112}<110>. The texture intensity initially strengthened with increasing levels of strain, and weakens at very high strains occur after 12 passes.

In contrast Pithan et al. [69] demonstrated strong textures for Al-4.56%Mg alloy deformed up to 8 passes following route C at 200 ^{o}C. They reported that above 4 passes of ECAE a texture transition occurs and that another, second ideal orientation besides copper orientation {112}<111> predominates in the deformation texture. With increasing intensity a component close to the brass orientation {110}<112> develops.

The simple shear texture of silver have been reported to be {112}<110>. The materials processed at room temperature following route 3A exhibited similar components with some shift due to the geometry of the deformation process. On the other hand, iron processed via route B exhibits a fiber texture, with <110> aligned parallel to the wire axis or the extrusion axis for ECAE processed material [70]. Agnew et al. [71] severely deformed a conventional extruded Mg alloy utilizing ECAE for 8 passes following route B at 200 ^{o}C. They found that the typical magnesium fiber texture of <100> and <110> fibers representing the basal poles aligned perpendicular to the extrusion direction changed to a preferred orientation with the basal planes inclined 45° to the bar axis, namely coinciding with the shear plane.

To the best of author`s knowledge, there has been no work reported on the texture development of severely deformed difficult-to-work alloys, possibly due to the small number of extrusion passes preventing a complete understanding of texture development. In this respect, this study will be a first attempt in the area, documenting the texture evolution of a severely deformed austenitic stainless steel where twinning is highly active.

1.6 Previous Studies on Ti-6Al-4V

Ti-6Al-4V (Ti64) is one of the most widely used titanium alloys. Being an alpha-beta ($\alpha-\beta$) two phase alloy it contains 6 wt% Al and 4 wt% V. The alpha phase has hcp crystal structure while the beta phase has bcc crystal structure. This alloy is typically utilized in aerospace applications for the production of structural parts, turbine disks and compressor blades, in pressure vessels, and in biomedical industry for surgical implants. High strength and toughness combined with excellent corrosion resistance are the main reasons that make this alloy favorable for the mentioned applications. At room temperature the microstructure is mainly composed of primary and secondary hcp α grains. Fig. 1.6.1 shows the phase diagram of this alloy. Above 650 °C, hcp α transforms to BCC β grains. α begins to form with slowly cooling from the β region passing through β transus (about 980 ^{o}C). α forms in plates with a crystallographic relation to the β. The α plates form with their basal plane perpendicular to the $(\bar{1}12)$ plane in the β phase [19, 72]. Because of the close packing along this common plane, the α phase thickens relatively slowly perpendicular to this plane but thickens faster parallel to it and plates are developed [19]. The microstructure has the form of parallel plates of α delineated by the β phase between them. α plates forming along different planes of β meet and high angle grain boundaries form. This morphology is called the widmanstatten structure.
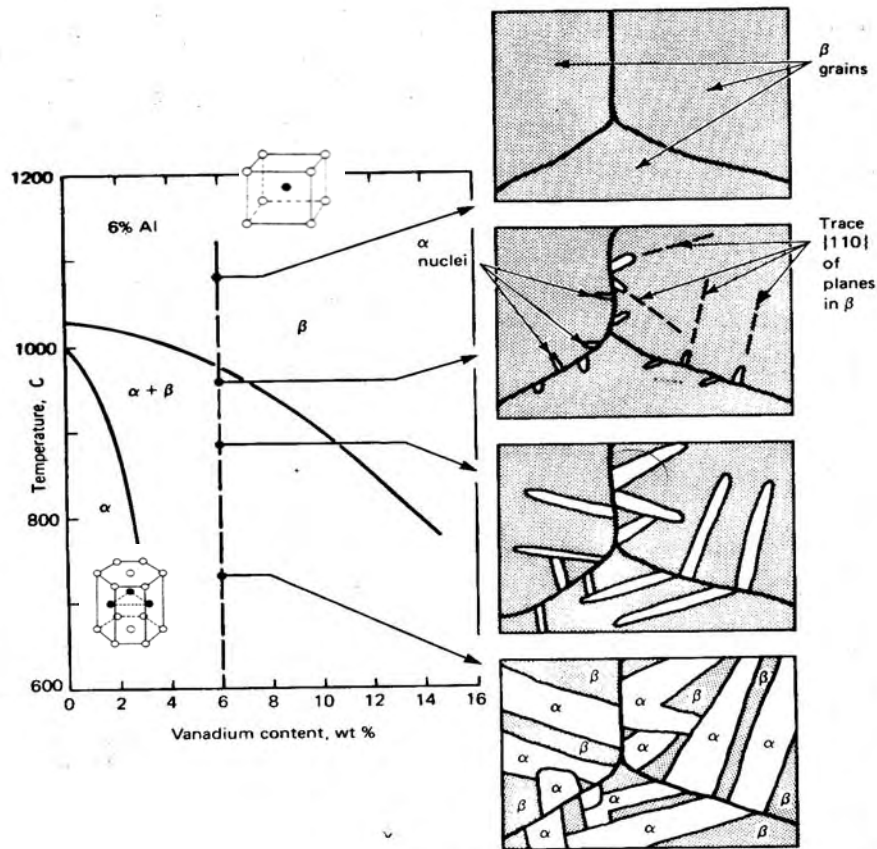
Fig. 1.6.1. Phase diagram of Ti-6Al-4V alloy [19].

On the other hand, slow cooling from below the β transus will lead to the formation of primary α grains. In this process, no α lamellae are formed within the β grains resulting in a fully equiaxed microstructure. Typically the equiaxed α size and spacing is controlled during α-β working, while the lamellae spacing is defined by the rate of cooling from the α-β working temperature or the subsequent solution treatment temperature [22, 72].

From the few studies focusing on ECAE processing of Ti64, the work of Semiatin and DeLo [15] attracts attention. Initial material with lamellar alpha

microstructure is deformed by ECAE non-isothermally. The die is preheated to 300 $^{\circ}$C and the billets are extruded at temperatures ranging from 900 to 985 $^{\circ}$C. They found that shear localization and surface cracking occurred at temperatures below 900 $^{\circ}$C and strain rates above 0.05 sec^{-1}. Comparison of these results with isothermal compression tests [73] suggests that at least part of the underlying cause for the presence of the shear localization and cracking may be due to the die chilling effects. Additionally, they have shown that initial upsetting during ECAE promotes flow uniformity for materials that exhibit decreasing degrees of flow softening with the increase in strain. This was attributed to the greater stability of upsetting as compared to simple shear. Indeed, Ko et al. [16] have recently been successful in isothermal ECAE processing of Ti64 at temperatures above 600°C. One drawback of isothermal extrusion is the reduced die life at such high temperatures. In addition, no mechanical properties of processed materials were reported in these studies. In a recent study by Kim et al. [74], it was found out that the initial microstructure has a remarkable effect on the flow localization and stated that ECAE processed Ti64 with initial equiaxed microstructure experiences uniform flow, whereas initial widmanstatten microstructure leads to localized flow with surface segments especially at the colony boundaries. Mishra et al. [75] reported the mechanical behavior of nanocrystalline Ti64 torsinal strained to a true strain of 6. They conducted tension tests at different temperatures and strain rates and reported improved strength and ductility at elevated temperatures. Similarly, Sergueeva et al. [76] used high pressure torsion to severely deform Ti64 and reported the room temperature mechanical properties of the as processed materials. In high pressure torsion, a disk shaped sample is

placed between two vertically opposed anvils. With high pressure imposed on the upper anvil, lower anvil starts rotating and surface friction forces deform the sample by shear [77]. Although this method is also very effective in producing severely deformed microstructures, the dimensions of the processed disk shaped samples are small, usually not exceeding 20 mm in diameter and 1 mm in thickness. Additionally, it is hard to keep track of the deformation conditions and constraints since it depends on the friction between the sample and the rotating anvil. Apart from these, a few studies [11-14] are noticeable in terms of demonstrating the mechanical behavior at a wide range of temperatures and strain rates. Meyer [11] investigated the tensile and compressive behavior of Ti64 at a variety of strain rates. Maiden et al. [12] also reported the compressive behavior of Ti64 at various strain rates. Both studies reported increased tensile and compressive flow strengths at high strain rate tests compared to low strain rate ones. The mechanical test results from these studies are presented in Figs. 1.6.2 and 1.6.3. Johnson et al. [13] reported similar compressive behavior for samples prepared from the same parent material with equiaxed and widmanstatten microstructures. Results from Frary et al. [78] are also included in Fig. 1.6.2 representing the tensile behavior of Ti64 alloy produced by a similar powder metallurgy process as in this study.
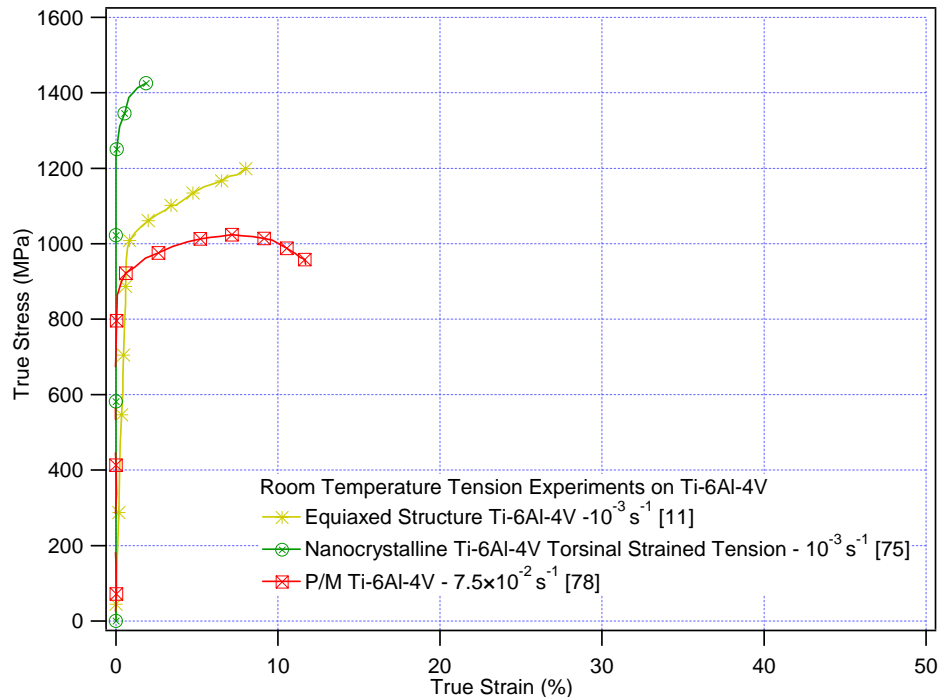
Fig. 1.6.2. Tensile response of Ti-6Al-4V with different microstructures under different strain rates.
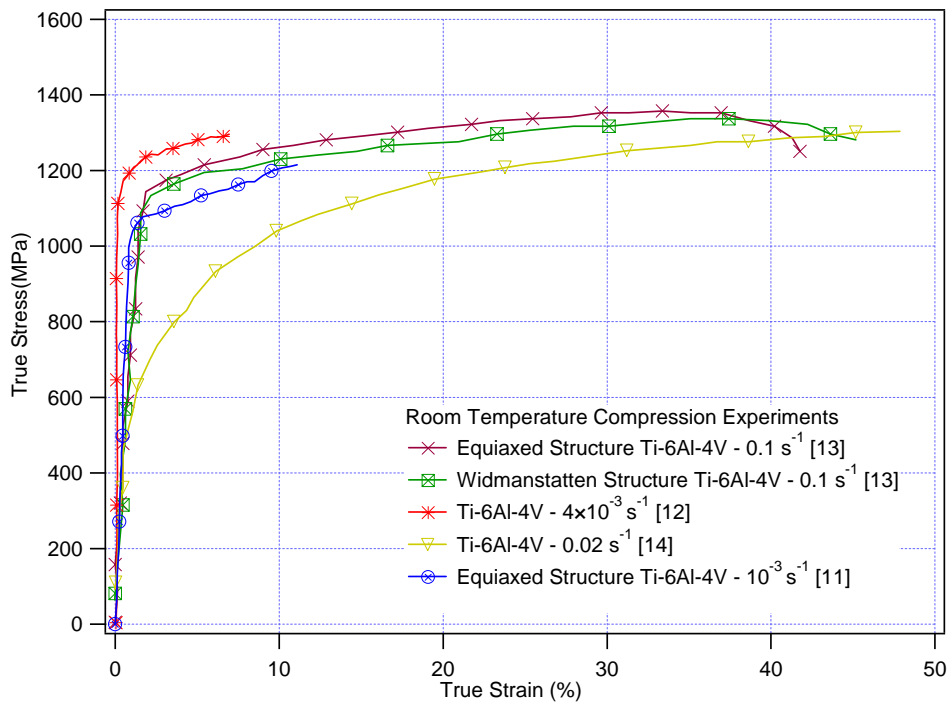
Fig. 1.6.3. Compressive response of Ti-6Al-4V deformed at a variety of strain rates.

1.7 Previous Studies on Ti-6Al-4V + 10% TiC

This research material was chosen to investigate the effect of ECAE on microstructure and the resulting mechanical behavior of a Ti64 metal matrix composite. Metal matrix composites are developed to achieve better mechanical and physical properties than the matrix by reinforcing it. Fibers used for reinforcing have very high strength and stiffness. Titanium matrix composite materials can be strengthened by reinforcement of continuous fibers, or discontinuous particulates [79, 80]. While TiC, TiB and TiAl are the general ceramic and intermetallics used for particulate reinforcement, SiC is used for continuous reinforcement [81]. This research material contains 10 vol% TiC particulates in Ti64 matrix. TiC particulates dispersed in the matrix provides greater stiffness and increases the wear resistance. Discontinuous reinforcement is advantageous compared to continuous in terms of the opportunities of creating complex geometries. Powder metallurgy (P/M) techniques should be employed for production. Near net shape parts can be produced by cold isostatic pressing. The most important considerations in producing titanium P/M components are oxygen content, purity and contaminants. Powders must be handled very carefully because of the high affinity for oxygen. Purity is critical for the consolidation of the blended elemental powders. Contaminants are detrimental to fatigue properties. With near net shape processing capability, uniform grain structure results in comparable strength levels to wrought products [79, 81].

There has been no report identifying the mechanical behavior of severely deformed Ti64/TiC. Kim et al. [82] demonstrated the fracture behavior and mechanical

properties of near fully densified Ti64/TiC metal matrix composite produced by in-situ gas solid reaction of blended elemental powders. They reported that the composite has a higher stiffness, strength, hardness and wear resistance than the wrought alloy. Gorsse and Miracle [83] studied the effect of composition and reinforcement alignment (ie: aligned vs randomly distributed) on the mechanical behavior of Ti64/TiB composite. They concluded that fine grained matrix with homogeneously distributed fine whiskers is needed for improved strength and ductility in reinforced titanium. Likewise, Soboyejo et al. [84] and Srivatsan et al. [85] and indicated a slight improvement in ambient yield strength of Ti64/TiB over the unreinforced matrix. Galvez et al. [86] revealed the effect of strain rate on the deformation behavior of Ti64 uniaxially reinforced with continuous SiC fibers. They concluded that increase in strain rate leads to increase in the strength of the MMC. In addition it is reported [87] that the addition of TiC leads to improved creep resistance. Zhu et al. [88] proposed that the TiC particulates improve the creep properties of the composite by altering the matrix microstructure. The addition of the TiC particulates to Ti64 alloy leads to a general refinement in the microstructure, resulting in finer α/β colony size. The α/β boundaries act as barriers to dislocation slip, resulting in improved creep properties in the composite. Another study by Frary et al. [78] reported the tensile behavior of Ti64 reinforced with 10 wt% W at room temperature. The material was processed by combined cold and hot isostatic pressing and demonstrated significant improvements in yield and ultimate tensile strengths with an acceptable reduction in ductility compared with the unreinforced matrix. The results from the aforementioned studies are summarized in Fig. 1.7.1.
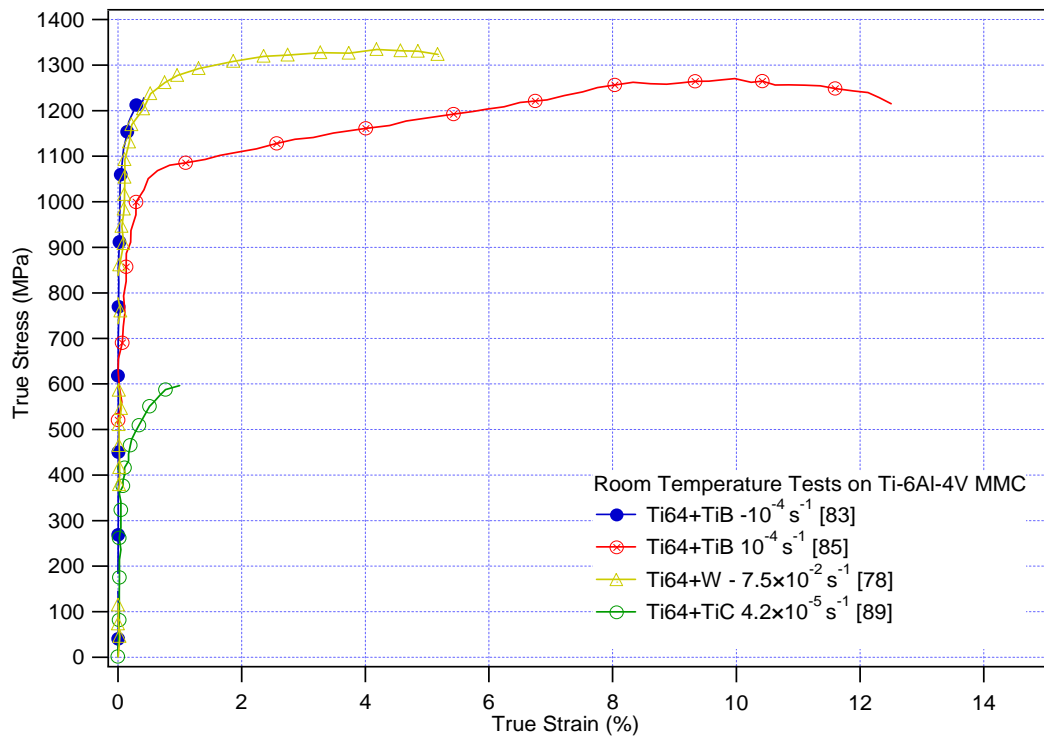
Fig. 1.7.1. Tensile response of Ti-6Al-4V with different reinforcements under different strain rates.

1.8 Previous Studies on AISI 316L

Austenitic stainless steels are non-magnetic and contain 18-25 wt% Cr and 8-20 wt% Ni and are low on C (between 0.03 wt% and 0.25 wt%). They are predominantly austenitic at all temperatures, although depending on composition and thermomechanical history some delta ferrite may be present [89-91]. Presence of nickel and chromium brings high temperature strength and oxidation resistance. The composition of AISI 316L stainless steel provides good corrosion and pitting resistance and high temperature mechanical properties [90-92].

Being one of the most widely used structural materials, bulk stainless steels need improved mechanical properties to gain a wider range of applications. Grain refinement

is a convenient way of achieving this without changing the chemical composition. This can be accomplished through severe plastic deformation [93-97] or thermomechanical processing [98-100]. Several studies have focused on the deformation characteristics of austenitic stainless steels in a wide range of temperatures [101-105]. However the properties of ECAE processed austenitic stainless steels have not yet been investigated. Belyakov et al. [96, 105] investigated the severe deformation of 304 stainless steel by repeated uniaxial compression at elevated temperatures. Equiaxed fine grains with a couple of hundred nanometer grain size and high angle grain boundaries were developed. Dobatkin [97] studied the grain refinement of austenitic stainless steels during SePD by high pressure torsion at low temperatures which was facilitated by martensitic transformation. However, resulting mechanical properties were not reported.

In contrast, severely deformed low carbon bulk steel has been a work of many researchers utilizing ECAE. These studies will not be mentioned here but can be found in detail elsewhere. [106-109].

1.9 Statement of Objectives

The objectives of this research are:

1. Uniformly deforming hard materials at temperatures low enough to enable the formation of refined microstructures with improved mechanical properties.

2. Investigating microstructures developed during SPD by varying the temperature and the route performed.

3. Demonstrating room temperature mechanical properties of extruded billets and report any improvement.

4. Correlating the mechanical properties with the mictrostructures created during ECAE.

5. Investigating the effect of texture created on the mechanical properties. Report the existence of any tension/compression asymmetry due to texture.

6. Demonstrating the effect of refinement in alpha and beta phase on the mechanical behavior of Ti-6Al-4V.

7. Reporting any change in the distribution of second phase particles in the Ti-6Al-4V matrix and tailoring them to obtain improved mechanical properties.

8. Demonstrating the activation of competing deformation mechanisms, slip vs twinning in AISI 316L stainless steel.

CHAPTER II

EXPERIMENTAL METHODS

Three research materials were investigated. Commercially available AISI 316L stainless steel, initially hot rolled and solution treated at 1050°C had a composition of 16.9% Cr, 10.3% Ni, 2.14% Mo, 1.64% Mn, 0.17% Si, 0.08% N, 0.019% C in weight and Fe balance and was supplied from Villares Metals. Ti6Al4V and Ti6Al4V+10%TiC were supplied from Dynamet Corporation, in the form of cylindrical rods with diameters of 10 mm. They were fabricated by blending powder, cold isostatically pressing at 380 kPa and vacuum sintering at 1230 °C for 4 hrs. This was followed by hot isostatically pressing at 100 kPa and 900°C for 2 hrs followed by furnace cooling. For SS 316L, 15 cm long bulk bars were cut and coated with a graphite base lubricant before extrusion. They were heated in an electric resistance furnace to the deformation temperature where they were held for 1 hour before both first and second passes. Finally they were transferred to the 25.4×25.4 mm cross section angle ECAE die, preheated to 300 °C.

Extrusions were performed at a rate of 12.7 mm/sec. Extruded billets were water quenched after processing to assist in maintaining the microstructure produced by ECAE. For Ti64 and Ti64+10%TiC, the billets were inserted into 25.4×25.4 mm rectangular stainless steel cans coated with a lubricant and heated to deformation temperatures and maintained for 1 hour between each ECAE pass. Shielding the extrusion material with cans was done to prevent shear localization due to die chilling, to minimize tool wear and to conduct a smoother extrusion process. Similar with SS 316L,

the die is preheated to 300 °C, and the extrusions are held at a rate of 12.7 mm/sec. Following extrusion, the billets were water quenched. Although coating with lubricant, very high loads were seen during extrusion. Therefore, a maximum of two passes could be performed for SS 316L and Ti64, where only one pass could be performed for Ti64+10%TiC. The minimum extrusion temperature that could be attained was 400 °C for SS 316L, 550 °C for Ti64 and only 700 °C for Ti64+10%TiC. For Ti64 alloys, the extrusion temperatures were selected in the α-β phase region, and the minimum extrusion temperature of 550°C was selected because below which Ti$_3$Al precipitation is likely to occur [22]. Table 2.1 summarizes the extrusion conditions for the processed billets. Processed materials have been characterized utilizing several techniques including optical microscopy, transmission electron microscopy (TEM), scanning electron microscopy (SEM), mechanical experiments, harness tests and texture analysis.

Table 2.1

Processing parameters of the extrusions held throughout the research.

	Temperature (°C)	Route	Max. Load (kN)
T i 6 4	550	1A	1388
	600	2A	1090
	700	1A	614
	800	1A	1201
	800	2A	934
Ti64+TiC	700	1A	1148
	800	1A	738
3 1 6 L	450	1A	1076
	550	1A	956
	600	2B	823
	700	1A	881
	800	1A	934

Optical microscopy samples of Ti64, Ti64+10%TiC and SS316L were prepared following the steps of sectioning, mounting, polishing, and etching. Sectioning was done with a Buehler Isomet 1000 diamond saw using a water based lubricant. The sectioned samples were mounted in fast cure epoxy. Grinding of samples was performed by abrasive removal of material from the material surface. The purpose of grinding and polishing is to produce a suitable surface for microstructural evaluation by means of step-by-step removal of deformed material, therefore silicon carbide papers of 400, 600, 800 and 1200 Grit were sequentially applied. As a final step, polishing of samples using 3μ, 1μm diamond paste and alumina powder on a special cloth was performed. Etching of 316L is performed with Marble`s reagent (5 g $CuSO_4$ + 20 ml HCl in 50 ml distilled water) for 10 seconds and etching of Ti64 and Ti64+10%TiC is performed with Kroll`s reagent (2 ml HF + 5 ml HNO_3 in 100 ml distilled water) for 25 seconds.

TEM study was performed on as-received and as-processed 316L and Ti64 samples. Samples for TEM observation were prepared by grinding, mechanical polishing of slices down to 100 μm, punching 3 mm disks. Ti64 thin foils were twin-jet electropolished with a 20 volume % H_2SO_4 in a methanol solution, whereas SS 316L foils were dimpled and ion milled. Thin foils were examined in a JEOL 2010 transmission electron microscope (TEM) operated at 200 kV. Examination was done on the Ti64 samples cut from the flow plane of the processed billets, while SS 316L samples observed were cut from all three planes (F, L, T) of the processed billets.

SEM study was performed for secondary electron imaging of as-received and as-processed Ti64 and Ti64+10%TiC samples. This study was more essential in terms of a

higher imaging quality of the TiC samples in the Ti64 matrix. The same samples prepared for optical microscopy were utilized in the SEM study. The epoxy mounts were carbon taped to enable conductivity between the sample and the sample holder.

Mechanical behavior of the as-received and as-processed samples were explored using a MTS servo-hydraulic test frame controlled with a Teststar II system. The tests are done by displacement control during loading and force control during unloading. Both monotonic tension and compression tests were performed. The tension samples had a dog-bone shape with a gage section of 1.5 mm x 3 mm x 8 mm. The compression samples were rectangular blocks with dimensions 4 mm x 4 mm x 8 mm. These samples are presented in Fig. 2.1.
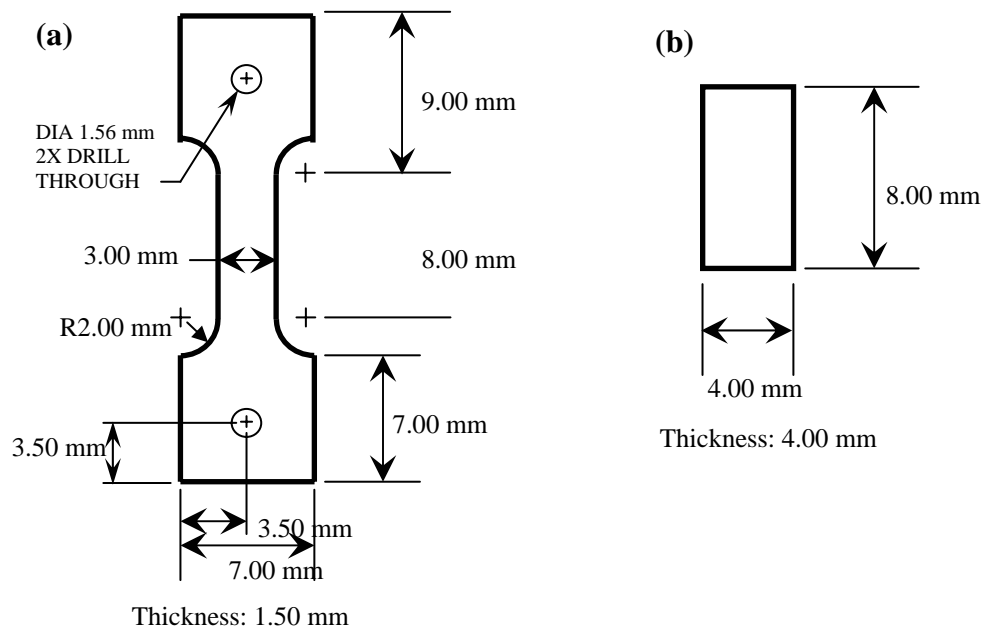
Fig. 2.1. Schematics representing the (a) tension and (b) compression samples used in this study.

The tension samples were oriented parallel to the extrusion direction for all the research materials. For SS 316L, compression axis was parallel to the extrusion direction, whereas for Ti64 and Ti64+10%TiC, compression axis was perpendicular to the extrusion direction. SS 316L samples were tested at a strain rate of $5x10^{-4}$ s^{-1} both in tension and compression. Ti64 and Ti64+10%TiC samples were tested at a strain rate of $1x10^{-4}$ s^{-1} and $1x10^{-3}$ s^{-1} in tension and at a strain rate of $1x10^{-3}$ s^{-1} in compression. The strains were measured using a miniature 3mm gage length extensometer. Experiments were repeated on two to three companion specimens to check repeatability and minimize any errors due to shape effects.

As another indication of mechanical strength, hardness tests were done by using Buehler Micromet II digital microhardness test machine. The working principle of microhardness testing is forcing a diamond indenter of specific geometry into the polished surface of the samples. The Vickers hardness number (Hv) is determined by calculating the ratio of the applied load to the area indented on the sample surface [110]. Area indented is determined by measuring the length of the diagonals of the indentation. All these calculations are done automatically with the current apparatus. The geometry of the indenter is a square based pyramidal diamond with face angles of 136°. In Vickers microhardness testing applied loads generally do not exceed 1kgf. For all the research materials, 500gf load is applied for 13 seconds and average of at least 10 measurements was used after removing the outlying highest and lowest values to determine representative hardness values of the specimens.

Additionally, macrotexture analysis on SS 316L was performed to see the effect ECAE processing on the textural evolution. Texture data was obtained on the transverse plane of the extruded billets to reveal the orientation dependence of post-processing mechanical behavior.   Texture measurements were conducted at University of Paderborn, Germany using a Philips X'Pert system with Cu Kα radiation. A minimum of three hkl planes was analyzed and inverse pole figures were calculated from this using popLA software [111]. A brief summary of the experimental methods is given in Fig. 2.2.
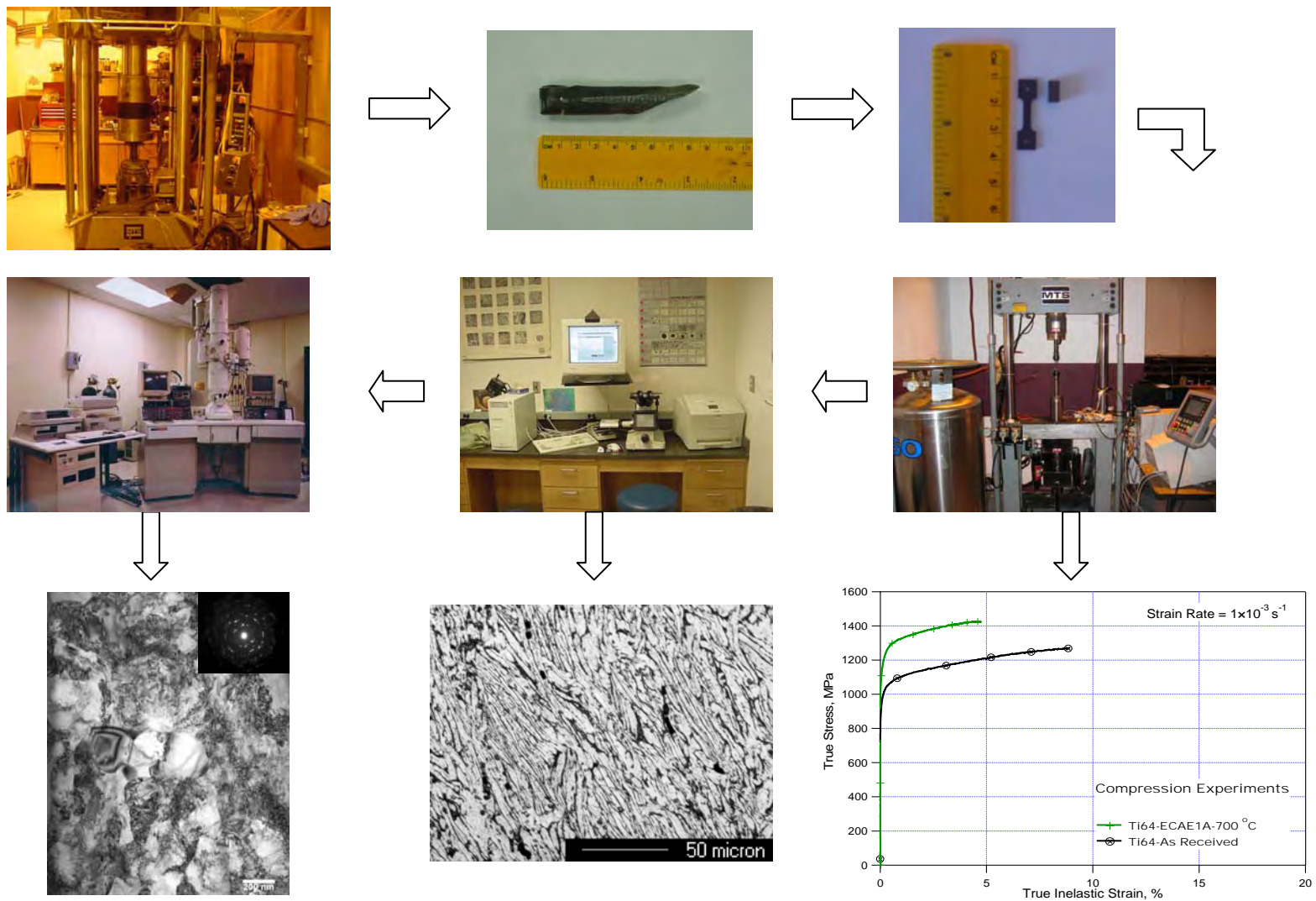
Fig. 2.2. Summary of experimental methods utilized throughout the research.

CHAPTER III

RESULTS & DISCUSSIONS ON Ti-6Al-4V

This section will demonstrate microstructural examinations and mechanical behavior results pertaining to Ti-6Al-4V intermetallic.

3.1 Microstructural Evolution

The as-received material had a coarse lamella colony α structure with an average colony size of 70 μm and a lamellae α plate size of 17 μm without distinct prior β phase boundaries as seen in Fig. 3.1.1.a. The α colonies had near equiaxed morphology with lamellar plates separated by thin β strips.

Visual examination of the de-canned samples indicate that they had deformed uniformly at all extrusion temperatures with the leading edge having near the theoretical shear angle as seen in Fig. 3.1.2. Indeed only the rear portion of the sample extruded at 550°C being the lowest deformation temperature demonstrated any evidence of non-uniform flow. The uniformity of deformation at temperatures as low as 550°C confirms the importance of eliminating die chilling during ECAE of hard to deform materials. Figs. 3.1.1.b through 3.1.1.f summarizes the microstructure evolution observed during ECAE. They show that:

1. Simple shear during ECAE helps eliminate the lamellae colony structure.

2. The α plate size decreases with decreasing temperature and with increasing number of passes.

(a)　　　　　　　　　　　　　　　　(b)

(c)　　　　　　　　　　　　　　　　(d)

(e)　　　　　　　　　　　　　　　　(f)
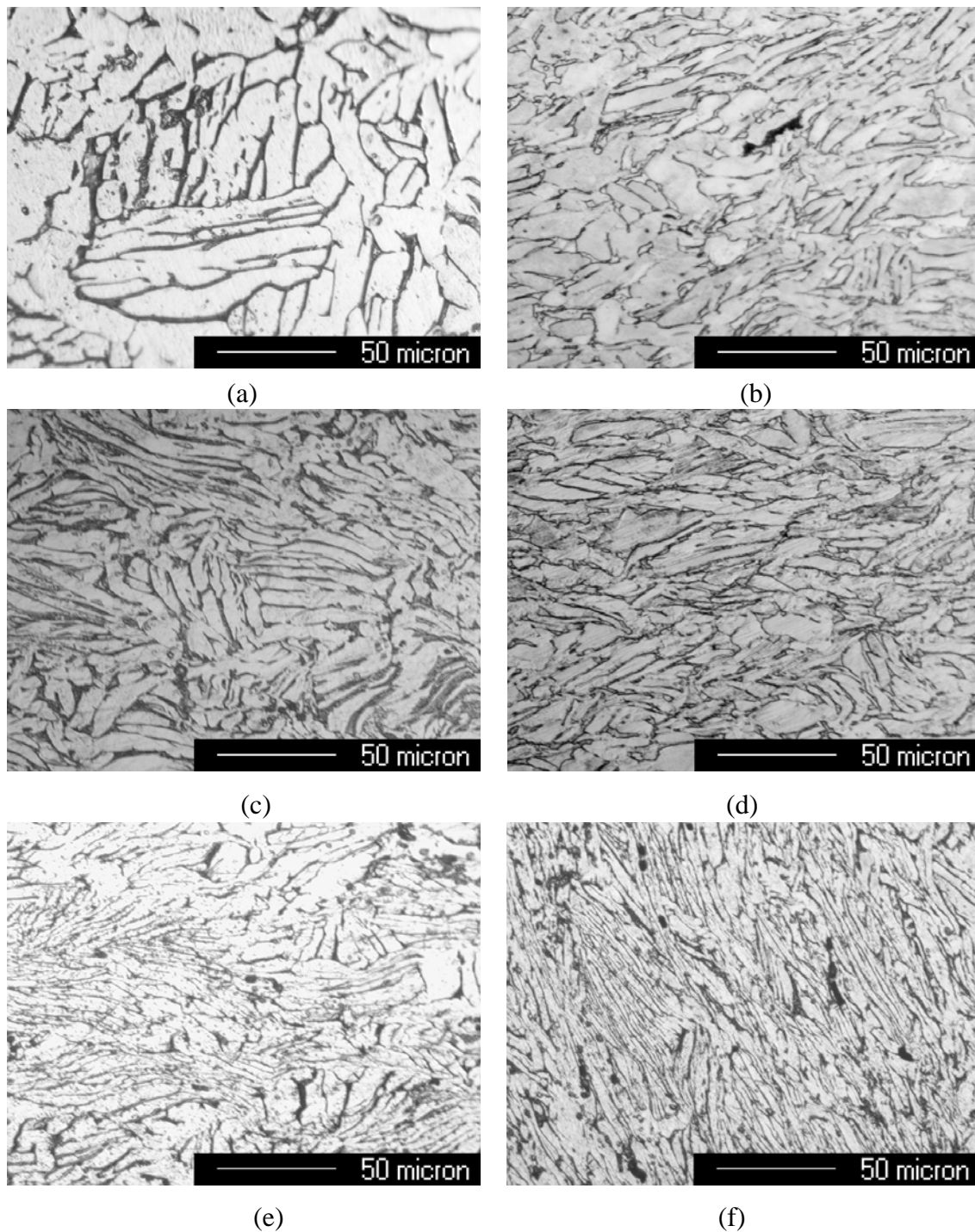
Fig. 3.1.1. Optical micrographs of (a) as-received material and samples extruded at (b) 550°C, one pass, (c) 700°C, one pass, (d) 800°C, one pass, (e) 600°C, two passes, Route A, and (f) 800°C, two passes Route A. Images are taken from the transverse plane.

3. Decreasing extrusion temperature and increasing number of passes promotes cavitation (microcracks and pores) along the β and α interface, especially in the samples extruded at 550°C one pass and 600°C two passes.

4. Macroscopic cracking was not observed in any of the extrusions, presumably because of the hydrostatic pressure provided by stainless steel can.

SEM study also reveals similar findings. SEM micrographs are tabulated in Figs. 3.1.3.a through 3.1.3.f. During extrusion, β strips oriented along shear direction deforms and stress concentrations develop at the α/β interface, especially at the triple junctions. Since colony α structure is hard, the stress concentrations may not be relieved unless the softening rate of α plates exceeds the stress accumulation rate, and cracks or pores may nucleate at the interface [112]. The degree of softening decreases with decreasing temperature and with decreasing α plate size, cavitation occurs at low temperatures and at higher number of passes.

Fig. 3.1.2. Single pass Ti-6Al-4V processed non-isothermally in a stainless steel can at 800°C.
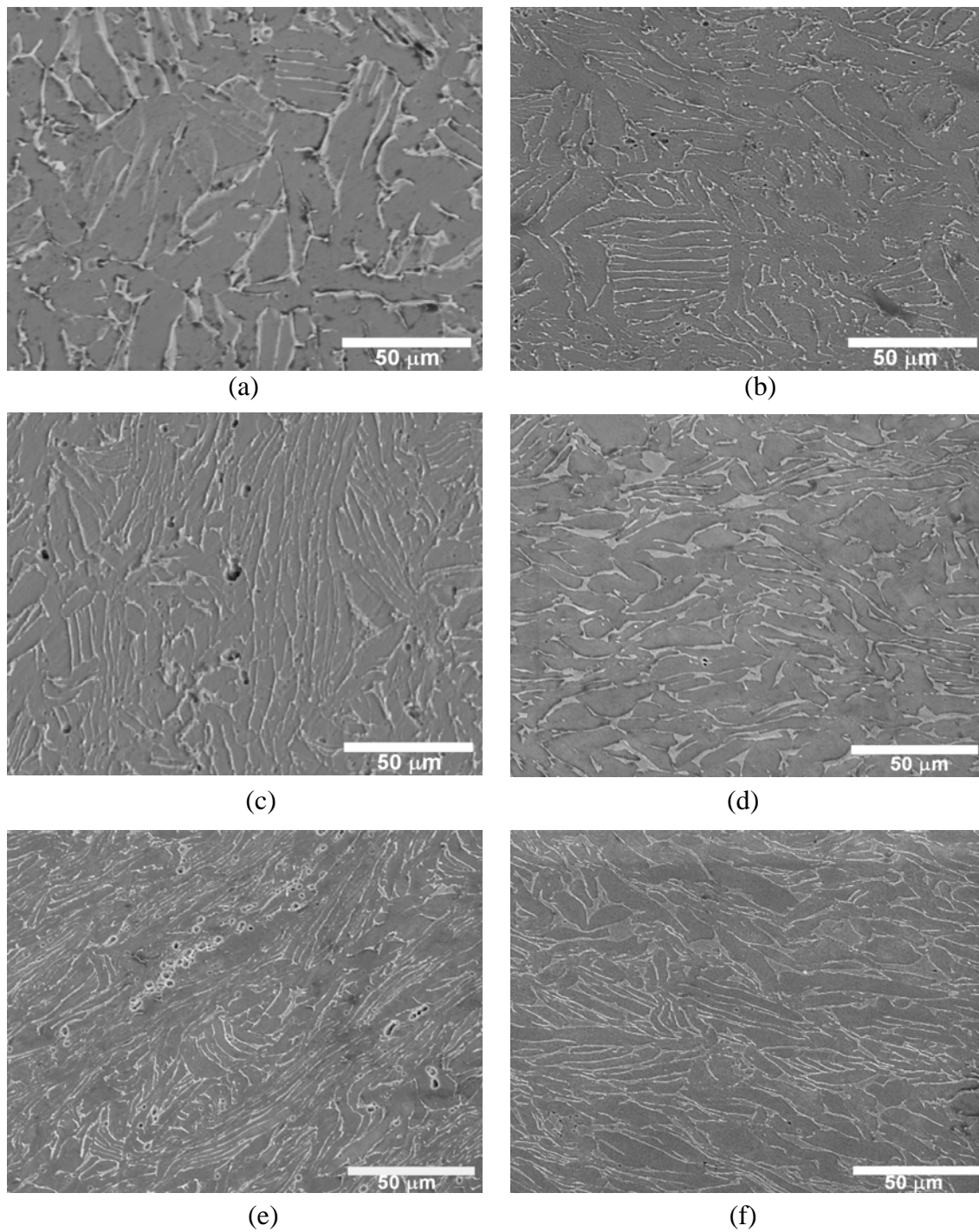
Fig. 3.1.3. SEM micrographs of (a) as-received material and samples extruded at (b) 550°C, one pass, (c) 700°C, one pass, (d) 800°C, one pass, (e) 600°C, two passes, Route A, and (f) 800°C, two passes Route A. Images are taken from the transverse

TEM study was conducted on the flow plane of the processed samples. Each sample was imaged making sure that the α and β phases are distinguished. Fig. 3.1.4 shows the as-received microstructure indicating dislocation free α grains and thin β phase strips located between them.
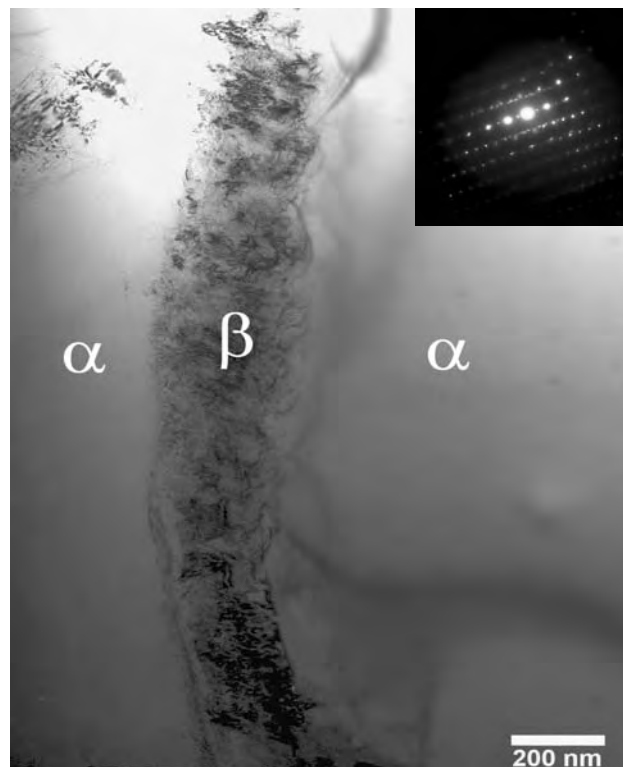
Fig. 3.1.4. TEM micrograph of as received Ti6Al4V demonstrating dislocation free α and β phases. Thin β strips located between coarse lamellar α plates are seen.

Bright field TEM micrographs of Ti64, Figs. 3.1.5 through 3.1.8, indicate that:

1. Refinement of the alpha phase occurs with the formation of recrystallized alpha grains within the plates, the degree of refinement increasing with increasing strain. This can be observed by comparing Figs. 3.1.5.a, 3.1.6.a and 3.1.7.a.

2. Beta phase refinement occurs by fragmentation. A decrease in both the thickness and length of the beta phase was observed after the first pass, successive passes leading to only lengthwise refinement (Figs. 3.1.5.b, 3.1.6.b, 3.1.7.b and 3.1.8.b.).

3. A combination of recrystallized grains and heavily deformed areas are produced by ECAE of Ti64 with the fraction of recrystallized grains increasing with increasing strain. Additionally subsequent passes result in the deformation of recrystallized grains as indicated by the arrow in Fig. 3.1.8.a.
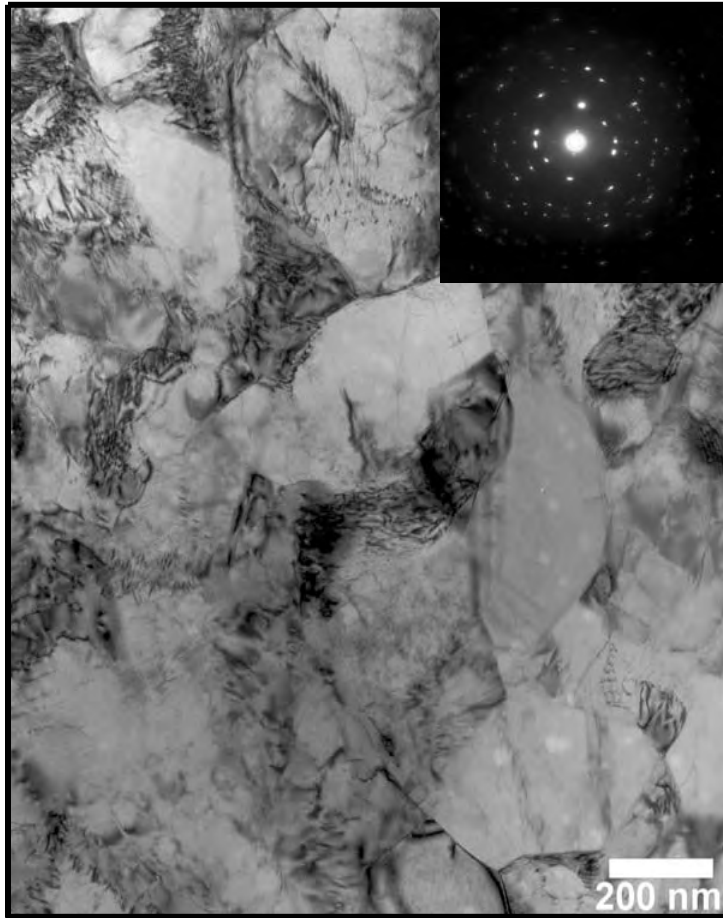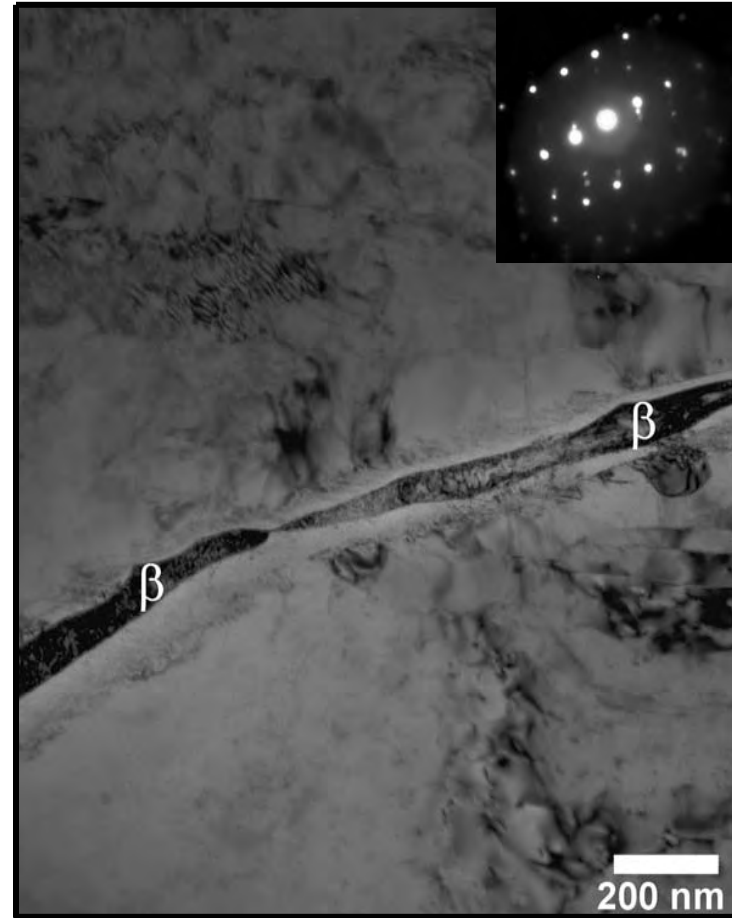
Fig. 3.1.5. TEM micrographs of the sample extruded at 800°C, one pass, (a) high angle boundary subgrain formation with high dislocation density, (b) refined β phase in detail.
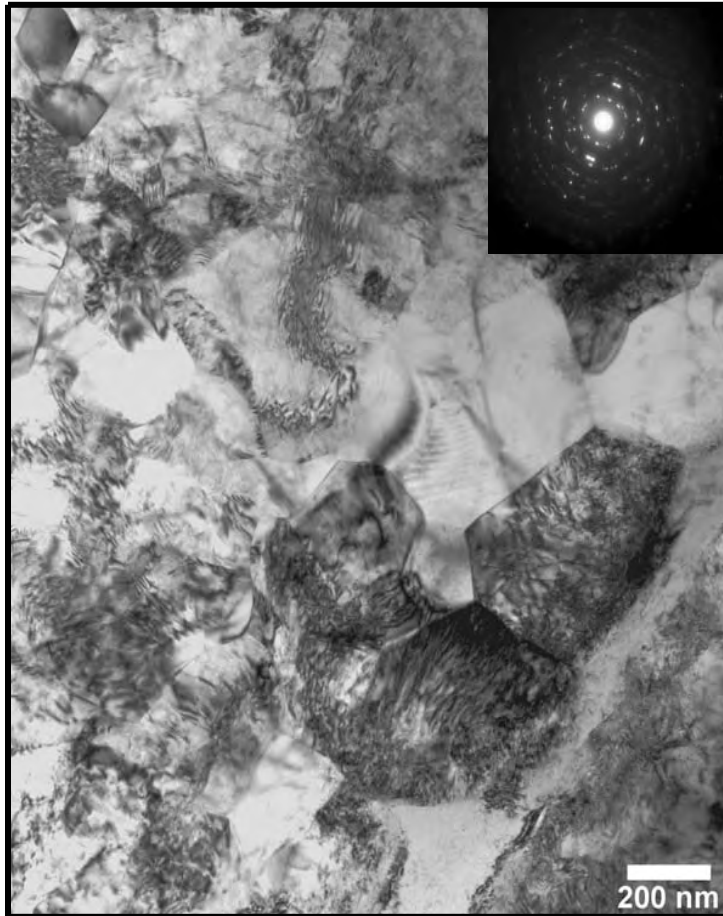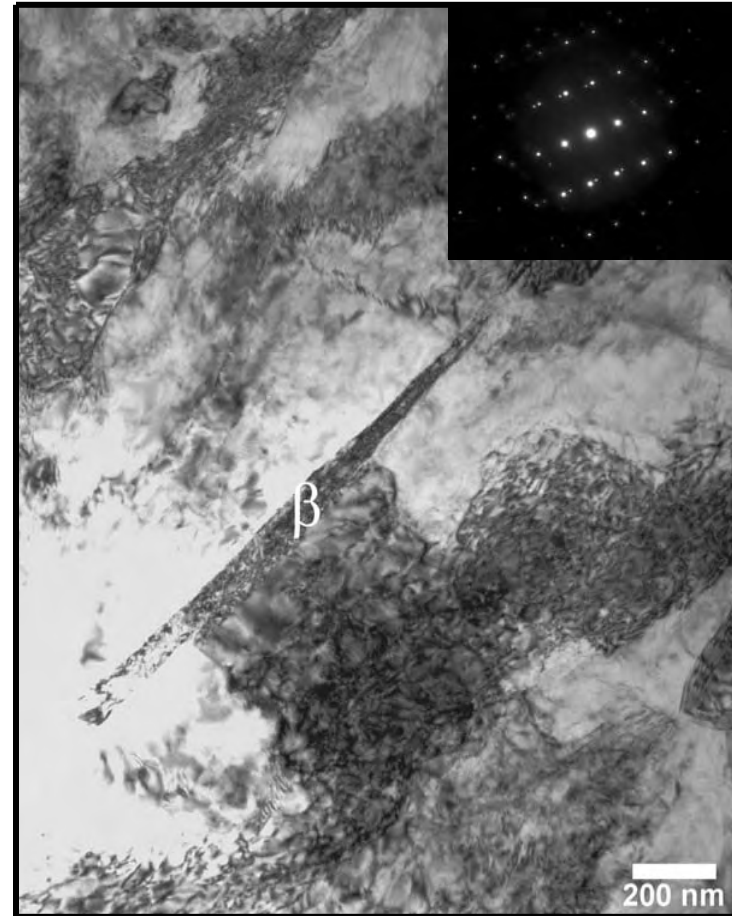
(a) (b)

Fig. 3.1.6. TEM micrographs of the sample extruded at 700°C, one pass, (a) elongated grains when compared to 1A 800°C case, (b) indication of β phase refinement.
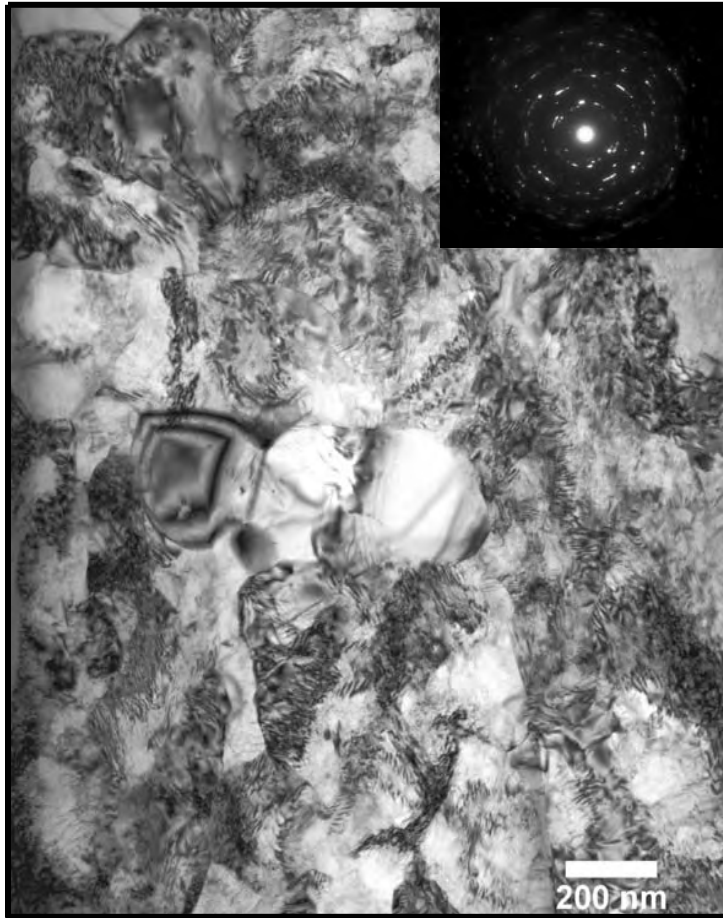
(a)
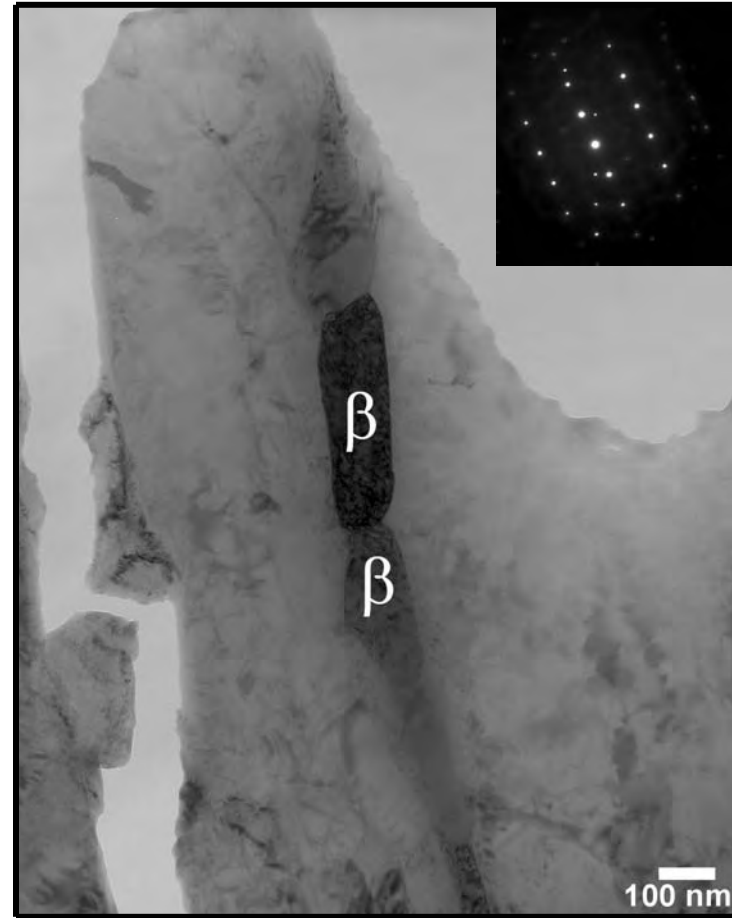
(b)

Fig. 3.1.7. TEM micrographs of the sample extruded at 600°C, two passes, Route A, (a) high dislocation density grains. Both refined and equiaxed α agrains, (b) fragmented β phase along the boundary between α plates.
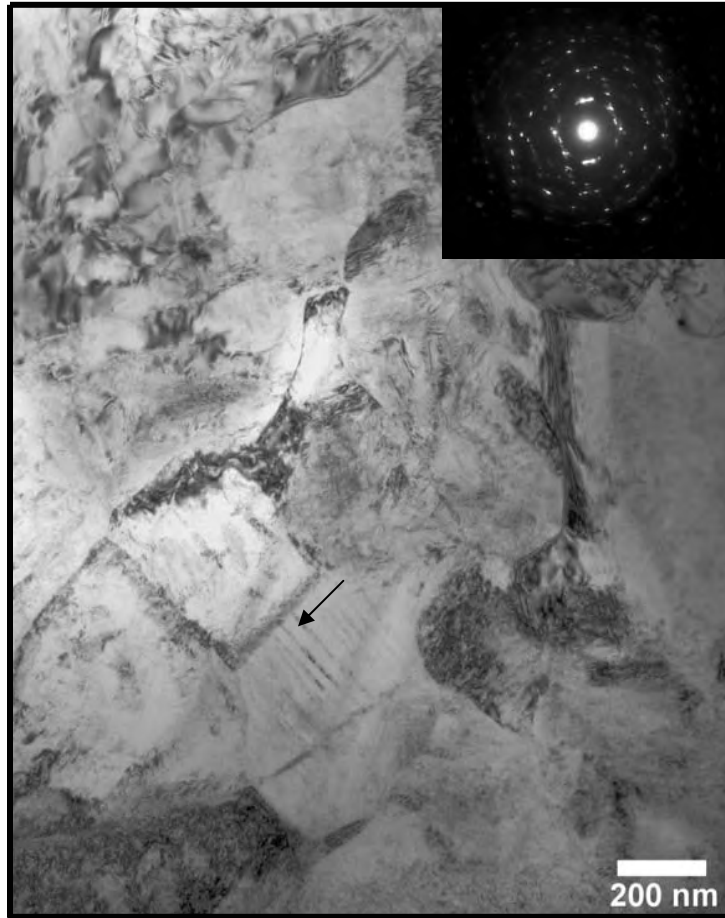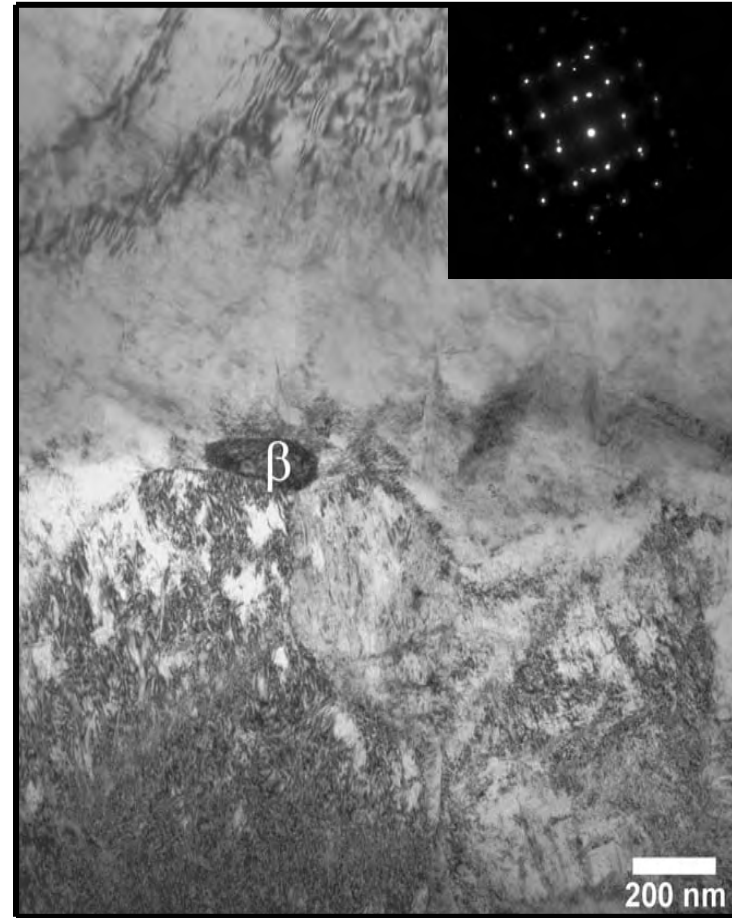
Fig. 3.1.8. TEM micrographs of the sample extruded at 800°C, two passes, Route A (a) twinning in previously recrystallized grains, (b) highly refined β phase.

Table 3.1.1
 Summary of the processing conditions and resulting length scales of Ti-6Al-4V.

Processing Conditions	Average α plate thickness, μm	Average α grain size, nm	Average β phase thickness, nm
As Received	17	-	330
800°C, ECAE 1A	9.7	450	105
800°C, ECAE 2A	7.3	350	115
700°C, ECAE 1A	8.7	305	90
600°C, ECAE 2A	6	260	125

The resulting length scales are obtained by lineal intercept method and tabulated in Table 3.1.1. Fine twins can be seen in the dislocation free grains of the 2A 800 °C processed sample. These grains are formed during the first extrusion pass by dynamic recrystallization. Other than this sample, twinning is not readily observed. It is reported that increasing concentrations of solute atoms in alpha Ti, such as oxygen or aluminum suppresses the occurrence of twinning [113]. Occurrence of the twinning in the second pass may be attributed to the additional strain imposed.

3.2 Mechanical Behavior

Figs. 3.2.1 and 3.2.2 show the stress-strain response of ECAE Ti64. The tensile and compressive yield strengths of Ti64 increase with ECAE deformation: the lower the extrusion temperature, the higher the yield strength. If the yield strengths and the α plate sizes in Table 3.2.1 are compared, it can be seen that there is a direct correlation between the strength values and α plate thickness, and thus the effective slip length. At higher extrusion temperatures, deformation is accompanied by recovery. An interesting observation is that at two different strain rates, both strength and ductility increased after two extrusion passes at 800°C.
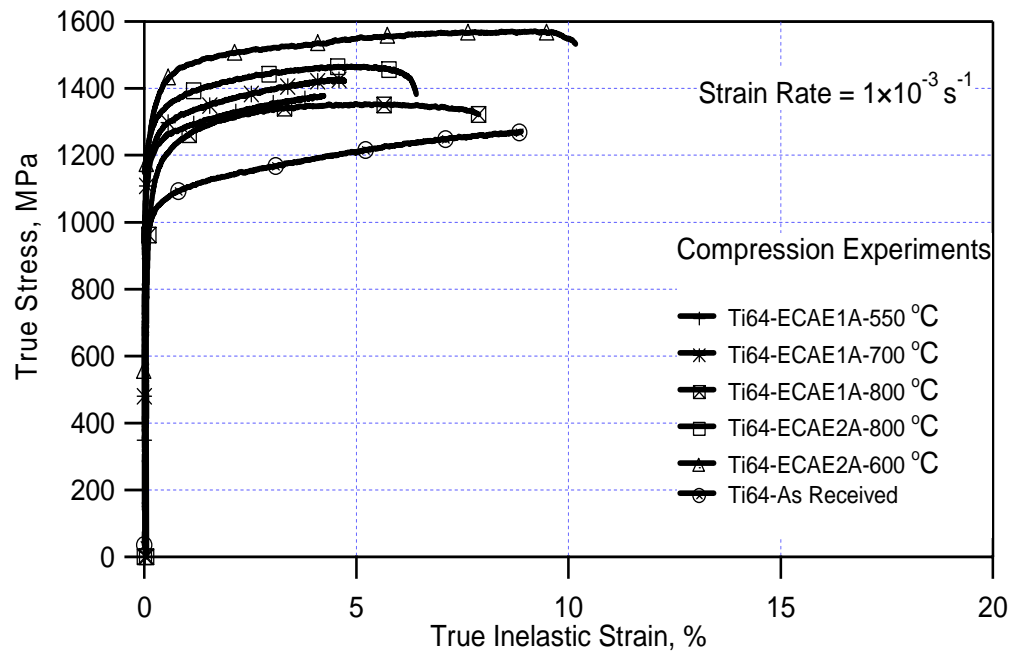
Fig. 3.2.1. Compressive true stress – true inelastic strain response of as-received and ECAE processed Ti-6Al-4V samples at a strain rate of 10^{-3} s^{-1}.

(a)

(b)
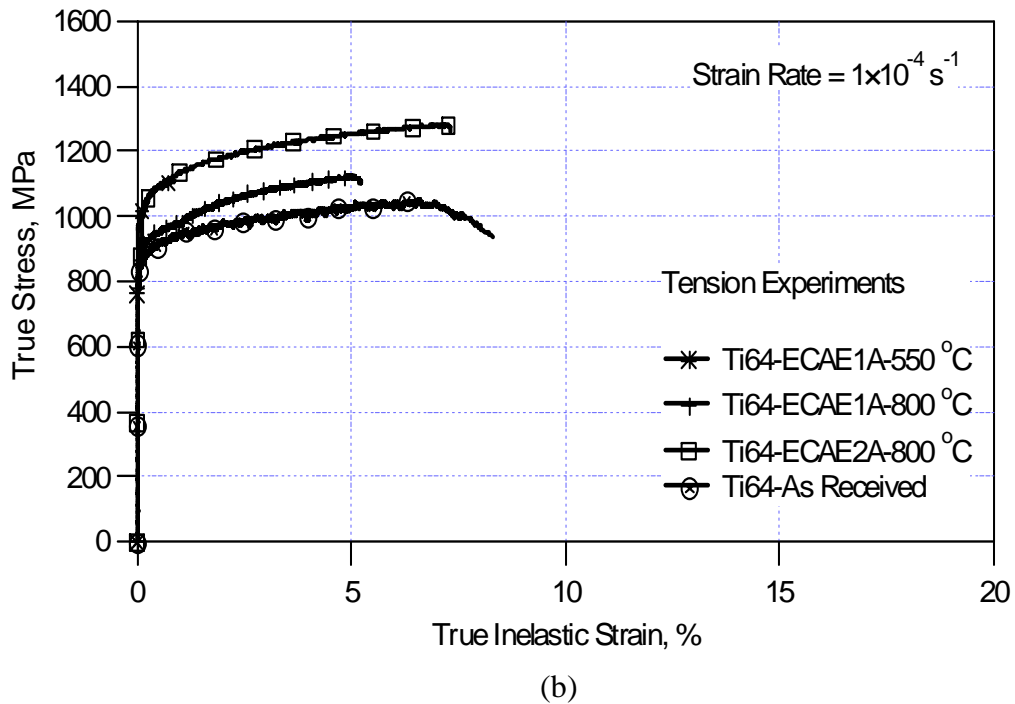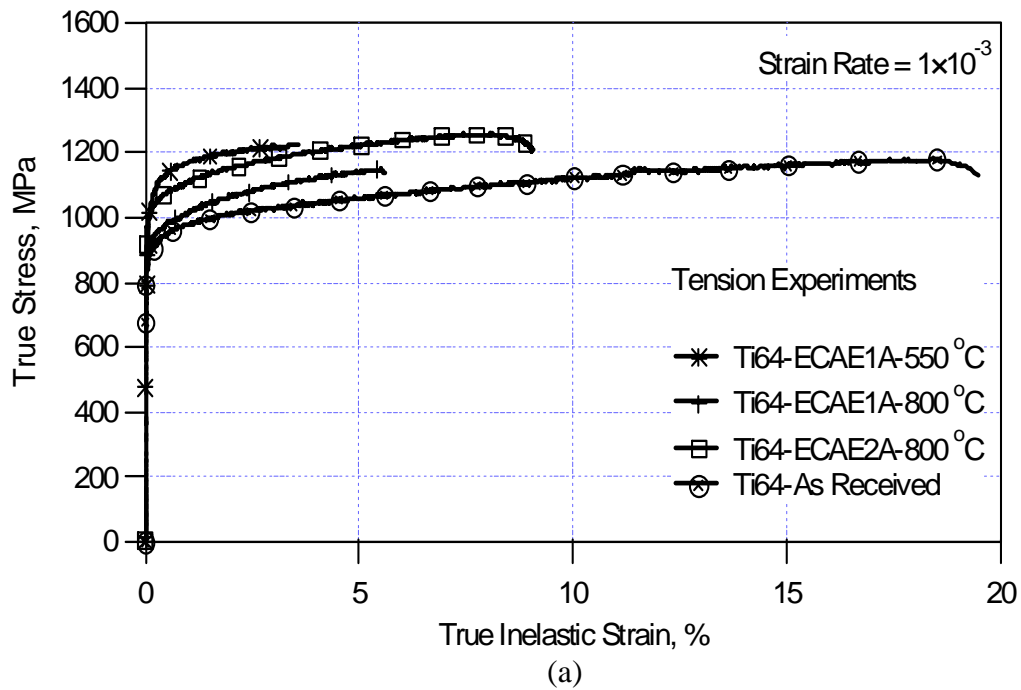
Fig. 3.2.2. Tensile true stress – true inelastic strain response of as-received and ECAE processed Ti-6Al-4V samples at two different strain rates. The strain rates were (a) 10^{-3} s^{-1} and (b) 10^{-4} s^{-1}.

Table 3.2.1

Summary of the results of the mechanical experiments conducted on Ti-6Al-4V at room temperature. σ_y: yield stress; ε_f: tensile fracture strain; $d\sigma/d\varepsilon$: strain hardening coefficient, UTS: ultimate tensile strength.

Processing Conditions	Average α plate thickness, μm	Tension $\dot{\varepsilon}=10^{-3}$				Tension $\dot{\varepsilon}=10^{-4}$				Compression $\dot{\varepsilon}=10^{-3}$		
		σ_y, MPa	UTS, MPa	ε_f, %	$d\sigma/d\varepsilon$, MPa	σ_y, MPa	UTS, MPa	ε_f, %	$d\sigma/d\varepsilon$, MPa	σ_y, MPa	UTS, MPa	$d\sigma/d\varepsilon$, MPa
As Received	17	911	1182	19.5	1408	878	1051	8.3	1797	1021	1271	2417
550°C, ECAE 1A	6.8	1076	1225	3.6	1892	1048	1111	0.9	2432	1200	1378	3576
800°C, ECAE 1A	9.7	941	1149	5.6	2953	920	1127	5.2	3207	1088	1420	2539
800°C, ECAE 2A	7.3	1040	1257	9.1	3078	1042	1284	7.3	2852	1285	1355	3241
700°C, ECAE 1A	8.7	-	-	-	-	-	-	-	-	1220	1466	3613
600°C, ECAE 2A	6	-	-	-	-	-	-	-	-	1318	1572	2417

At higher extrusion temperatures, deformation is accompanied by recovery. An interesting observation is that, both strength and ductility increased after two extrusion passes at 800°C. This may be due to the formation of fine recrystallized grains with low dislocation density. The lower fracture strain in the 550°C sample was attributed to the formation of cavitation at the α/β interface formed during extrusion. The tensile strain hardening coefficients also increased after extrusion deformation as seen in Table 3.2.1. Furthermore, there is a distinct difference between strain hardening coefficients of the 800°C extruded samples as compared to the as-received and 550°C extruded samples. Relatively low strain hardening following extrusion at 550°C was ascribed to microcracks formed during the extrusion process. In turn the higher strain hardening of the 800°C extruded samples when compared to the as-received material can be related to increasing grain boundary area and multiple glide within the finer recrystallized grains formed on extrusion at 800°C.

Compressive strengths also increased after ECAE. Moreover, they are higher than tensile strength values. Except for the 550°C extruded samples, an increase in compressive strength with the decrease in average α plate thickness was observed. The anomaly in the 550°C samples may again be ascribed to cavitation. The strain hardening coefficients in compression were also typically higher than those observed during tension. This difference in strain hardening behavior can be explained by considering the differing orientations of the compression and tensile samples with respect to the extrusion direction. Indeed the tension/compression asymmetry in the as-received material suggests that the initial texture was not random. DeLo et al. [114] demonstrated

that the basal poles of the α phase after one or two ECAE passes using route A was oriented in the longitudinal direction of the deformed billets (compression axis direction in the present study) perpendicular to both the extrusion direction (tension axis direction in the present study) and entrance direction. Fig. 3.2.3 exhibits the specimen orientations. At ambient temperature, this difference in texture will lead to activation of different slip systems as summarized in Table 3.2.2 and Fig. 3.2.4.

Table 3.2.2
Schmid factors for possible deformation mechanisms.

Loading Axis (l)	Slip Plane (n)	Slip Direction (s)	Schmid Factor (f)
$[10\bar{1}0]$	$(\bar{1}100)$	$[11\bar{2}0]$	$\sqrt{3}/4$
$[10\bar{1}0]$	$(0\bar{1}11)$	$[\bar{1}\bar{2}13]$	0
$[10\bar{1}0]$	(0001)	$[11\bar{2}0]$	0
$[000\bar{1}]$	$(\bar{1}100)$	$[11\bar{2}0]$	0
$[000\bar{1}]$	$(0\bar{1}11)$	$[\bar{1}\bar{2}13]$	$1/\sqrt{5}$
$[000\bar{1}]$	(0001)	$[11\bar{2}0]$	0

Lecomte et al. [115] investigated the deformation behavior of rolled Ti64 with an initial strong transverse texture (majority of the alpha phase aligned with the c axis perpendicular to the rolling direction). They demonstrated that higher tensile yield stresses are obtained for samples oriented in the transverse direction than the ones in the rolling direction. Moreover, along basal poles, compressive yield stresses are higher than tensile yield stresses because the high Critical Resolved Shear Stress (CRSS) of asymmetric <c+a> glide (main deformation mode along this texture) differs upon

reversal of resolved shear stress [115, 116]. These findings explain the observed tension/compression asymmetry in the present study.
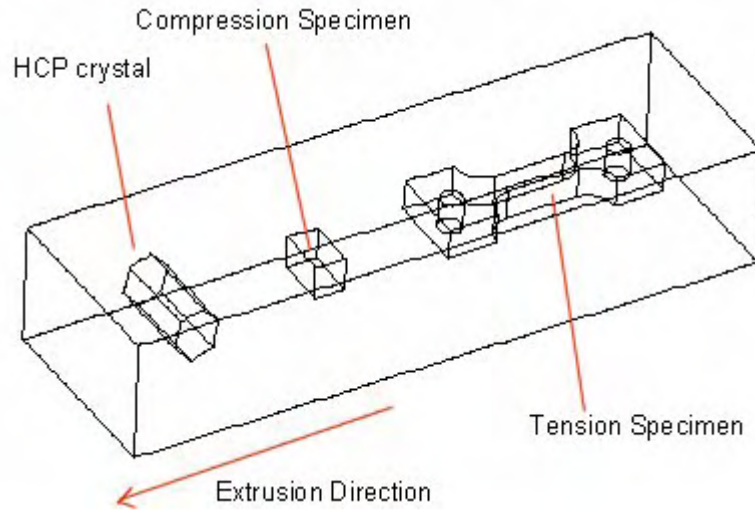
Fig. 3.2.3. Orientation of the tension and compression specimens prepared with respect to the extruded billet and the hcp crystal orientation after ECAE.
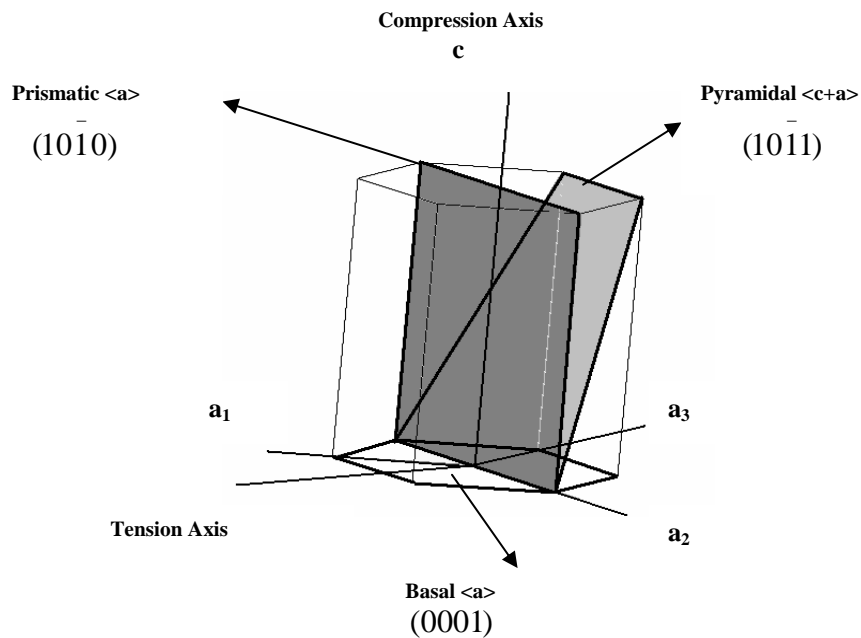
Fig. 3.2.4. Slip planes for basal <a>, prismatic <a> and pyramidal <c+a> glides.

Finally, Fig. 3.2.5 shows that the hardness measurements were inversely proportional with the alpha plate size: the 600°C two pass extruded samples having the highest hardness values and 800°C one pass extruded samples having the lowest.
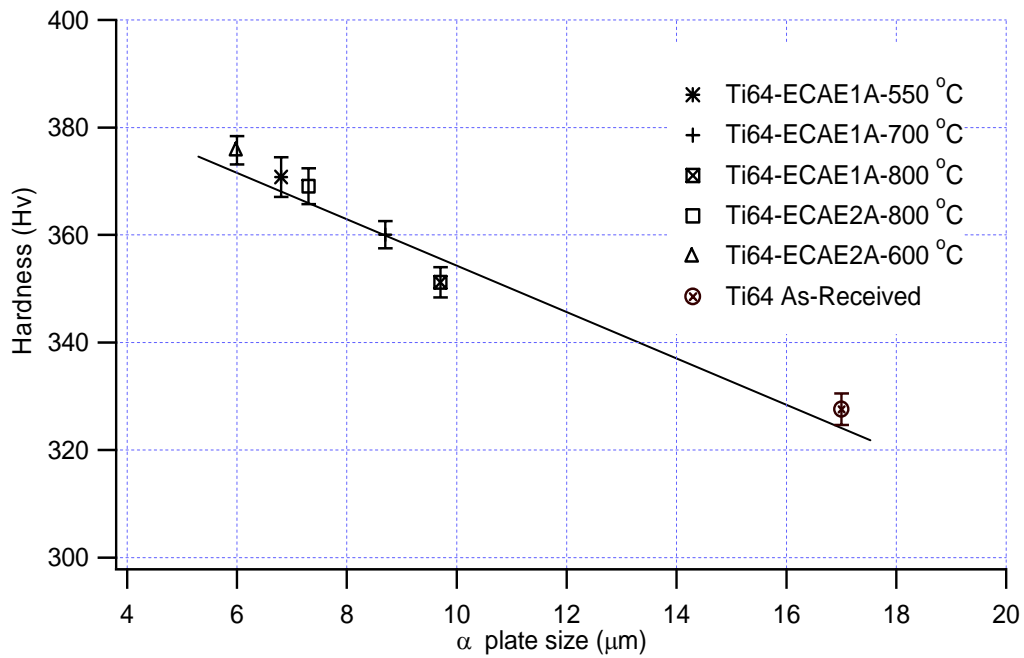
Fig. 3.2.5. Hardness of ECAE processed Ti-6Al-4V as a function of alpha plate size.

CHAPTER IV

RESULTS & DISCUSSIONS ON Ti-6Al-4V+10%TiC

This section will demonstrate microstructural examinations and mechanical behavior results pertaining to Ti-6Al-4V+10%TiC metal matrix composite.

4.1 Microstructural Evolution

The as received material has a coarse colony lamella α microstructure with an average colony size of 60 μm and a lamellae α plate size of 15 μm. As in the case of Ti64, Ti64/TiC extrusions also lead to decrease in α plate size, with a small refinement in TiC particle size. These observations can be seen in Figs. 4.1.1.a through 4.1.1.f. SEM imaging was conducted especially to examine the TiC particle distribution after ECAE processing. It has been explained that uniform distribution of reinforcements in metal matrix composites lead to significant strengthening compared to random distribution. However, no significant change in particle distribution was observed. Further extrusion passes may lead to significant size refinement and control over particle distribution. When compared to the Ti64 extrusions, the degree of refinement in the α plate size is lower possibly due to the effect of particle reinforcements. The microstructural refinement is tabulated in the second table on page 59.
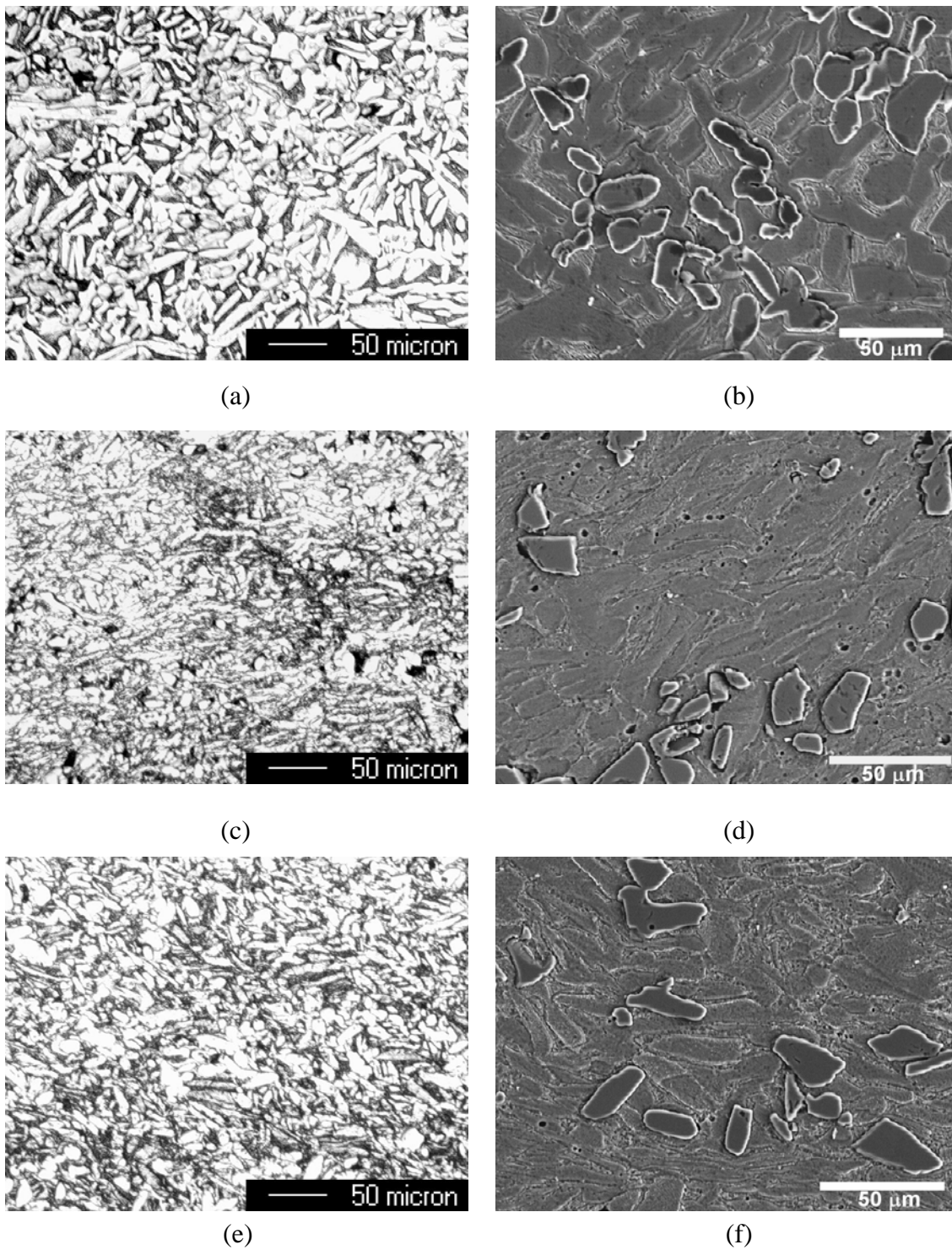
Fig. 4.1.1. Optical Microscopy and SEM micrographs of (a, b) as-received material and samples extruded at (c, d) 700°C, one pass, (e , f) 800°C, one pass, respectively.

4.2 Mechanical Behavior

Ti64/TiC samples exhibited higher tensile and compressive strengths with lower ductility than Ti64 samples. In spite of having a larger α plate size, 800°C sample have higher strengths than the 700°C sample, which may be attributed to the possible different distribution of TiC particles. Tension compression asymmetry in yield strengths present as expected and explained in Ti64 section (Figs. 4.2.1, 4.2.2). Higher tensile and compressive yield strengths may be obtained with further ECAE passes resulting in further α plate size and TiC particle size reduction. As discussed earlier it is reported that tailoring of the reinforcement is essential in terms of improved mechanical properties [24, 83]. Summary of the mechanical experiments can be found in Table 4.2.1. Results from hardness test are also tabulated in Table 4.2.2.
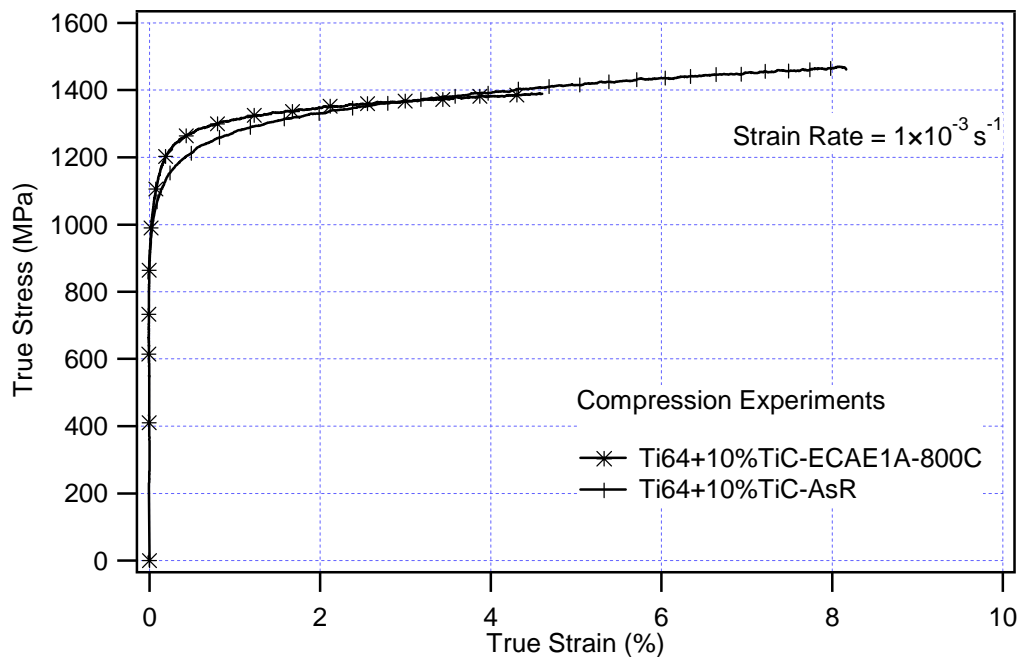
Fig. 4.2.1 Compressive true stress – true inelastic strain response of as-received and ECAE processed Ti-6Al-4V samples at a strain rate of 10^{-3} s^{-1}.
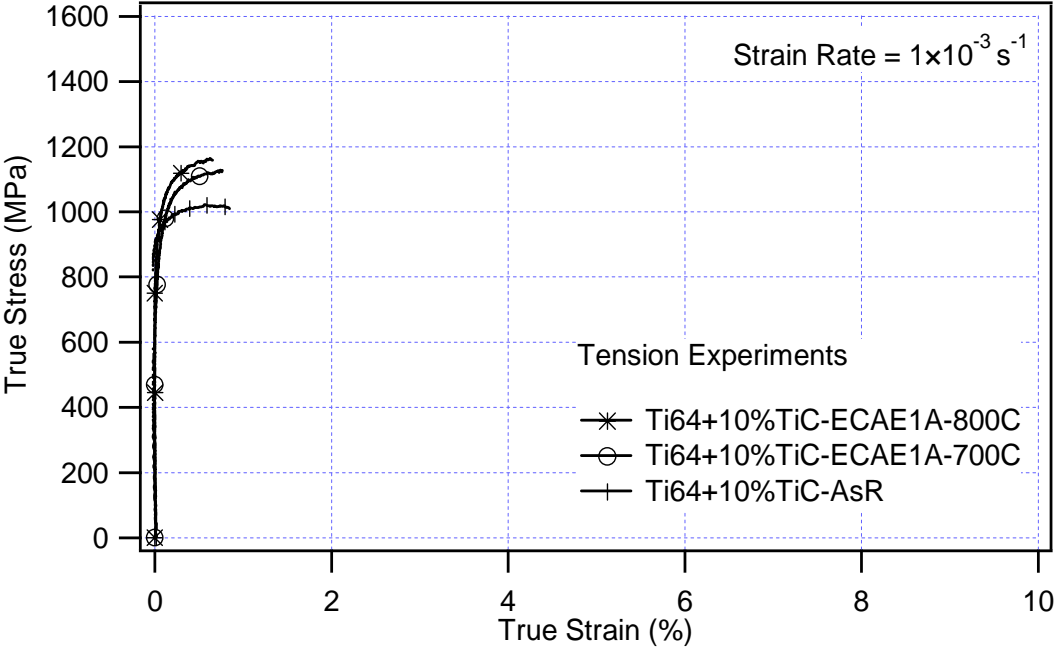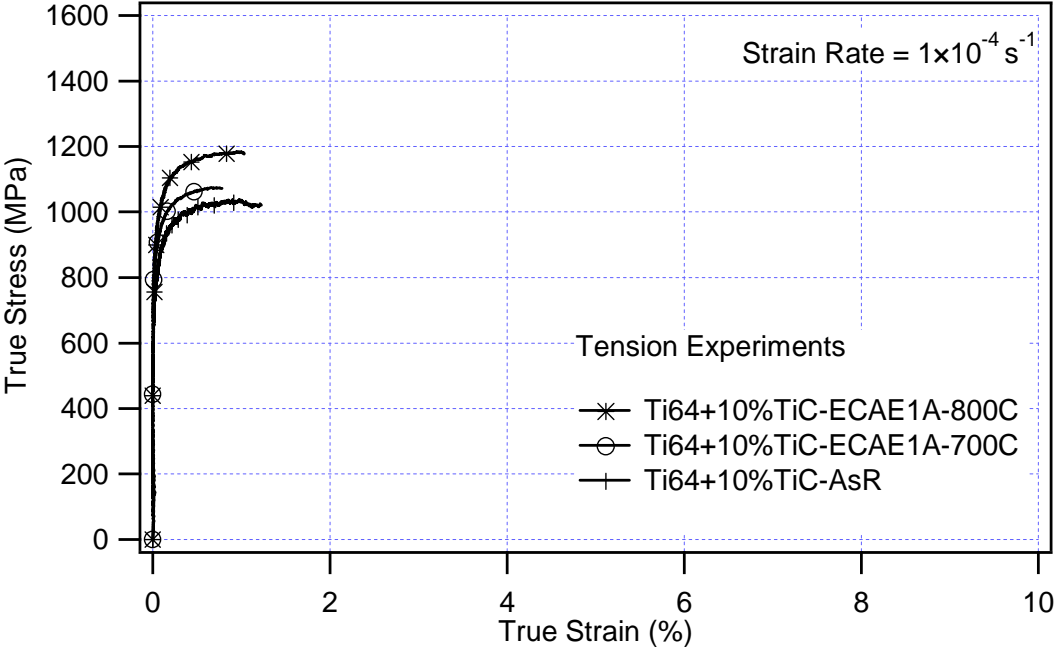
Fig. 4.2.2. Tensile true stress – true inelastic strain response of as-received and ECAE processed Ti-6Al-4V+10%TiC samples at two different strain rates. The strain rates were (a) 10^{-3} s^{-1} and (b) 10^{-4} s^{-1}.

Table 4.2.1
Summary of the results of the mechanical experiments conducted on Ti-6Al-4V+10%TiC at room temperature. σ_y: yield stress; ε_f: tensile fracture strain; $d\sigma/d\varepsilon$: strain hardening coefficient, UTS: ultimate tensile strength.

| | Tension | | | | | | | | Compression | |
| | $\dot{\varepsilon} = 10^{-3}$ | | | | $\dot{\varepsilon} = 10^{-4}$ | | | | $\dot{\varepsilon} = 10^{-3}$ | |
Processing Conditions	σ_y, MPa	UTS, MPa	ε_f, %	$d\sigma/d\varepsilon$, MPa	σ_y, MPa	UTS, MPa	ε_f, %	$d\sigma/d\varepsilon$, MPa	σ_y, MPa	$d\sigma/d\varepsilon$, MPa
As Received	990	1182	19.5	1408	955	1051	8.3	1797	1139	2417
700°C, ECAE 1A	1042	1225	3.6	1892	1018	1111	0.9	2432	1200	3576
800°C, ECAE 1A	1093	1149	5.6	2953	1106	1127	5.2	3207	1208	2539

Table 4.2.2
Refinement in α plate thickness and corresponding hardness values.

Processing Conditions	As Received	700°C, ECAE 1A	800°C, ECAE 1A
Average α plate thickness, μm	15	8.4	10.3
Hardness (Hv)	367	375	394

CHAPTER V

RESULTS & DISCUSSIONS ON AISI 316L

This section will demonstrate microstructural examinations and mechanical behavior results pertaining to AISI 316L stainless steel.

5.1 Microstructural Evolution

Successful extrusion of billets held at various temperatures without considerable localization, Fig. 5.1.1 exhibits one of them. Optical images are taken from the transverse planes of the extruded billets. Fig. 5.1.2 shows the microstructure of the as-received material. The annealing twins are evident. The average grain size is about 40 µm. Fig. 5.1.3 demonstrates the optical images from the flow planes of the extruded billets. Elongated grains in the direction of extrusion are a common feature of all micrographs taken. For all the extrusions, refinement in grain size is apparent. The 2B 600 °C billet has very fine structure possibly because of the large shear deformation and additional refinement during the second pass.
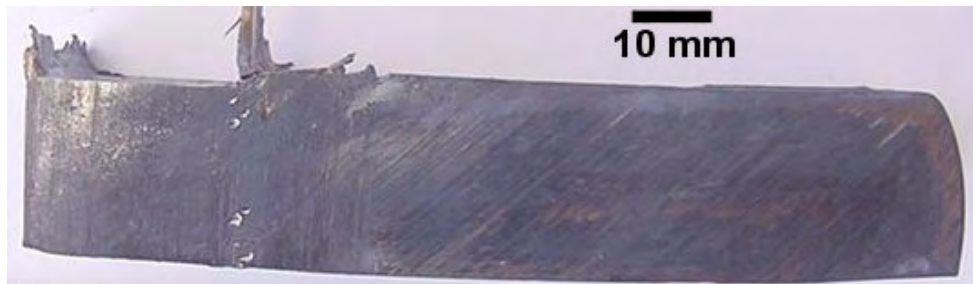
Fig. 5.1.1. A 316L stainless steel extruded billet at 550 °C. Extrusion is successful without localized deformation.

This apparent grain refinement causes hardening in the processed materials and apparently affects the mechanical properties. The comparison of the flow plane images demonstrates that the deformed grains have penny shapes and the minor axis length is the smallest in the 2B 600 °C sample while 700 °C and 800 °C samples have the largest minor axis length. The larger grains in 700 °C and 800 °C samples (Figs. 5.1.3.c and d) are attributed to the possible grain growth mechanisms taking place at higher temperatures. Although, it is hard to quantify the resulting grain size due to the highly deformed structure, it is likely that subgrains exist and should be taken as the important parameter in determining the degree of refinement by ECAE.
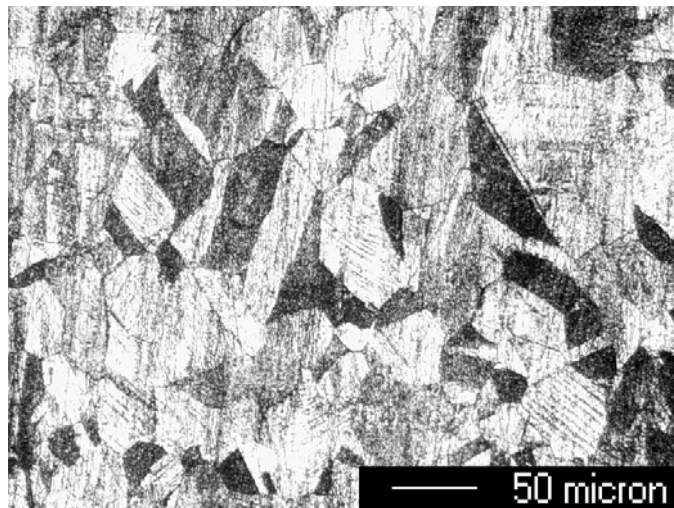
Fig. 5.1.2. Optical micrograph of SS 316L as-received material

Extrusion Direction
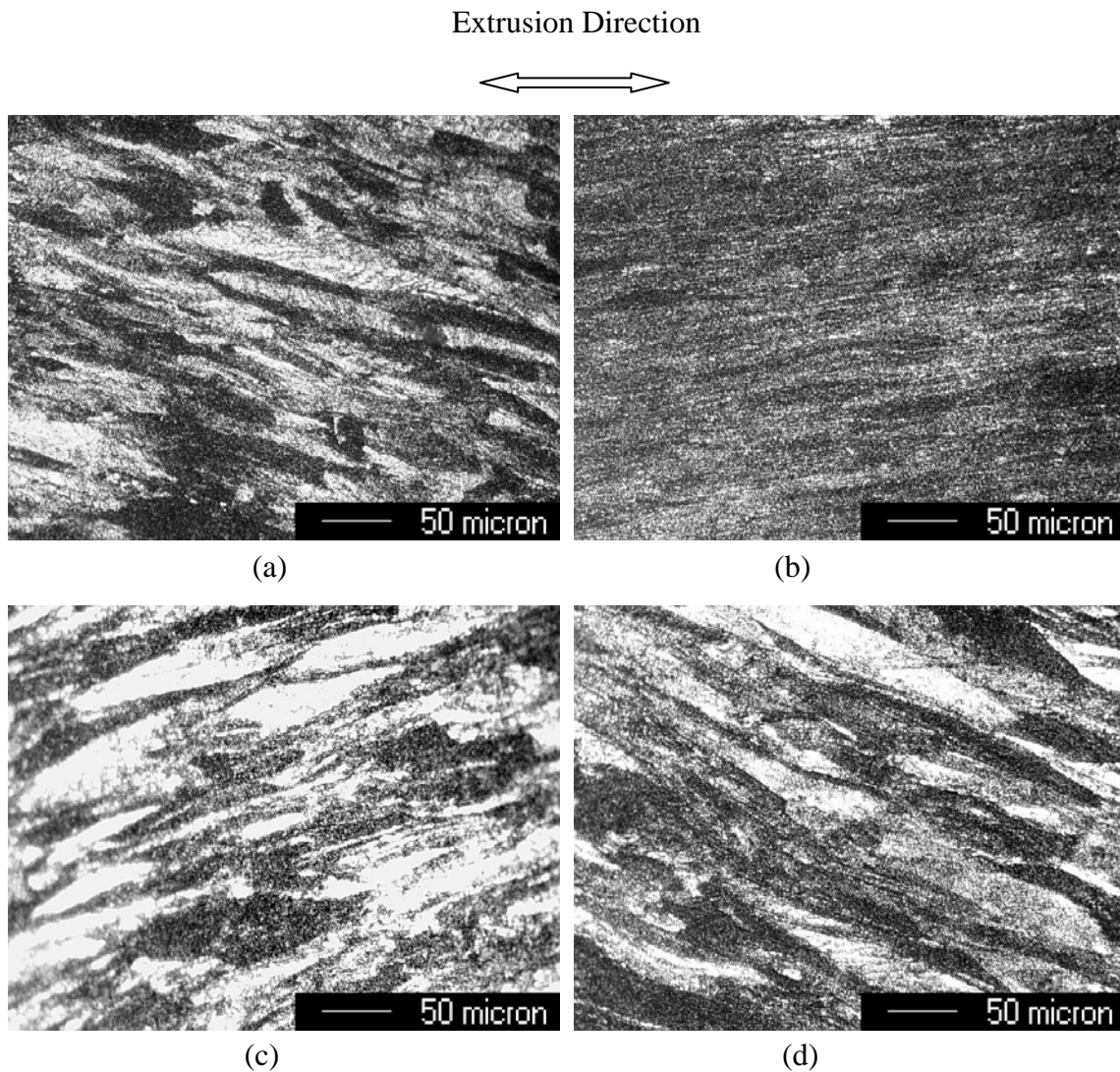
Fig. 5.1.3. Optical micrographs of (a) 450°C, one pass, (b) 600°C, two passes, Route B, (c) 700°C, one pass, (d) 800°C, one pass. Images are taken from the flow plane.

TEM studies showed that the as received material has a microstructure with dislocation free areas and few annealing twins that are common for the material (Fig. 5.1.4). TEM images of the ECAE processed samples are demonstrated in Figs. 5.1.5

through 5.1.10. The 450 ^{o}C extruded sample has a fine straight twin structure with a high dislocation density background on the flow plane. It is important to note the different twin systems terminating at the grain boundary. The longitudinal plane consists of dislocation cells and equiaxed subgrains with moderate dislocation density. The transverse plane is similar to the flow plane structure with the difference of having thicker twins with a wider spacing between boundaries. Also it may be seen that the intersection of twin systems with two different variants is more pronounced in this orientation. It is well known that multiple twinning is a characteristic structure of austenitic steel at high deformation degrees [117, 118]. The choice of strain accommodation by slip or secondary twinning may depend on the ratio of critical resolved shear stresses (CRSS) for slip and twinning. Moreover, a certain stress level is required by the pile-up of dislocations at twin-matrix interface for a new twin to shear through an existing twin [119]. The other important issue taking place is the initiation of subgrain formation at the twin-twin intersection sites.

Studies on the dynamic recovery mechanisms taking place at grain boundaries in ultra fine grained steels has been conducted [120, 121]. Kaibsyhev et al. [122] studied the dynamic recrystallization in relation with twinning. They showed the transformation of deformation twins to random high angle grain boundaries. In our case, extensive twin intersections brings in an ultra fine structure by breaking down grains into smaller domains and forms possible nucleation sites for new grain formation. In Fig. 5.1.5.c, it is seen that dislocation cells are formed in the vicinity of twin-twin intersections.

Fig. 5.1.4. TEM micrograph of SS 316L as-received material demonstrating dislocation free regions with annealing twins.

The 600 $^{\circ}$C sample (Fig. 5.1.6.) has a mixture of fine and coarse twins between elongated lamellar type cell structures on the flow plane. The twins are comparably thicker which may be attributed to the additional strain imposed by the second extrusion pass. This is in contrast to the study reporting increased twin thickness with increased strain for low SFE fcc alloys [117]. The longitudinal plane contains subgrains with high dislocation areas, the spreading in the diffraction pattern reveals the misorientation. However, the structure is not stabilized as compared to its counterpart in 450°C extrusion. The transverse plane contains equiaxed refined subgrains on the order of about 160 nm. These are possibly formed due to simultaneous annihilation and recovery processes occurred during the second extrusion pass.
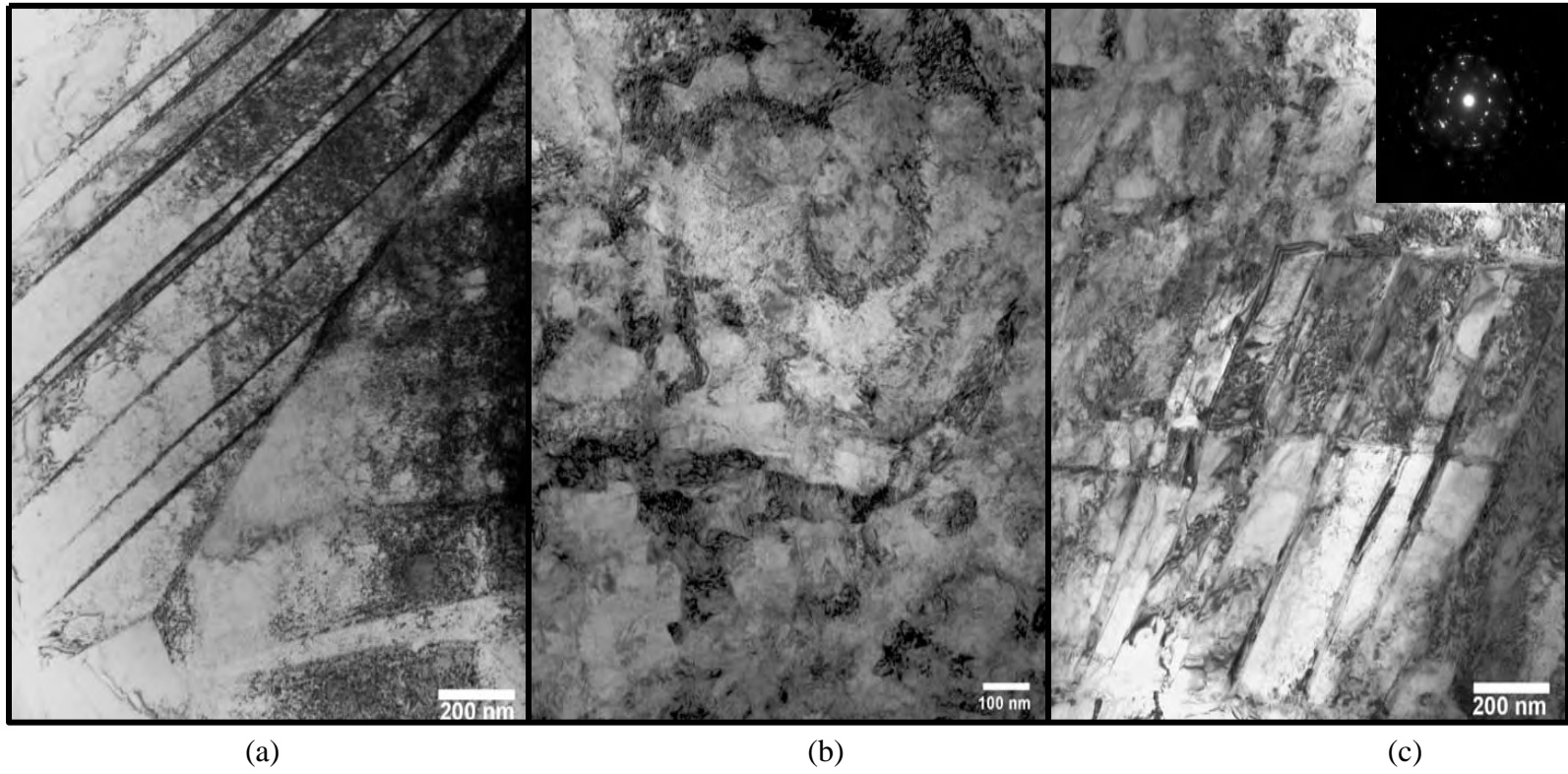
Fig. 5.1.5. TEM micrographs of the sample extruded at 450°C, one pass, (a) flow plane, (b) longitudinal plane, (c) transverse plane.

(a) (b) (c)
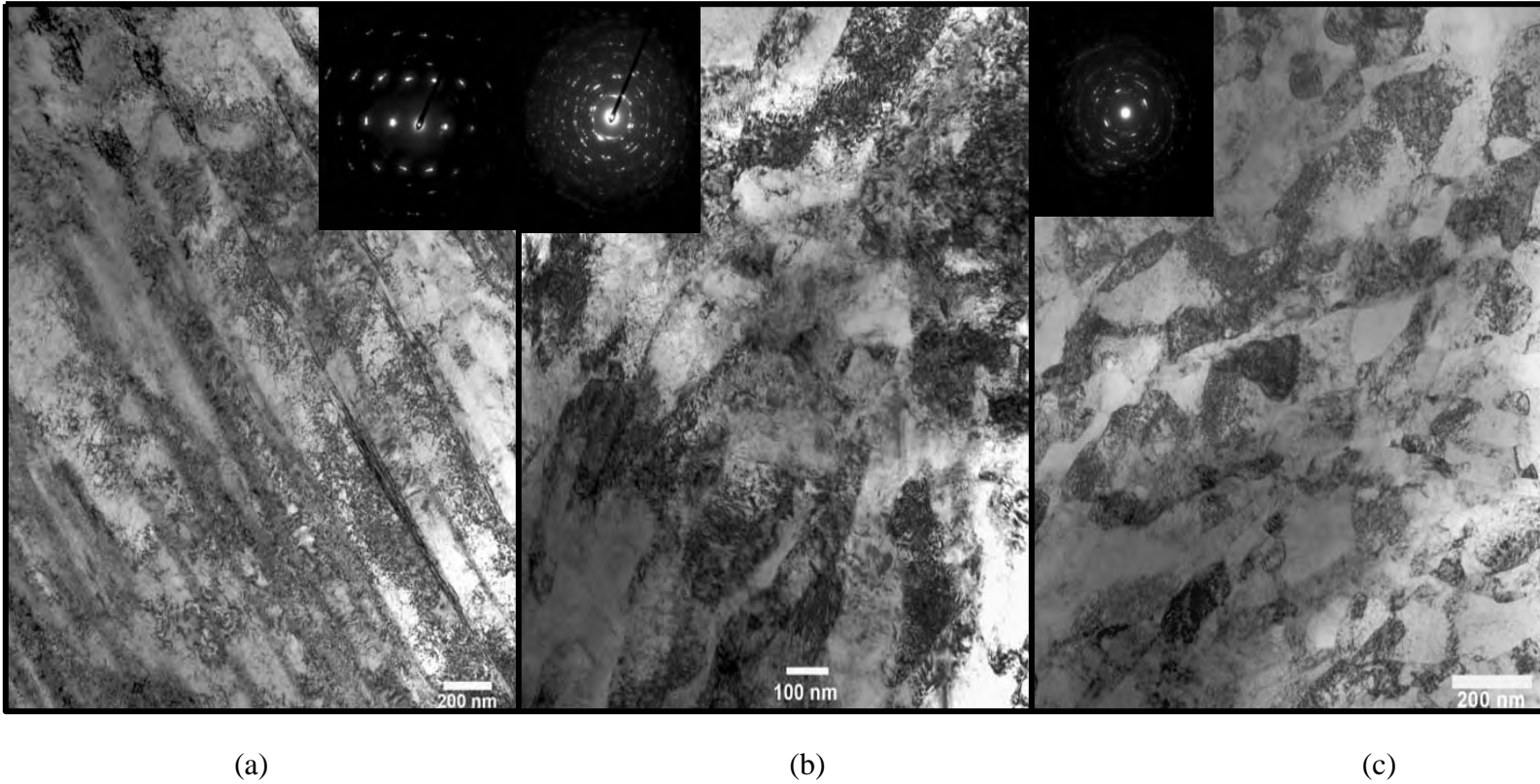
Fig. 5.1.6. TEM micrographs of the sample extruded at 600°C, two passes, Route B, (a) flow plane, (b) longitudinal plane, (c) transverse plane.
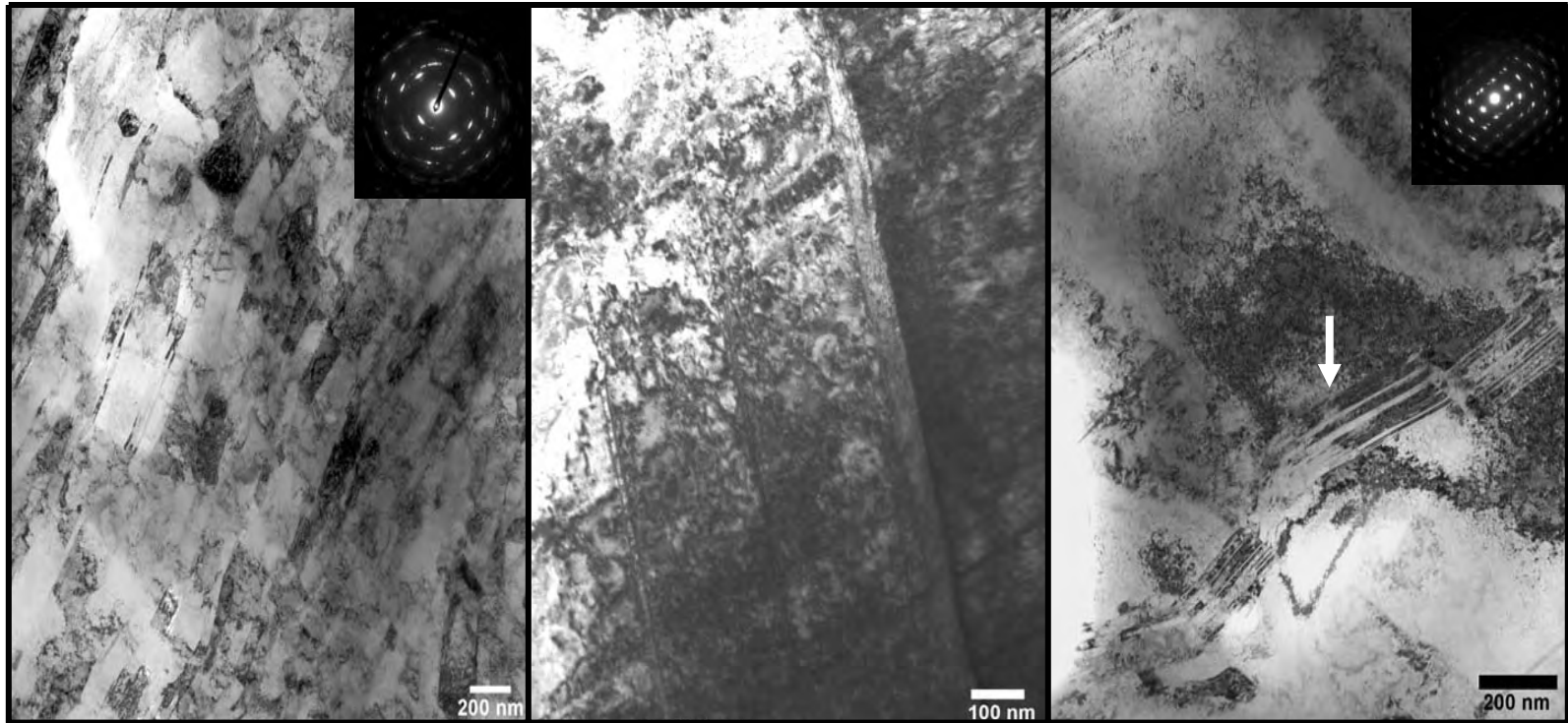
Fig. 5.1.7. TEM micrographs of the sample extruded at 700°C, one pass, (a) flow plane, (b) longitudinal plane, (c) transverse plane.
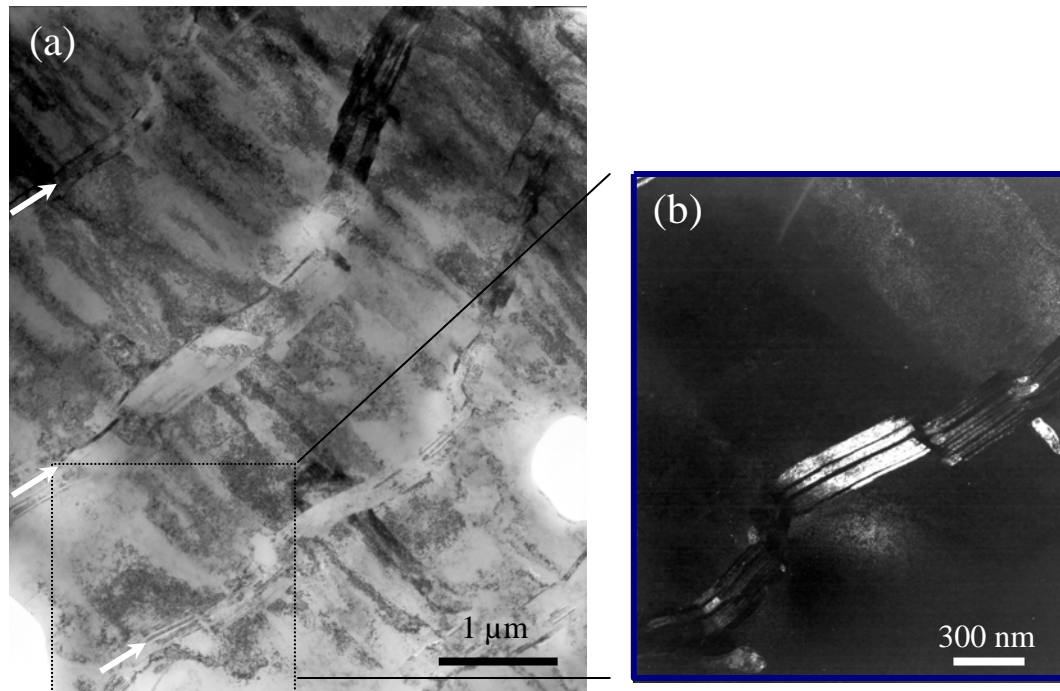
Fig. 5.1.8. (a) Low magnification image of Figure 5.1.7.c demonstrating parallel twinning bands as indicated by arrows, (b) Dark field image of the framed area in (a).
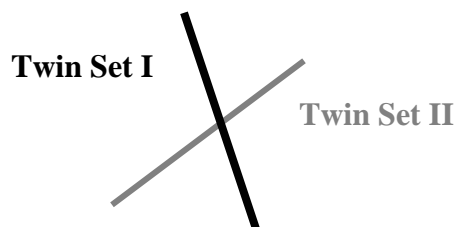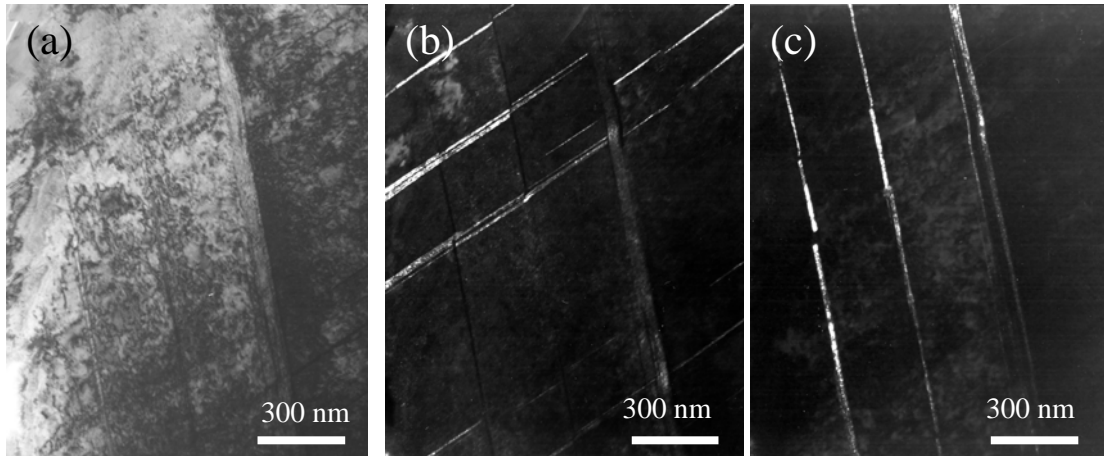
Fig. 5.1.9. (a) Intersection of two sets of twins at 700°C, one pass sample, (b) Dark field image of the first system, (c) Dark field image of the second system.
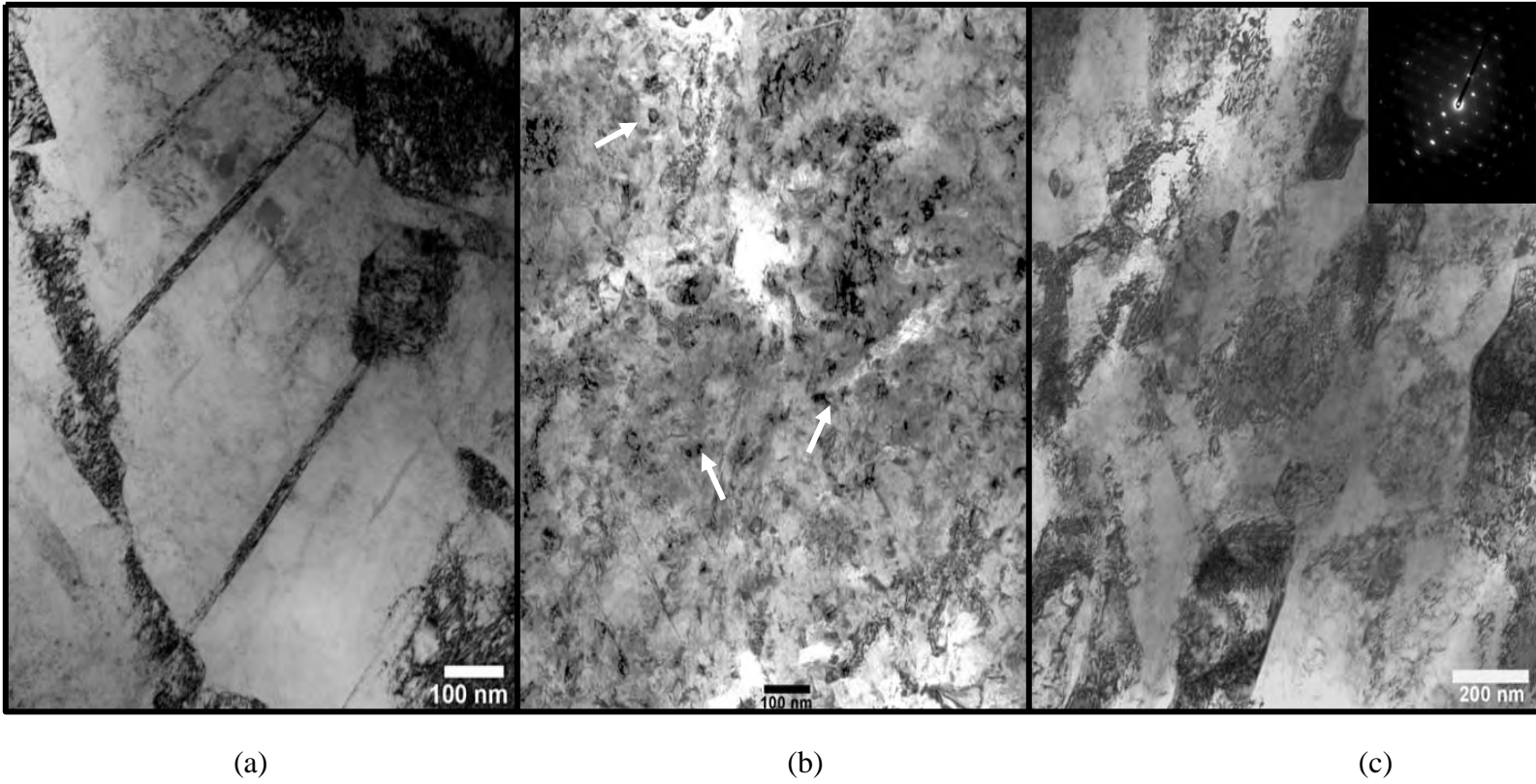
Fig. 5.1.10. TEM micrographs of the sample extruded at 800°C, one pass, (a) flow plane, (b) longitudinal plane, (c) transverse plane.

It is seen that the 700 $^{\circ}$C sample consists of very fine twins dispersed in the matrix with high dislocation density as shown in Fig. 5.1.7. Thin twins with an average thickness of 35 nm formed bundles with approximately equal distances of about 200 – 300 nm. It is previously demonstrated in single crystalline low SFE austenitic steels (316L and Hadfield Manganese steel) [123-125] that thin twins and bundle formation are common features of the deformation of these materials and play an important role in work hardening. Intersection of two twin systems can be observed occasionally (Figs. 5.1.5.c, 5.1.7.b and 5.1.9) leading to a fine twin network. The short twin length and abrupt change in twin direction in Figs. 5.1.7.c and 5.1.8 is because of microshear band formation. The existence of such a fine structure seems abnormal at first glance, since it is reported that twin thickness increases with temperature in austenitic steels [126]. Twins were not evident in all grains as some of the grains experienced elongated subgrain formation with high misorientation boundaries (Fig. 5.1.7.a) as expected in severely deformed materials. The average subgrain size along the minor axes is about 200 nm. In the grains where twins were evident, well-developed subgrain formation was not observed.

The 800 $^{\circ}$C extrusion leads to a structure composed of relatively coarse elongated subgrains and widely spaced twins as seen in Figs. 5.1.10.a and c. The subgrains are larger and more equiaxed than that of the 700 °C sample. There has been no study reporting deformation twins at homologous temperatures as high as 0.6 T_m. Twin formation was orientation dependent in the 800 °C sample as well. Moreover, in some

areas (Fig. 5.1.10.b), dynamically recrystallized nanosized (30-50 nm) grains were observed as indicated by the arrows.

In this microstructural evolution investigation, two observations are particularly significant: twin formation at such high homologous temperatures and orientation dependence of twin formation. The rationale for the former is that the twin formation is due to the high stress levels achieved during severe plastic deformation. In particular, dynamic strain aging, high strain levels and relatively high strain rate ($2 \ s^{-1}$) all will contribute to the high stress level. In previous studies on SS 316L single crystals [101, 102], it is demonstrated that austenitic steels deform by twinning when the stress levels are high regardless of the way that high stress level is achieved such as by the addition of nitrogen or carbon and decrease in temperature. Recently, this idea is extended polycrystals, where high stress levels were achieved by He ion or neutron irradiation and by increasing strain level and eventually deformation twinning was observed [127-129]. They determined that the critical stress level required for the formation of twins in polycrystals is about 600 MPa without considering the texture effect. During the present ECAE extrusions of these steels, the punch loads were three times as high as compared to the punch loads observed during the extrusion of soft materials such as Ni at room temperature. Therefore it is thought that the aforementioned stress level may have easily been achieved during high temperature extrusion of the stainless steel although the contribution of the other factors such as change in friction with temperature is not quantitatively known.

The significant effect of applied stress level on the nucleation of twinning regardless of the deformation temperature can be explained by the applied stress effect on partial dislocation separation resulting in what is often referred to as the concept of effective stacking fault energy. Marcinkowski and Miller [130] and later Copley and Kear [131] showed that in low SFE materials, the applied stress changes the equilibrium separation distance of the Shockley partials. Since the partial dislocation separation and the SFE are inversely related, the applied stress creates an effective SFE. The leading and trailing partials have different Burgers vectors, and thus, they experience different resolved shear forces under the same applied stress field. This force differential leads to an increase or decrease in the distance between partials depending on the relative orientation of applied stress direction and burgers vectors of the partials [132, 133]. The effective SFE incorporating this effect is defined as [131, 134]:

$$\gamma_{eff} = \gamma_0 + \frac{m_i \left(n_j^{(2)} - n_j^{(1)} \right)}{2} \sigma_{ij} b \qquad (3)$$

where γ_0 is the initial SFE, m_i is the slip plane normal, $n^{(2)}$ and $n^{(1)}$ are the direction of Burgers vectors of the trailing and leading Shockley partials, respectively, and σ_{ij} is the applied stress. In Fig. 5.1.11, the forces acting on the leading (1) and trailing partials (2) are shown as well as the effects of the tensile stress applied along different directions on partial dislocation separation. The effect of applied stress on the effective SFE is orientation dependent according to equation (3). To demonstrate the effect, consider the applied stress direction close to the [111] orientation under tension and compression and consider the slip system for fcc materials which is <110>{111}. The material under this applied stress experiences a decrease in the effective SFE (partials are pulled apart)

under tension, whereas the effective SFE increases (partials are squeezed together) under compression. The effect is opposite for the stresses applied along the [100] direction as shown in Fig. 5.1.12.

In considering equation (3) to determine the effective SFE, temperature dependence of the intrinsic SFE (γ_0) should be taken into consideration. Latanison and Ruff [135] and Lecroisey and Pineau [136] have demonstrated that the intrinsic SFE of austenitic stainless steels increases with temperature. At high temperatures, Suzuki effect which is the segregation of the solute atoms to stacking faults, leads to an increase in partial dislocation separation and decrease in SFE [133]. When a large amount of point defects in excess of the thermal equilibrium concentration are introduced into the crystals by a severe deformation, the segregation to stacking faults is expected to be enhanced. Indeed, Fujita et al. [133] demonstrated that these two competing effects almost cancel each other at high temperatures. Therefore, it is believed that the change in the intrinsic SFE (γ_0) is not significant as compared to the effect of the second term on the right hand side of equation (3).

$\sigma_T \rightarrow$ **Stress on Trailing Partial**

$\sigma_L \rightarrow$ **Stress on Leading Partial**

$$\sigma_L = \frac{m_i n_j^{(1)}}{2} \sigma_{ij} b_1$$

$$\sigma_T = \frac{m_i n_j^{(2)}}{2} \sigma_{ij} b_2$$

$$\gamma_{eff} = \gamma_0 + \sigma_T - \sigma_L$$
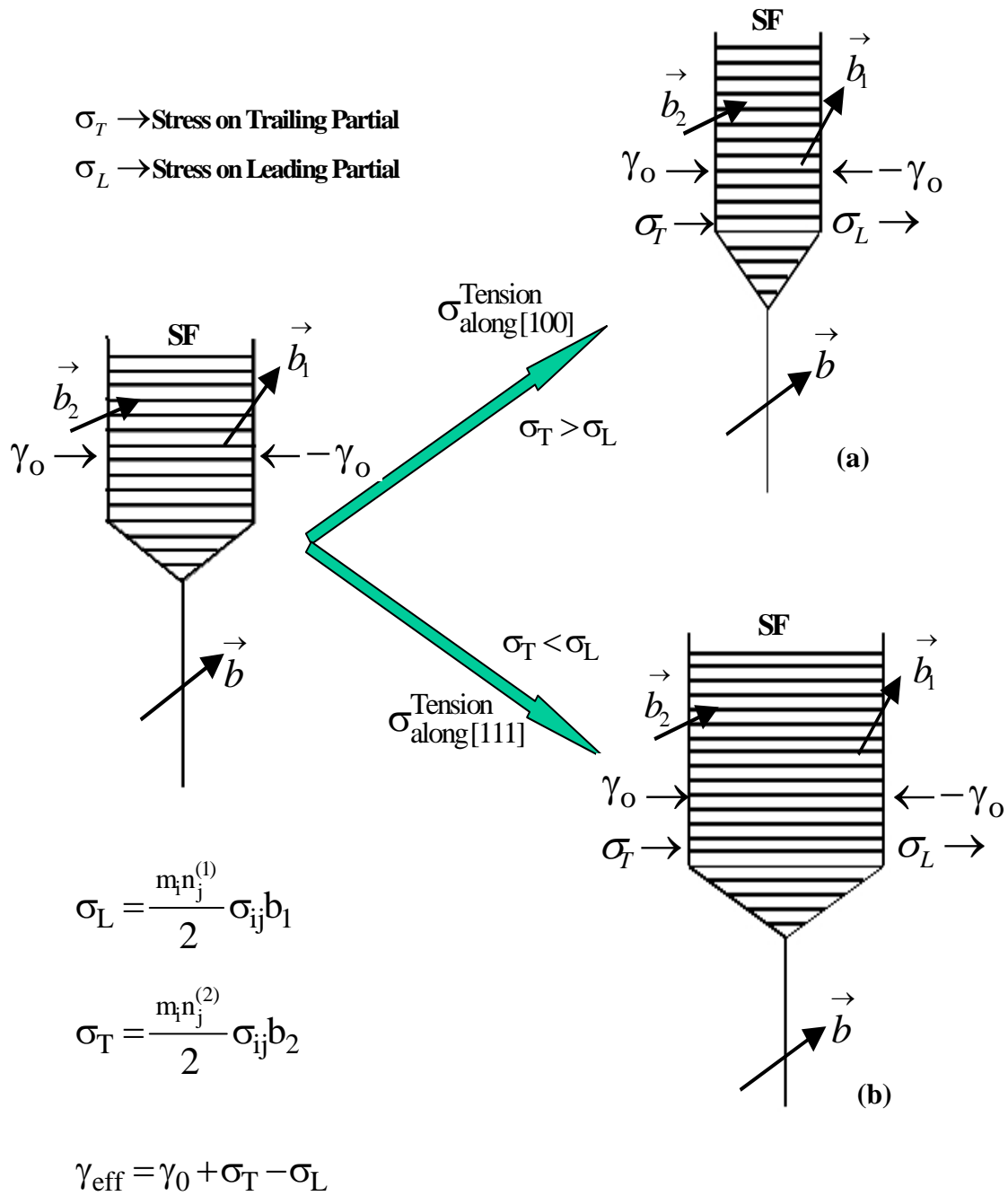
Fig. 5.1.11. Dissociation of a perfect dislocation into two shockley partials in tension with (a) loading axis along the [100] orientation and (b) loading axis along the [111] orientation.
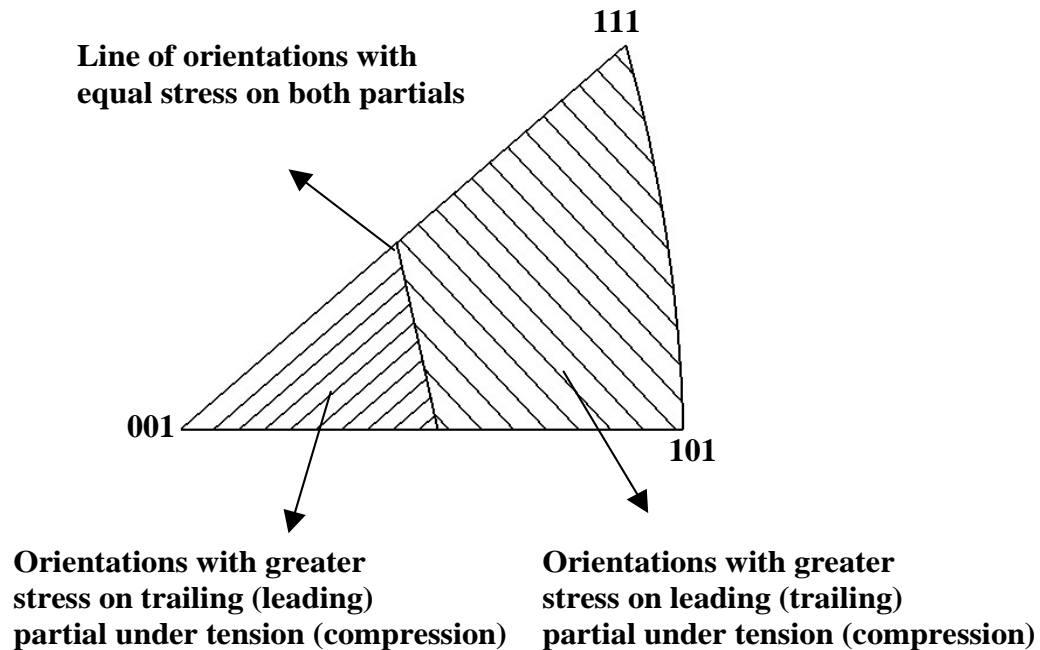
Fig. 5.1.12. The effect of applied stress on the equilibrium separation of partial dislocations. The stereographic unit triangle exhibits the applied stress effect on the separation in terms of the applied stress orientation.

Kestenbach [137] showed that the applied stress can make an average contribution of ±17% to the effective SFE in a polycrstalline 304 stainless steel under compression. It is demonstrated in single crystalline Hadfield and 316L stainless steels with nitrogen [101] that the change in the effective SFE can be as high as 50% depending on the orientation and nitrogen content at room temperature. Since the nucleation stress for twinning is directly proportional to the SFE [127], the decrease in the effective SFE leads to a decrease in twinning stress and thus, to the formation of deformation twins at early stages of deformation in single crystals [124, 138]. This is also true at high homologous temperatures in the ECAE processed polycrystals. Therefore, it is believed that the stress is more influential on deformation mechanisms of

austenitic steels than other material factors since it explains the observed deformation twinning formation.

The different microstructures developed during ECAE in different areas of the sample, i.e. the orientation dependence of twin formation, can also be attributed to the effect of applied stress on SFE. Monteiro and Kestenbach [139] studied the tensile deformation of 304 stainless steel at temperatures between 400 $^{\circ}$C and 600 $^{\circ}$C. They stated that an equiaxed cell structure is found in the [100] oriented grains whereas a banded structure consisting of aligned dislocation walls was present in the [110] oriented grains. At lower temperatures, deformation twinning was observed in the [110] and [111] orientations under tension in the stainless steel single crystals which can all be rationalized by the aforementioned theory [101, 102]. High applied stress level can sufficiently change the effective SFE such that certain grains demonstrate the microstructure of high SFE materials while others experience the microstructure of low SFE materials.

There are three main factors that contribute to the stress levels achieved during the high temperature extrusions: high strain level, relatively high strain rate, and dynamic strain aging. Puchi-Cabrera [31, 34] has studied the effect of strain level and strain rate on the high temperature deformation behavior of 316L stainless steel under compression in the dynamic strain aging regime, i.e from 300 °C to 900 °C. It was shown [31, 34-36] that at the present strain rate of 2 s^{-1} and a temperature of 700 °C, the flow stress achieved at 60% compressive strain was above 500 MPa while it was about 430 MPa at 800 °C. Considering the higher strain level achieved during ECAE and the

uniform simple shear deformation applied, it is likely to achieve Byun's [127] twinning stress level of 600 MPa. This requirement is satisfied likely satisfied for lower temperature extrusions of 450 °C and 550 °C and the two pass extrusion at 600 °C.

It is demonstrated in several studies that stainless steel exhibits dynamic strain aging in the warm working temperature regime for certain strain rates [29-37]. Two separate dynamic strain aging regimes have been reported [35]. At strain rates as slow as 0.001 s^{-1}, DSA occurs in the temperature range of 300 °C to 500 °C [33]. When the strain rate is increased two orders of magnitude, DSA is also observed at about 600 °C in addition to the temperature range of 300 °C to 500 °C [34]. The rationale for the occurrence of these two DSA regimes was attributed to three different DSA mechanisms. In the low temperature DSA regime (300 to 400 °C), it is proposed that interstitial-vacancy pair formation and diffusion of interstitials to dislocations [36] are the controlling mechanisms. Interaction of chromium with carbon atoms and formation of interstitial-substitutional pair formation leads to DSA in the intermediate temperature regime (400 to 500 °C) [35]. At higher temperatures (above 500 °C), diffusion of chromium to dislocation cores and the restriction of the dislocation motion is the most accepted mechanism [33]. Because of the relatively difficult dislocation motion due to DSA, strain hardening rate increases leading to a peak in flow stress at moderate temperatures. The temperature at which the peak stress is observed depends on the strain rate. It is reported for 304 and 316L steels [37] that the peak stress temperature is around 500 to 600 °C at low strain rates (10^{-4} s^{-1} – 10^{-3} s^{-1}). It is believed that higher strain rates increase the peak stress temperature supporting our argument on high stress levels

during the 700 °C and 800 °C extrusions. Moreover, the locking of dislocations by substitutional solutes or by the interstitial-substitutional pairs helps the nucleation of twins by providing the necessary barriers and pile up formation [123]. It has been reported [96] that DSA leads to flow instabilities and should be avoided during warm working. However, in the present investigation, flow localization was not observed during extrusions probably because of simple shear deformation applied in a very thin section of the sample during ECAE deformation.

5.2 Mechanical Behavior

Room temperature mechanical experiments were conducted on ECAE deformed samples at a strain rate of 5×10^{-4} s^{-1}. Tensile and compressive flow stresses are significantly increased as shown in Fig. 5.2.1. Increases in strain hardening coefficients with respect to as-received condition are also noticeable. For austenitic stainless steel, an ultra high strength level of about 1200 MPa is achieved. An increase in strain hardening coefficients as compared to the as-received condition is also noticeable as seen in Table 5.2.1. Toughness under tension of the sample processed at 800 °C is significantly larger than that of the as-received material while the 700 °C sample has a similar toughness as the as-received material. This may be related to two possible mechanisms, namely the broad grain size distribution due to local recovery and involvement of grain boundary moderated mechanisms in deformation [27, 123]. In samples with a broad grain size distribution, smaller grains provide the strength while larger grains lead to strain hardening and ductility, in a sense forming a composite structure. Since subgrain

boundaries possess high defect density after SPD and usually are higher angle boundaries, this leads to enhanced diffusivity. In turn, accelerated diffusion leads to easier recovery at these boundaries and it is argued that the development of grain boundary sliding which helps obtaining good ductility [27]. The strength in this second mechanism is probably connected with the difficulty of dislocation generation from non-equilibrium boundaries. However, this process also leads to the absence of strain hardening in SPD materials which is not the case in the present study where a high strain hardening is evident. Therefore, the former theory of broad grain size distribution is a more plausible explanation for the observed increase in strength without sacrificing toughness.

There is a critical microstructure and stress level that initiates brittle fracture by crack formation at the twin-twin intersections. A critical twin thickness should be maintained allowing dislocation nucleation during twin-twin penetration [140]. The low ductility of the 700 ^{o}C sample compared to other one pass extrusions can be explained with this model. The discontinuous nature of the twin band observed in Fig. 5.1.7.c may also create possible sites for crack initiation. The ductility of materials with twinning as a major mode of deformation is controlled by glide-twinning interactions. Dislocations are able to move much further than the free path in the case where the glide and twinning activities come into balance to form a steady defect structure. Otherwise if the glide dislocation density falls below a critical value with a high twin density, brittle fracture may occur [126].
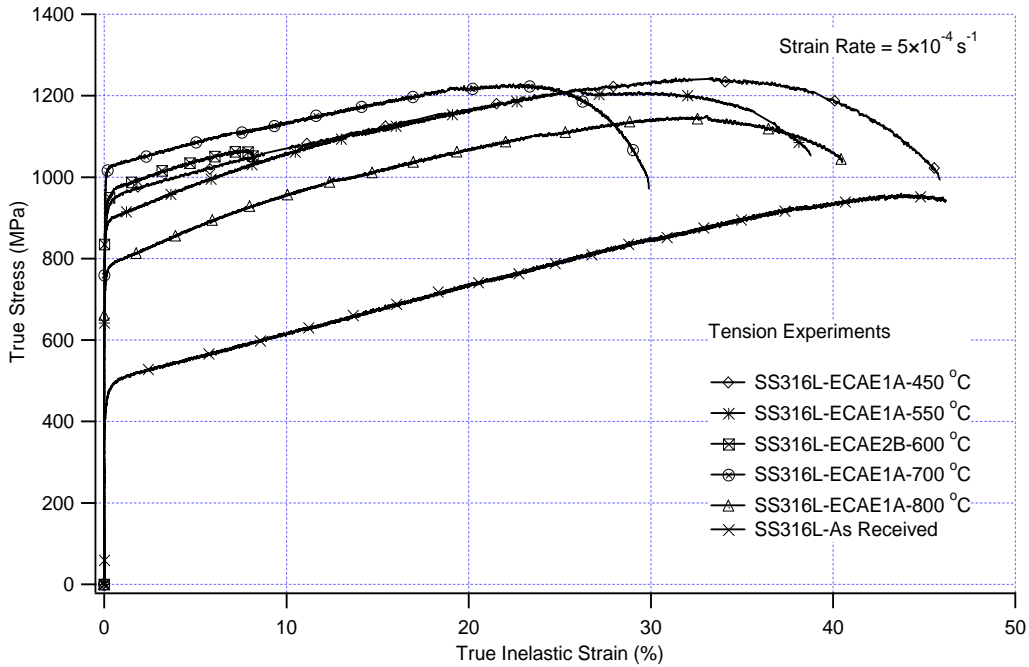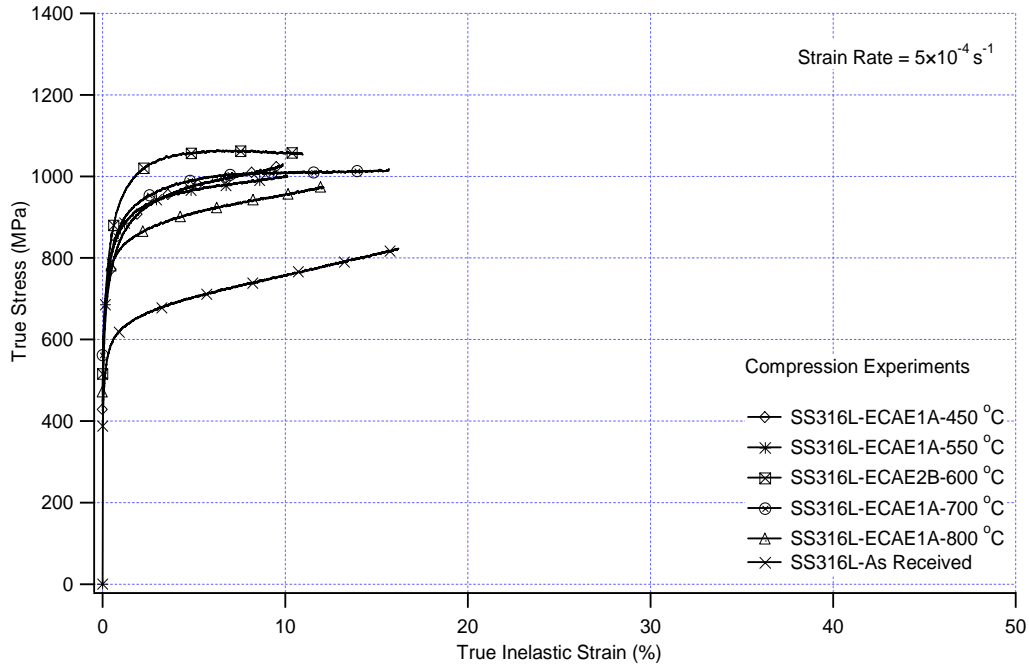
Fig. 5.2.1. (a) Tensile, (b) Compressive true stress – true inelastic strain response of as-received and ECAE processed AISI 316L samples at 5×10^{-4} s^{-1}.

Table 5.2.1

Summary of the results of the mechanical experiments conducted on AISI 316L at room temperature. σ_y: yield stress; ε_f: tensile fracture strain; $d\sigma/d\varepsilon$: strain hardening coefficient; UTS: ultimate tensile strength.

Processing Conditions	Tension $\dot{\varepsilon} = 5\times10^{-4}$				Compression $\dot{\varepsilon} = 5\times10^{-4}$	
	σ_y, MPa	UTS, MPa	ε_f, %	$d\sigma/d\varepsilon$, MPa	σ_y, MPa	$d\sigma/d\varepsilon$, MPa
450°C, ECAE 1A	920	1245	45.8	1280	680	1810
550°C, ECAE 1A	890	1215	38.8	1795	715	1180
600°C, ECAE 2B	940	1070	8.2	1450	735	1155
700°C, ECAE 1A	1020	1230	29.9	1265	730	1215
800°C, ECAE 1A	770	1150	40.5	2045	710	1855
As Received	460	960	46.2	1010	540	1465

The considerable difference in the tensile strengths of the samples processed at 700 ^{o}C and below compared with 800 ^{o}C is noticeable. This is attributed to the recovery mechanism that takes place during the higher temperature extrusion. The relatively low twin density in the 800 °C sample, and thus, a relatively low density of obstacles for slip, may be another reason for this behavior. The highest strain hardening of the 800 ^{o}C sample is attributed to the deformation of recrystallized grains supporting the occurrence of more recovery during the 800 °C extrusion than that of the rest.

Also the significant tension – compression asymmetry in the 600 °C and 700 °C extrusion samples attract attention. There can be two possible reasons for this asymmetry: texture and directional internal stress. In high strength, low SFE materials, deformation mechanisms (slip vs. twinning) are orientation dependent because of obvious Schmid's law consideration and also because of the aforementioned effect of applied stress on SFE. As mentioned earlier, twinning dislocation motion is directional as opposed to slip dislocations. Therefore, twinning systems activated under tension can not be activated under compression and the Schmid's factor for twinning in a single crystal is different under tension and compression loadings. Moreover, the applied stress direction and orientation of crystals are important in increasing or decreasing the twinning stress. In the [111] orientation under tensile loading, the Schmid factor for twinning (0.31) is higher than the Schmid factor for slip (0.27) and the tensile loading decreases the effective SFE (leading to a reduction in twinning stress. However, under compressive loading the Schmid factor for twinning is lower (0.16) and the compressive loading increases the effective SFE making twinning nucleation more difficult.

Therefore, twinning occurs more easily under tensile loading than under compressive loading in the [111] orientation, and tensile flow stresses are lower than compressive flow stresses which have been experimentally demonstrated in austenitic steel single crystals [101, 124]. The situation is opposite in the [001] orientation, i.e., twinning easily occurs under compressive loading as compared to tensile loading. Therefore, if we assume that texture would be the only reason for the observed tension - compression asymmetry, one would expect a strong [001] texture developed in the 600 °C and 700 °C samples since the tensile flow stress is higher than the compression flow stress. However, texture measurements indicated that the initial texture had strong <110> and <144> components along the extrusion direction. The high temperature extrusions did not change the texture components significantly, but led to weakening of the texture as shown in Fig. 5.2.2 with inverse pole figures along the loading axes. From these texture components, an opposite tension – compression asymmetry would have been expected (Fig. 5.1.11) meaning higher compressive stresses than tensile stresses. Indeed, the as-received material followed this expectation as the compressive yield strength is slightly higher than the tensile yield strength. Therefore, texture may not be the reason for the higher tensile flow stress observed in the 600 °C and 700 °C ECAE processed samples. Presence of oriented internal stress may be the source of this discrepancy and needs further investigation.
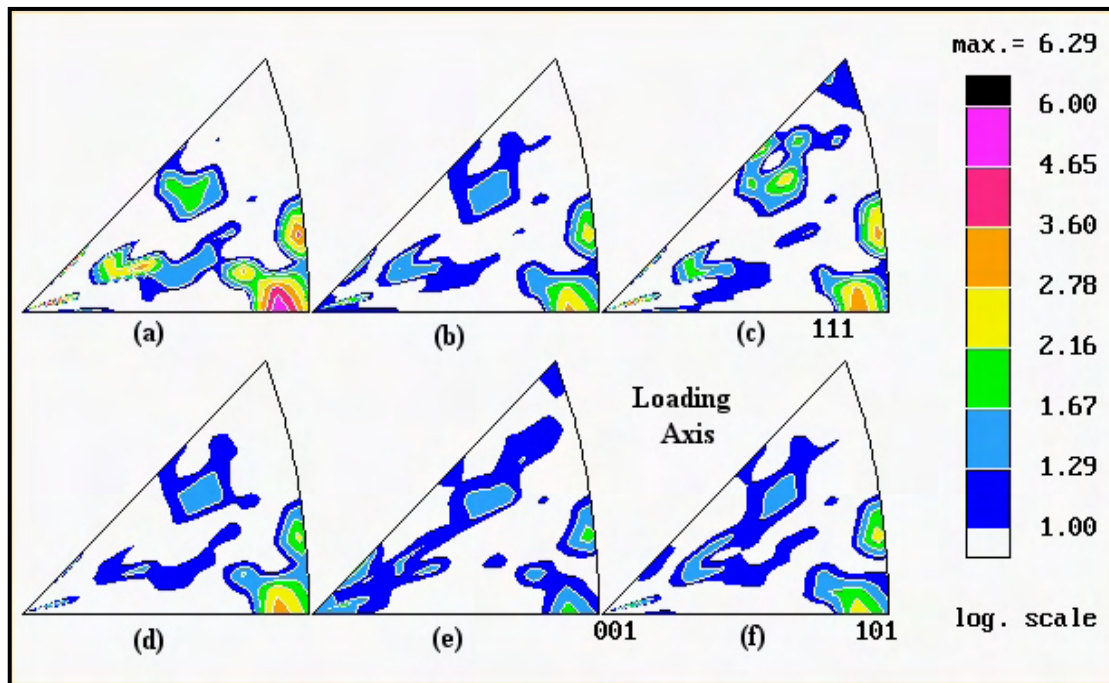
Fig. 5.2.2. Inverse pole figures of the (a) as-received material and the ECAE processed (b) 450 °C, one pass (c) 550 °C, one pass, (d) 600 °C, two passes, Route B, (e) 700 °C, one pass, (f) 800 °C, one pass sample along the loading axis. This axis is parallel to the extrusion direction. Texture components get weaker upon extrusion.

To investigate whether directional internal stress exists and to test whether it can explain the tension – compression asymmetry, a sample processed at 700 $^{\circ}$C was annealed at 500 $^{\circ}$C for one hour. This temperature was determined based on the hardness values of the samples annealed at different temperatures for one hour as will be explained later. Above 500 °C, the hardness starts to drop. The annealed sample has higher compressive flow stress than the as-extruded 700 $^{\circ}$C sample as shown in Fig. 5.2.3. The new flow stress level achieved after annealing is similar to the tensile flow stress demonstrating the effect of directional internal stresses on the asymmetry in flow stresses. Clearly, the directional (compressive) internal stress works in favor of applied

stress in compression and opposes the stress in tension. Moreover, there is a significant increase in compressive strain hardening coefficient after annealing which becomes similar to the compressive strain hardening coefficients of the as-received and the 800 °C samples demonstrating the relief of the internal stresses. Therefore, it is concluded that the main reason for the observed tension – compression asymmetry is the existence of compressive internal stress in the 700 °C extruded sample.

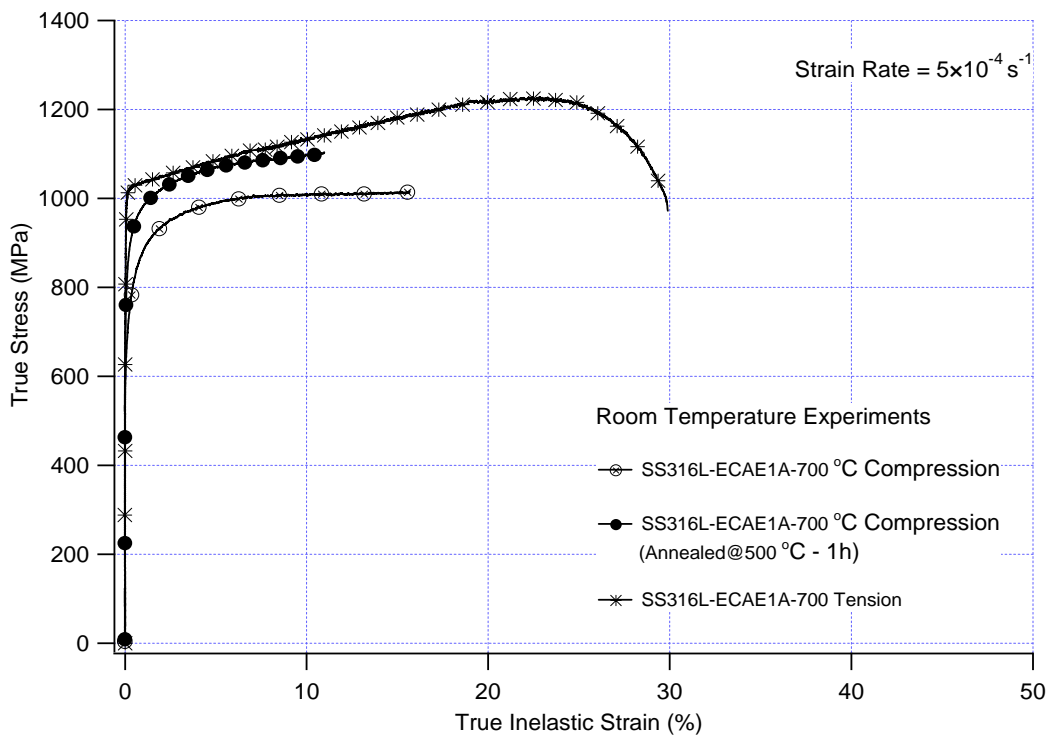**Fig. 5.2.3.** Comparison of the true stress – true inelastic strain responses of the 700 °C compression, 700 °C annealed one hour at 500 °C and 700 °C tension samples.

In conclusion, the high stress levels achieved at room temperature after extrusions can be attributed to the additional dislocation barriers provided by twin boundaries. They decrease the mean free path of the dislocations and provide

strengthening similar to grain boundaries, however to a lesser extent as they are penetrable [124]. Moreover, as opposed to the inverse dependence of the flow stress on the square root of the grain size, it inversely depends on the twin thickness. Therefore, the combined effect of the decrease in grain size and the additional strengthening due to thin twins and their boundaries result in high strength levels achieved in 316L stainless steel. The one pass 450 °C extruded sample demonstrates the most promising results in terms improved mechanical strength with near as-received material ductility. This is due to the relative absence of dynamic recovery mechanisms in this sample. Moreover, it is suggested that further extrusion passes at this temperature will evolve the unstable low angle grain boundaries to stable high angle grain boundaries and provide higher yield strengths.

Additionally, hardness tests were conducted to report any change in hardness values after ECAE processing. Each sample was tested at the three planes of deformation, namely F, L and T. Results are demonstrated in Figs. 5.2.4 and 5.2.5. It is seen that hardness values increase after severe deformation. However, no significant difference is observed between the processed samples. 600 °C sample has slightly higher hardness possibly due to the second pass. Hardness measurements conducted at different annealing temperatures were also utilized to determine the recrystallization temperature. The recrystallization of a material is characterized by softening due to the decrease of the dislocation density and the nucleation of new grains.

A drop of hardness occurs when a specimen is annealed at the recrystallization temperature. The annealing temperature of the 700 °C sample that will lead to the

relaxation of internal stresses was determined by examining Fig. 5.2.5.c. Annealing at 500 °C was chosen to remove the compressive internal stresses without significant softening.
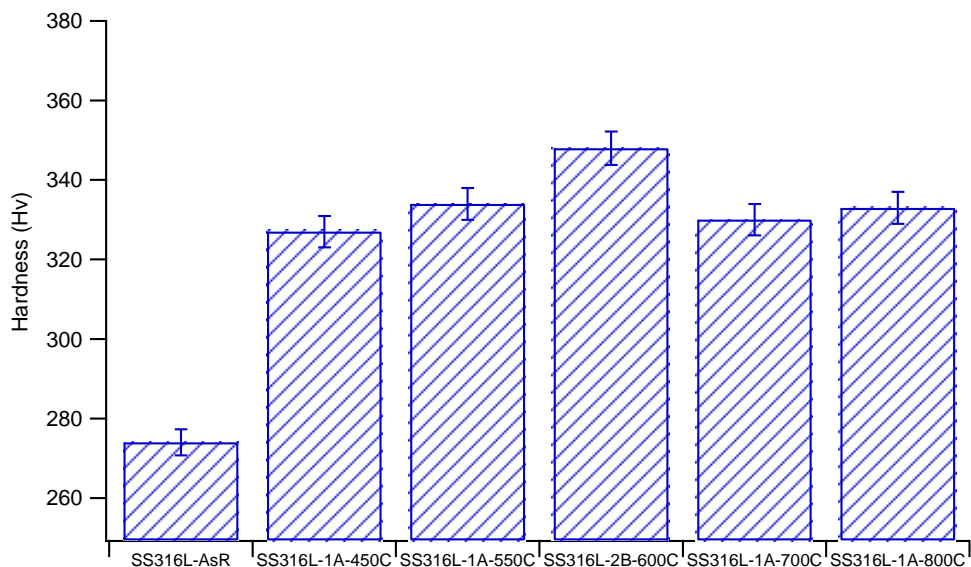
(a)
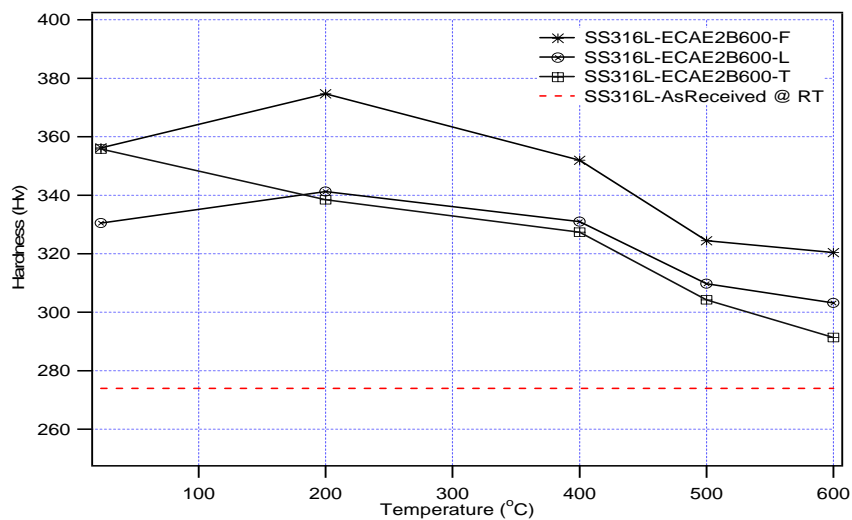
(b)

Fig. 5.2.4. (a) Average hardness measurements on as-received and ECAE processed samples, (b) Hardness measurements on different planes of the 600°C, two passes, Route 2B.
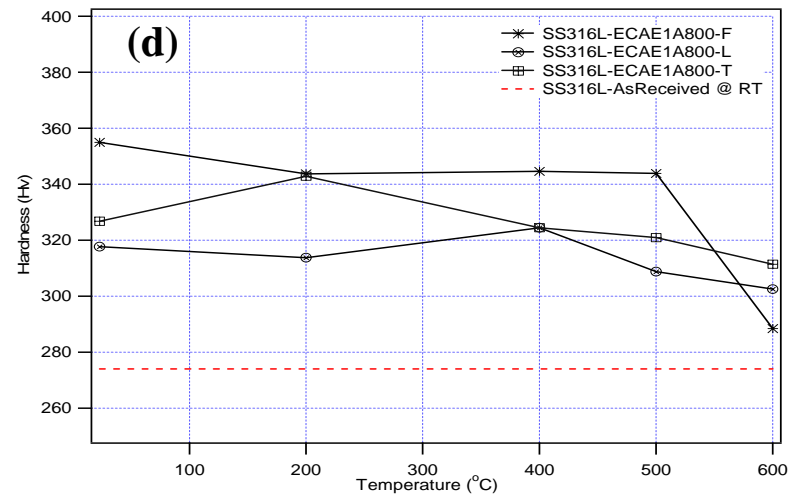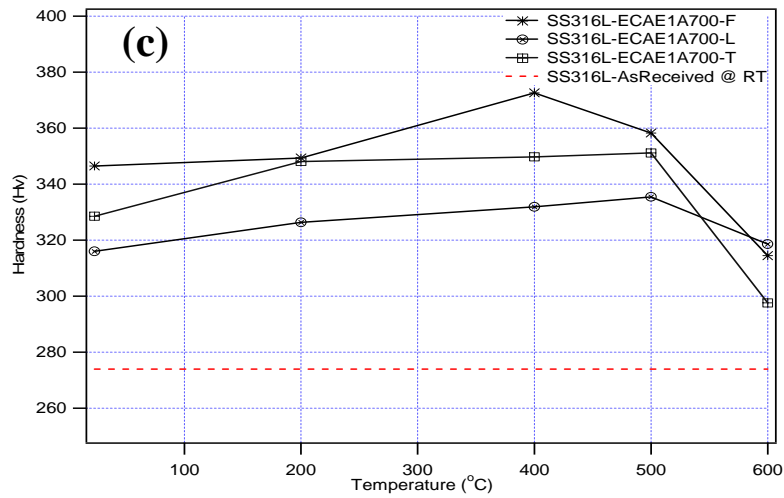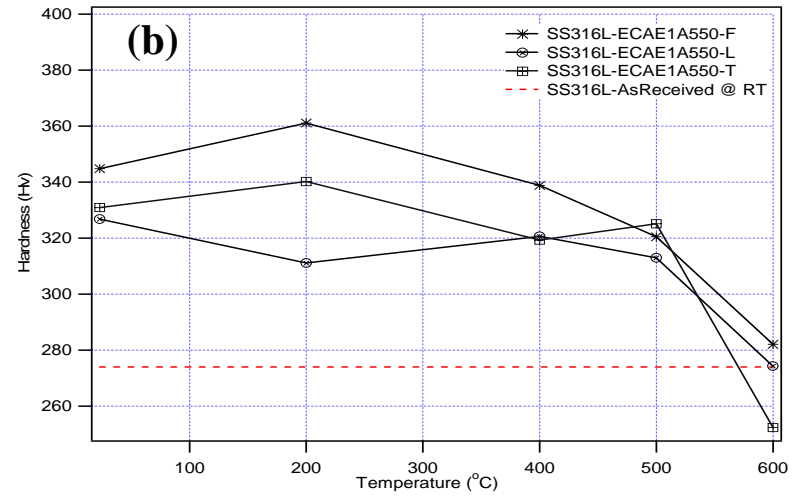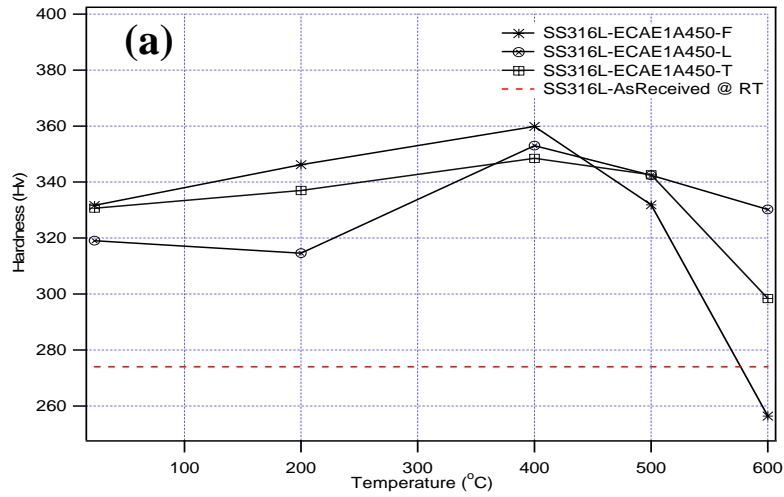
Fig. 5.2.5. Hardness measurements on different planes of the (a) 450°C, one pass, (b) 550°C, one pass, (c) 700°C, one pass, and (d) 800°C, one pass.

CHAPTER VI

CONCLUSIONS

Equal Channel Angular Extrusion (ECAE) has been shown to be a viable method for processing of difficult-to-work alloys. As a general trend of improved mechanical strengths with slight losses in ductility are recorded. In spite of the worn out conditions of the current ECAE die, we have managed to extrude samples at temperatures as low as 450 C for one pass and 600 C for two passes. The results are presented below.

Ti-6Al-4V and Ti-6Al-4V+10%TiC

ECAE processing of Ti-6Al-4V with a lamellae colony α structure was successfully performed under non-isothermal condition using stainless steel cans at temperatures above 550°C. The effects of extrusion temperature and number of passes on microstructure and room temperature monotonic stress-strain response revealed that:

1. ECAE shear deformation leads to refinement in α plates and elimination of prior β boundaries. Decreasing extrusion temperature and increasing number of passes decreases α plate size and grain size. Refined α grain size leads to a significant increase in tensile and compressive flow stresses at room temperature.

2. The second extrusion pass at 800°C increased both the yield strength and ductility. This was attributed to the observed α plate refinement.

3. Cavitation at the interface between β strips and α plates at 550°C was thought to be the reason for low ductility and relatively low strain hardening at room temperature.

4. Texture has a pronounced effect on mechanical properties. Tension/compression asymmetry in flow strengths and strain hardening coefficients may be described by the activation of differing slip systems under tension and compression loading because of texture.

5. Ti-6Al-4V+10%TiC samples also exhibited improved mechanical properties after ECAE deformation. However further extrusion passes should be carried out for enhanced particle distribution.

<u>AISI 316L</u>

Non-isothermal ECAE processing of AISI 316L stainless steel was successfully carried out between 450 $^{\circ}$C and 800 $^{\circ}$C. The effects of extrusion temperature on microstructure and room temperature monotonic stress-strain response were investigated. The results support the following conclusions:

1. ECAE deformation at high homologous temperatures (0.55 to 0.60 T_m) resulted in deformation twinning as an effective deformation mechanism. This first time observation is attributed to the effect of the high stress levels on the partial dislocation separation, i.e. effective stacking fault energy. The high stress levels were achieved by dynamic strain aging, the high strain level, and the relatively high strain rate used during ECAE. The mechanical behavior of low SFE, high strength austenitic steels and the underlying mechanisms responsible for their behavior

(competing deformation twinning and slip) are universal in a wide range of temperatures, irrespective of the way in which the high strength levels are achieved.

2. Deformation twinning led to high stress levels during post-processing room temperature monotonic experiments by providing additional barriers to dislocation motion and decreasing the mean free path of dislocations. The highest tensile flow stress observed in the sample processed 700 ^{o}C was on the order of 1200 MPa which is very high for 316L stainless steel.

3. Substantially different microstructural features were observed in different areas of the samples. This can be explained by the orientation dependence of the deformation mechanisms (slip vs. twinning).

4. The sample processed at 700 °C displayed tension-compression asymmetry in yield strength and strain hardening coefficient. Texture, orientation dependence of the deformation mechanisms and directional internal stresses are all potential causes of this behavior. From the data obtained, however, it is concluded that compressive internal stress is the main reason for the observed tension-compression asymmetry.

5. In the sample processed at 800 ^{o}C, dynamically recrystallized, nanometer size grains were formed and dynamic recovery occurred, leading to high strain hardening and lower flow stresses observed in this sample both in tension and compression tests as compared to the 700 °C sample. The lower twin volume fraction is another reason for the lower flow stress in the 800 °C sample.

6. The one pass 450 °C extruded sample demonstrates the most promising results in terms improved mechanical strength with near as-received material ductility.

REFERENCES

[1] T.C. Lowe, R.Z. Valiev, Investigations and Applications of Severe Plastic Deformation, Kluwer Academic Publishers, NY, 2000, p. 25.

[2] R.Z. Valiev, R.K. Islamgaliev, I.V. Alexandrov, Progr. Mater. Sci. 45 (2000) 103.

[3] H. Gleiter, Progr. Mater. Sci. 33 (1989) 223.

[4] C.C. Koch, Y.S. Cho, Nanostructured Mater. 1 (1992) 207.

[5] V.M. Segal, Mater. Sci. Eng. A. 197 (1995) 157.

[6] V.M. Segal, V.I. Reznikov, A.E. Drobyshevkiy, V.I. Kopylov, Russian Metall. 1 (1981) 99.

[7] M. Furukawa, Y. Iwahashi, Z. Horita, M. Nemoto, T.G. Langdon. Mater. Sci. Eng. A 257 (1998) 328.

[8] S. Ferrasse, V.M. Segal, K.T. Hartwig, R.E. Goforth, Metall. Mater. Trans. A, 28 (1997) 1047.

[9] O.V. Mishin, D.J. Jensen, N. Hansen, Mater. Sci. Eng. A. 342 (2003) 320.

[10] S.R. Agnew, J.R. Weertman, Mater. Sci. Eng. A. 244 (1998) 145.

[11] L.W. Meyer, Proc. 5th Int. Conf. on Titanium, Munich, 1984, p. 1851.

[12] C.J. Maiden, S.J. Green, J. Appl. Mech. 33 (1996) 496.

[13] A.J. Johnson, C.W. Bull, K.S. Kumar, C.L. Briant, Metall. Mater. Trans A. 34 (2003) 295.

[14] W.S. Lee, M.T. Lin, J. Mater. Proc. Tech. 71 (1997) 235.

[15] S.L. Semiatin, D.P. DeLo, Materials and Design. 21 (2000) 21 311.

[16] Y.G. Ko, W.S. Jung, D.H. Shin, C.S. Lee. Scripta Mater. 48 (2003) 197.

[17]   D.P. DeLo, S.L. Semiatin, in in: Y.T. Zhu, T.G. Langdon, R.S. Mishra, S.L. Semiatin, M.J. Saran and T.C. Lowe (Eds.), Ultrafine Grained Materials II, Proceedings of 2002 TMS Annual Meeting, Warrendale, PA, TMS, 2002, p.539.

[18]   S.L. Semiatin, D.P. DeLo, E.B. Shell, Acta Mater. 48 (2000) 1841.

[19]   Donachie MJ. Titanium:A Technical Guide, Materials Park, OH : ASM International, 2000, p. 22.

[20]   G. Lutjering, J. Albrecht, O.M. Ivasishin, Microstructure/ Property Relationships of Titanium Alloys, TMS, Warrendale, PA, 1994, p. 65.

[21]   R.I. Jaffee, H.M. Burte, Titanium Science and Technology, Vol 3, Plenum Press, NY, 1973, p. 98.

[22]   G. Lutjering, Mater. Sci. Eng. A. 243 (1998) 32.

[23]   D. Ma, J. Wang, K. Xu, Mater. Letters 56 (2002) 999.

[24]   V.M. Segal, K.T. Hartwig, R.E. Goforth, Mater. Sci. Eng. A. 224 (1997) 107.

[25]   M.E. Wahabi, J.M. Cabrera, J.M. Prado. Mater. Sci. Eng. A. 343 (2003) 116.

[26]   J.W. Simmons, Mater. Sci. Eng. A. 207 (1996) 159.

[27]   V. Tsakiris, D.V. Edmonds. Mater. Sci. Eng. A. 273 (1999) 430.

[28]   N. Hashimoto, S.J. Zinkle, A.F. Rowcliffe, J.P. Robertson, S. Jitsukawa, J Nucl. Mater. 283-287 (2000) 528.

[29]   R.L. Peng, M. Oden, Y.D. Wang, and S. Johansson, Mater. Sci. Eng. A 334 (2002) 215.

[30]   L.H. Almeida, I.L. May, and P.R. Emygdio, Mater. Charac. 41 (1998) 137.

[31]   E.S. Puchi-Cabrera, Mater. Sci. Tech. 17 (2001) 155.

[32]   S.H. Cho, Y.C. Yoo, and J.J. Jonas, J. Mater. Sci. Lett. 19 (2000) 2019.

[33]   K.G. Samuel, S.L. Mannan, and P. Rodriguez, Acta Metall. 36 (1988) 2323.

[34]   E.S. Puchi-Cabrera, Mater. Sci. Tech. 19 (2003) 189.

[35]   S. Venugopal, S.N. Mannan, and Y.V.R.K. Prasad, J. Nucl. Mater. 227 (1995) 1.

[36]   S. Venugopal, S.N. Mannan, and Y.V.R.K. Prasad, Mater. Sci. Tech. 9 (1993)
        899.

[37]   K. Tsuzaki, T. Hori, T. Maki, and I. Tamura, Mater. Sci. Eng. 61 (1983) 247.

[38]   V.M Segal , Mater. Sci. Eng. A. 271 (1999) 322.

[39]   L.R. Cornwell, K.T. Hartwig , R. E. Goforth , S.L. Semiatin, Matls. Charac. 37
        (1996) 295.

[40]   R.Z. Valiev, A.V. Korznikov, R.R. Mulyukov, Mater. Sci. Eng. A. 168 (1993)
        141.

[41]   Y. Iwahashi, M. Furukawa, Z. Horita, T.G. Langdon T.G., Acta Mater. 45
        (1997) 4733.

[42]   Y. Iwahashi, J. Wang, Z. Horita, M. Nemoto, T.G. Langdon, Scripta Mater. 35
        (1996) 143.

[43]   Horita Z., D.J. Smith, Nemoto M., R.Z. Valiev, T.G. Langdon. J. Mater. Res. 13
        (1998) 448.

[44]   K.S. Havner, Finite Plastic Deformation of Crystalline Solids, Cambridge
        University Press, Cambridge, 1992, p. 67-84.

[45]   W.F. Hosford, The Mechanics of Crystals and Textured Polycrystals, Oxford
        University Press, Oxford, 1993, p. 29-50.

[46]   C.N. Reid, Deformation Geometry for Materials Scientists, Pergamon Press, Hungary, 1973, p. 103-126.

[47]   T. H. Courtney, Mechanical Behavior of Materials, McGraw-Hill, Boston, 2000, p. 141-159.

[48]   R.E. Reed-Hill, R. Abbaschian, Physical Metallurgy Principles, PWS Publishing Company, Boston, 1991, p. 541-546.

[49]   J.W. Christian, S. Mahajan, Prog. Mater. Sci. 39 (1995) 1.

[50]   R.W. Cahn, Acta Met. 1 (1953) 49.

[51]   J.W. Christian, Metal Trans. A. 13 (1982) 509.

[52]   G.T. Gray III, Acta Met. 36 (1988) 1745.

[53]   M.J. Marcinkowski, H.A. Lipsitt, Acta Met. 10 (1962) 95.

[54]   W. Gambin, Plasticity and Textures, Kluwer Academic Publishers, NY, 2001, p. 194.

[55]   U.F. Kocks, C.N. Tome, H.R. Wenk, Texture and Anisotropy, Cambridge University Press, Cambridge, 1998, p.182.

[56]   A.W. Stephens, Ph.D. Dissertation, University of Arizona, 1969.

[57]   H. Hu, S.R. Goodman, Trans. Metall. Soc. AIME 227 (1963) 627.

[58]   M.J. Philippe, in: H.J. Bunge (Ed.), Textures of Materials ICOTOM-10, Trans. Tech. Pubs., Switzerland, 1994, p.1337.

[59]   G.R. Canova, U.F. Kocks, Acta Metall. 32 (1984) 211.

[60]   F. Montheillet, M. Cohen, J.J. Jonas, Acta Metall. 32 (1984) 2077.

[61]   W.H. Huang, L. Chang, P.W. Kao, C.P. Chang, Mater. Sci. Eng. A 307 (2001) 113.

[62]   C.S. Barrett, T.B. Massalski, Structure of Metals. Pergamon Press, Oxford, 1980.

[63]   W.Q. Cao, A. Godfrey, Q. Liu, Mater. Sci. Eng. A 361 (2003) 9-14.

[64]   M. A. Gibbs, K. T. Hartwig, L. R. Cornwell, R. E. Goforth, and E. A. Payzant, Scripta Mater. 39 (1998) 1699.

[65]   O.V. Mishin, V.Y. Gertsman, R.Z. Valiev, G. Gottstein, Scripta Mater. 35 (1996) 873.

[66]   G. Wang, S.D. Wu, L. Zuo, C. Esling, Z.G. Wang, G.Y. Li, Mater. Sci. Eng. A 346 (2003) 83.

[67]   S.R. Agnew, J.R. Weertman, Mater. Sci. Eng. A 242 (1998) 174.

[68]   A. Gholinia, P. Bate, P.B. Pragnell, Acta Mater. 50 (2002) 2121.

[69]   C. Pithan, T. Hashimato, M. Kawazoe, J. Nagahora, K. Higashi, Mater. Sci. Eng. A 307 (2001) 113.

[70]   S. Suwas, L.S. Toth, J.J. Fundenberger, A. Eberhardt, W. Skrotzki, Scripta Mater. 49 (2003) 1203.

[71]   S.R. Agnew, J.A. Horton, T.M. Lillo, D.W. Brown, Scripta Mater. 50 (2004) 377.

[72]   G. Lutjering, J.C. Williams, Titanium, Springer Publishing, Berlin, 2003, p. 177.

[73]   T. Seshacharyulu, S.C. Medeiros, W.G. Frazier, Y.V.R.K. Prasad, Mater. Sci. Eng. A. 325 (2002) 112.

[74]   S.M. Kim, J. Kim, D.H Shin, Y.G. Ko, C.S. Lee, S.L. Semiatin, Scripta Mater. 50 (2004) 927.

[75]   R.S. Mishra RS, V.V Stolyarov, C. Echer, R.Z. Valiev, A.K. Mukherjee, Mat. Sci. Eng. A. 298 (2001) 44.

[76]   A. V. Sergueeva, V.V. Stolyarov, R.Z. Valiev. A.K. Mukherjee, Mater. Sci. Eng. A. 323 (2002) 318.

[77]   T. Hebesberger, R. Pippan, H.P. Stuwe, in: Y.T. Zhu, T.G. Langdon, R.S. Mishra, S.L. Semiatin, M.J. Saran and T.C. Lowe (Eds.), Ultrafine Grained Materials II, Proceedings of 2002 TMS Annual Meeting, Warrendale, PA, TMS, 2002, p.133.

[78]   M. Frary, S. Abkowitz, S.M. Abkowitz, D.C. Dunand, Mater. Sci. Eng. A 344 (2003) 103.

[79]   C. Leyens, M. Peters, Titanium and Titanium Alloys, Wiley-VCH Publishing, Weinheim, Germany, 2003, p. 305.

[80]   T.M. Godfrey, A. Wisbey, A. Brown, R. Brydson, C. Hammond, in: M. Winstone (Ed.), Titanium Alloys at Elevated Temperature, Cambridge University Press, Cambridge, 2001, p. 165.

[81]   S. Mall, T. Nicholas, Titanium Matrix Composites: Mechanical Behavior, Technomic Pub., Lancaster, PA, 1998, p. 47.

[82]   Y.J. Kim, H. Chung, S.L. Kang, Mater. Sci. Eng. A 333 (2002) 343.

[83]   S. Gorsse, D.B. Miracle, Acta Mater., 51, (2003), 2427.

[84]   W.O. Soboyejo, R.J. Lederich, S.M.L. Sastry, Acta Metall, Mater. 42 (1994) 2579.

[85]   T.S. Srivatsan, W.O. Soboyejo, R.J. Lederich, Composites Part A. 28 (1997) 365.

[86]   F. Galvez, C. Gonzalez, P. Poza, J. Llorca, Sripta Mater. 44 (2001) 2667.

[87]   Z.Y. Ma, R.S. Mishra, S.C. Tong, Acta Mater. 50 (2002) 4293.

[88]   S.J. Zhu, D. Mukherji, W. Chen, Y.X. Lu, Z.G. Wang, R.P. Wahi, Mater. Sci. Eng. A 256 (1998) 301.

[89]   H.S. Kahatak, B. Raj, Corrosion of Austenitic Stainless Steels, Narosa Publishing House, Delhi, India, 2002, p. 2.

[90]   J. Beddoes, J.G. Parr, Introduction to Stainless Steels, ASM International, Materials Park, Ohio, 1999, p. 122.

[91]   P. Marshall, Austenitic Stainless Steels: Microstructure and Mechanical Properties, Elsevier Applied Science, London, England, 1984, p. 19.

[92]   A.J. Sedriks, Corrosion of Stainless Steels, John Wiley & Sons, NY, 1996, p. 16.

[93]   Y. Saito, H. Utsunomiya, N. Tsuji, T. Sakai, Acta Mater. 47 (1999) 579.

[94]   D.H. Shin, W.-J. Kim, W.Y. Choo, Scrip. Mater. 41 (1999) 259.

[95]   N. Tsuji, Y. Saito, H. Utsunomiya, S. Tanigawa, Scrip. Mater. 40 (1999) 795.

[96]   A. Belyakov, T. Sakai, H. Miura. Mater. Sci. Eng. A. 319-321 (2001) 867.

[97]   S.V. Dobatkin, in: Y.T. Zhu, T.G. Langdon, R.S. Mishra, S.L. Semiatin, M.J. Saran and T.C. Lowe (Eds.), Ultrafine Grained Materials II, Proceedings of 2002 TMS Annual Meeting, Warrendale, PA, TMS, 2002, p.183.

[98]   A. Belyakov, T. Sakai, H. Miura, R. Kaibyshev, Scrip. Mater. 42 (2000) 319.

[99]   A. Belyakov, H. Miura, T. Sakai, Scrip. Mater. 43 (2000) 21.

[100]   R. Priestner, A.K. Ibraheem, Mater. Sci. Technol. 16 (2000) 1267.

[101]   I. Karaman, H. Sehitoglu, H.J. Maier, and Y.I. Chumlyakov, Acta Mater. 49 (2001) 3919.

[102]   Y.I. Chumlyakov, I.V. Kireeva, and O.V. Ivanova, Phy. Met. Metall.78 (1994) 350.

[103]   X. Feaugas, Acta Mater. 47 (1999) 3617.

[104]   A. Belyakov, T. Sakai, and H. Miura, R. Kaibyshev, K. Tsuzaki, Acta Mater. 50 (2002) 1547.

[105]   A. Belyakov, R. Kaibyshev, Nanostructured Mater. 6 (1995) 893.

[106]   H.K. Kim, M. Choi, C.S. Chung, D.H. Shin, Mater. Sci. Eng. A 340 (2003) 243.

[107]   D.H. Shin, B.C. Kim, Y.S Kim, K.T. Park, Acta Mater. 48 (2000) 2247.

[108]   K.T. Park, Y.S. Kim, J.G. Lee, D.H Shin, Mater. Sci. Eng. A 293 (2000) 165.

[109]   N. Tsuji, R. Ueji, Y. Minamino, Y. Saito, Scrip. Mater. 46 (2002) 305.

[110]   H. Chandler, Hardness Testing, ASM International, Materials Park, Ohio, 1999, p. 66.

[111]   J.S. Kallend, U.F. Kocks, A.D. Rollett, and R.H. Wenk, Mater. Sci. Eng. A 132 (1991) 1.

[112]   S.L. Semiatin, V. Seetharaman, A.K. Ghosh, E.B. Shell, M.P. Simon, P.N. Fagin, Mater. Sci. Eng. A. 256 (1998) 92.

[113]   N.E. Paton, J.C. Williams, G.P. Rauscher, Titanium Science and Technology, Plenum Press, New York, 1973, p.1049.

[114]   D.P. DeLo, T.R. Bieler, S.L. Semiatin. in: R.S. Mishra, S.L. Semiatin, C. Suryanarayana, N.N. Thadhani and T.C. Lowe (Eds.), Ultrafine Grained Materials, Warrendale, PA, TMS, 2000, p.257.

[115]   J.S. Lecomte, M.J. Philippe, P. Klimanek, La Revue de Metallurgie-CIT / Science et Genie des Materiaux. 2 (1999) 201.

[116]   J.J. Fundenberger, M.J. Philippe, F. Wagner, C. Eslin, Acta Mater. 45 (1997) 4041.

[117]   S. Asgari, E. El-Danaf, S. Kalidindi, R.D. Doherty. Met. Mater. Trans. A 28 (1997) 1781.

[118]   P. Mullner, C. Solenthaler, P. Uggowitzer, M.O. Speidel, Mater. Sci. Eng. A 164 (1993) 164.

[119]   E. El-Danaf, S. Kalidindi, R.D. Doherty, Met. Mater. Trans. A 30 (1999)1223.

[120]   A. Belyakov, H. Miura, T. Sakai, Mater. Sci. Eng. A 255 (1998) 139.

[121]   A. Belyakov, Y. Sakai, T. Hara, Y. Kimura, K. Tsuzaki, Scripta Mater. 45 (2001) 1213.

[122]   R.O. Kaibyshev, O.S. Sitdikov, Phys. Met. Metall.89 (2000) 384.

[123]   I. Karaman, K. Gall, H. Sehitoglu, Y. I. Chumlyakov, and H.J. Maier, Acta Mater. 48 (2000) 1345.

[124]   I. Karaman, H. Sehitoglu, A.J. Beaudoin, H.J. Maier, Y.I Chumlyakov, and C.N. Tome, Acta Mater. 48 (2000) 2031.

[125]   I. Karaman, H. Sehitoglu, Y.I. Chumlyakov, and H.J. Maier, JOM 54 (2002) 31.

[126]   P. Mullner and C. Solenthaler, Mater. Sci. Eng. A 230 (1997) 107.

[127]   T.S. Byun, Acta Mater. 51 (2003) 3063.

[128]   E.H. Lee, T.S. Byun, J.D. Hunn, M.H. Yoo, K. Farrell, and L.K. Mansur, Acta Mater. 49 (2001) 3269.

[129] E.H. Lee, M.H. Yoo, T.S. Byun, J.D. Hunn, K. Farrell, and L.K. Mansur, Acta Mater. 49 (2001) 3277.

[130] M.J. Marcinkowski and D.S. Miller, Phil. Mag. 6 (1961) 871.

[131] S.M. Copley and B. H. Kear, Acta Metall. 16 (1968) 227.

[132] D. Goodchild, W.T. Roberts, and D.V. Wilson, Acta Metall. 18 (1970) 1137.

[133] M. Fujita, Y. Kaneko, A. Nohara, H. Saka, R. Zauter and H. Mughrabi, Iron and Steel Institute of Japan Journal. 34 (1994) 697.

[134] I. Karaman, H. Sehitoglu, K. Gall, and Y. I. Chumlyakov, Scripta Mater. 38 (1998) 1009.

[135] R. M. Latanison and A. W. Ruff, Metall. Trans. 2 (1971) 505.

[136] F. Lecroisey and A. Pineau, Metall. Trans. 3 (1972) 387.

[137] H.J. Kestenbach, Phil. Mag. 36 (1977) 1509.

[138] I. Karaman, H. Sehitoglu, Y.I. Chumlyakov, H.J. Maier, and I.V. Kireeva, Metall. Mater. Trans. A 32 (2001) 695.

[139] S.N. Monteiro and H.J. Kestenbach, Metall. Trans A 6 (1975) 938.

[140] P. Mullner, Mater. Sci. Eng. A 234-236 (1997) 97.

VITA

Guney Guven Yapici was born in Adana, Turkey in 1980. He graduated form Uskudar Science High School, and started his education in Bogazici University, Istanbul. In 2001, he received a B.S. degree in mechanical engineering. After graduation, he continued his studies at Texas A&M University, in the Department of Mechanical Engineering. He has been conducting research on mechanics and materials behavior as a research assistant since then. During his studies, he authored two peer-reviewed journal articles and 2 conference publications. Mr. Yapici wishes to continue his academic life by pursuing a Ph.D. in the same field. He can be reached at his permanent address:

Akdogan Sk. Ay Apt.

40/7 Besiktas 80690

Istanbul, TURKEY.